REPORT No. 47

BOUNDARY LAYER EFFECTS ON AIRFOIL LIFT

KURT H. SCHNEIDER

September 1958

GAS TURBINE LABORATORY
MASSACHUSETTS INSTITUTE OF TECHNOLOGY
CAMBRIDGE · 39 · MASSACHUSETTS

BOUNDARY LAYER EFFECTS ON AIRFOIL LIFT

by

KURT H. SCHNEIDER

Under the sponsorship of:

Office of Naval Research Contract Number 1841 (13)

Gas Turbine Laboratory
Report Number 47

September
1958

Massachusetts Institute of Technology

ABSTRACT

A study of the discrepancy in lift between potential flow calculations and experiments was made.

In potential flow the fluid is assumed to follow the contour of the airfoil, forming a stagnation point at the geometric center of the trailing edge. In the flow of a viscous fluid around an airfoil a boundary layer forms along the surface of the airfoil changing its effective shape. The pressure at the trailing edge is approximately equal to the static pressure at upstream infinity.

Detail stagnation and static pressure and flow direction surveys were made near the trailing edge on a 50 inch chord NACA 0015 airfoil with trailing edge thickness increased to three per cent chord.

By the use of thin airfoil theory, modified to include terms of second order, good agreement with published experiments in lift and pressure distribution is obtained.

Using Teledeltos paper, an electrical analog of the flow around the NACA 0015 airfoil in the tunnel was made. A method was developed for determining velocity directly from the analog.

ACKNOWLEDGEMENTS

The work described in this report marks the final period of close association with the Gas Turbine Laboratory at the Massachusetts Institute of Technology. It is with deep regret that I step outside this group of interesting, helpful and friendly people.

My sincere gratitude goes to Professor E. S. Taylor, Director of the Gas Turbine Laboratory, whose generosity, tolerance, and everlasting good humour has won him great respect and admiration. I shall always be indebted to him for giving me the opportunity to study at the Gas Turbine Laboratory.

For the time and effort spent in the supervision of this investigation, I want to thank Professors A. H. Shapiro, A. H. Stenning, H. Ashley and Y. Senoo.

Of the many other people who assisted in the program I want to mention Messieurs P. Wassmouth, D. Baugh, the personnel in the Model and Electronic Shops of the Aero-Elastic and Structures Research Group in the Aeronautical Department, and Messieurs A. Maksymowicz, H. Lima, R. Jones, V. Pham and Mrs. S. Fahlquist who helped in the experimental investigation, data reduction and presentation of the results. Last and not least I must acknowledge the very important work of the reluctant yet helpful typist, Natalie Appleton.

TABLE OF CONTENTS

NOMENCLATURE

c = chord

c_d = drag coefficient $\left(\frac{D}{\frac{1}{2}\rho W_\infty^2 c}\right)$

c_l = lift coefficient - - - - - - - - - $\left(\frac{L}{\frac{1}{2}\rho W_\infty^2 c}\right)$

c_p = pressure coefficient $\left(\frac{p - p_r}{p_{or} - p_r}\right)$

p = local static pressure

p_o = local stagnation pressure

p_r = reference static pressure; also static pressure at upstream infinity

p_{or} = reference stagnation pressure; also stagnation pressure at upstream infinity

r = distance of probe from center of the trailing edge of the airfoil

u = induced velocity in x - direction

v = induced velocity in y - direction

w = total induced velocity

W = local velocity

x, y = rectangular coordinates

z = complex number $(x + iy)$

α = angle of attack of airfoil; angle between chord line and velocity vector at upstream infinity

β = angular position of aluminum disk with respect to tunnel centerline

Γ = circulation around the airfoil

Γ_0 = circulation around the airfoil with stagnation point at geometric center of trailing edge

SUBSCRIPTS

c = refers to the meanline

e = refers to the trailing edge

p = refers to the pressure side of the airfoil

q = refers to the source and sink distribution

s = refers to the suction side of the airfoil

t = refers to the basic thickness airfoil

δ = refers to the edge of the boundary layer or wake

γ = refers to the vortex distribution

∞ = refers to far upstream conditions

1. INTRODUCTION

Experience shows that a body in motion relative to a viscous fluid always experiences a force resisting the motion. Depending on the shape of the body there may exist an additional force, normal to the relative velocity vector at infinity.

Up to the 16th century only physical descriptions - magic forces not excluded - were presented, proving and disproving the existence of such forces.

With the development of more advanced mathematical methods and by application of Newton's laws, the flow around bodies immersed in an infinite fluid could be described mathematically.

Classic hydrodynamics was established and about the middle of the 17th century d'Alembert proposed his famous paradox, stating that no net force acts on a body moving through a fluid with constant velocity. Realizing that this is contrary to experience, d'Alembert says: "a singular paradox which I leave to geometricians to explain".

With the introduction of the concept of vortex motion by Helmholtz the basic step for solving this paradox was accomplished. Kutta and Joukowski, working independently, calculated the force acting on a body around which there existed a circulation, and applied it to the calculation of the lift on an airfoil. The airfoil shape was obtained from a circle by a simple conformal transformation which resulted in a cusped trailing edge. The amount of circulation was fixed by the requirement that the flow should leave the trailing edge smoothly.

For an airfoil of finite trailing edge angle or finite trailing edge thickness the circulation is fixed by requiring that no flow occurs around the trailing edge, i.e. the geometric center of the trailing edge is a stagnation point.

The fomulation of another basic concept in fluid mechanics, the fluid of small viscosity, made it more difficult to determine the amount of circulation. Prandtl showed that near a solid boundary a thin layer of fluid existed, in which viscous forces were of the same order of magnitude as pressure and inertia forces. In this boundary layer the velocity varies from the free stream velocity to zero at the solid boundary. At the trailing edge of the airfoil the two boundary layers from the pressure and suction side of the arifoil join to form the wake; no stagnation point is established, however, although the original suggestion, i.e. that the flow should leave the trailing edge smoothly, is still satisfied for each side of the airfoil in the unstalled region of operation.

Any theory for the calculation of the actual lift of an airfoil (as opposed to the lift calculated from the Kutta-Joukowski hypothesis of no flow around the trailing edge), therefore, has to include the effects of viscosity, in form of the boundary layer along the surface of the airfoil on one hand, and the flow condition near the trailing edge on the other hand.

2 EXPERIMENTAL INVESTIGATION

When originally considering the problem of the difference in lift as obtained from experiment and theory, based on the Kutta - Joukowski condition, it was thought that much of the difference was due to the details of flow around the trailing edge. The position of the stagnation point at the trailing edge determines the circulation in theroetical calculations, and therefore the lift. Very small changes in this position could change the lift appreciably.

To demonstrate this, calculations were made on an ellipse of unit major diameter, minor diameter of 0.173 and leading and trailing edge radii of 0.015. (The eccentricity of the ellipse was adjusted such that the radius of curvature was the same as that of the airfoil used in the experiment.) Comparing this ellipse with an airfoil and making calculations at angles of attack of 4, 8 and 12 degrees, the change in position of the rear stagnation point due to a change in lift of 5, 10, and 15 per cent was calculated (8, 13). If Γ is the variable lift, Γ_0 the lift at 4, 8, and 12 degrees, respectively, with the stagnation point at the geometric center of the trailing edge, the motion of the corresponding stagnation point along the arc away from the geometric center was calculated and is given in the table below

	Motion of stagnation point Δ s		
α T/T_o	4°	8°	12°
1.0	.0000	.0000	.0000
.95	.0012	.0026	.0040
.90	.0026	.0068	.0090
.85	.0040	.0090	.0180

For example, at an angle of attack of 4 degrees $(C_l \approx .44)$ a motion of .0026 units in the position of the stagnation point of an airfoil of elliptical cross-section would change the circulation by 10 per cent.

In the available literature there were no detail experimental data of pressure distribtuin and flow direction near the trailing edge of an airfoil.

In order to obtain this information an experimental program was initiated with the purpose of investigating in detail the flow in the immediate neighbourhood of the trailing edge of an airfoil.

2.1 Experimental set up

It was desirable to use an airfoil of large size in order to decrease probe interference effects and increase the relative accuracy of the measurements. As a closed circuit wind tunnel with a test section of 7 ft width and 5 1/2 ft height was available, the chord of the airfoil was made 50 inches long.

The airfoil decided upon was a NACA 0015 section with the trailing edge increased to a thickness of 3 per cent chord to represent more closely an actual blade. A drawing of the airfoil is shown in Fig. 10, the coordinates are given in Appendix 3.

The airfoil stood vertically in the test section and could be rotated around the center of the trailing edge for adjustment of the angle of attack. A 1/2 inch diameter shaft extended from the top trailing edge center of the airfoil upward and rotated in a 1 inch thick, 12 inch diameter aluminum disk. This disk was supported on three bearings in the top tunnel wall and rotated around the same center as the airfoil (Fig. 11). A radial slot was machined in the disk carrying the probe holder (Fig. 12). The radial distance of the measuring probe from the center of the disk (and of the trailing edge), the angular position of the disk with respect to the center line of the tunnel and the angular position of the probe with respect to the disk could be contolled and measured from the desk in front of the test section (Fig. 13). The measuring probes extended 20 inches from the top of the tunnel to the tip of the probe.

2.2 Instrumentation

Stagnation pressure and direction were measured with a three-hole cobra probe (Fig. 14). The zero position of the probe was determined before each test by placing a four foot length of a 3 inch diameter thin walled tube in the tunnel, parallel to the tunnel wall. The probe was then yawed at the exit. (A traverse at the exit showed a flat velocity profile of 1.2 inches diameter).

The static pressure was determined by means of a sphere static probe manufactured by the Flow Corporation in Arlington,Mass. This probe has a spherical tip of 1/8 inch diameter. Two prodruding rings are machined on the sphere to insure a turbulent separation. The pressure holes are located in the stem joining the sphere. If p_p is the pressure measured by this probe, the ratio $p - p_p/p_o - p$ stays essentially constant for a large variation in inflow direction. The calibration curve for one of the sphere static probes at different tunnel velocities is shown in Fig. 15.

As the stem of the probe was bent away from the center of rotation, because of aerodynamic interference, it was necessary to use two probes, one for the pressure and one for the suction side, respectively. For stagnation pressure and direction measurements through the wake, where large stagnation pressure and direction gradients existed, a third probe of essentially straight stem design was used. All probes were constructed such as to have the measuring point at the center of rotation.

The pressure signal was transmitted to Statham pressure transducers and read on galvanometers located on the control desk.

To obtaim information on the unsteadiness of the flow in the vicinity of the trailing edge hot wire measurements were made along arcs with radii $r/c = .084$, $.054$ and $.024$, measured from the center of the trailing edge. Low frequency fluctuations (up to 70 cycles per second) were recorded on a Sanborn recorder, high frequencies on a two-channel DuMont oscilloscope.

Since in the direct vicinity of the trailing edge large changes in direction were observed with the three hole probe, lamp black traces were made on aluminum plates fixed perpendicular to the span at the trailing edge. Since no change in flow pattern was noticed when going from small plates of different shapes (approximately 3 x 2 inches) to larger plates, it was decided that the interaction between the plate boundary layer and the boundary layer on the surface of the airfoil was small. The plate size finally used was 14 inches long in the direction of the chord and 7 inches wide. The lamp black was mixed with kerosine and applied on the plate with variable concentration to give clear traces in regions of low velocity.

2.3 Experimental set up.

All experiments were made at a mean tunnel velocity of 107 ft/sec.

2.3.1 Pressure distribution and direction

The distribution of static and stagnation pressures, flow direction and velocity are plotted as contour graphs in Figs. 16 - 19. These graphs were obtained by first plotting the experimental results for a constant radius against angular position of the aluminum disk (β), and then transferring the data to the contour graphs at convinient values of the variable in question. Contours drawn in dashed lines represent an estimate where no direct measurements were possible. The streamlines were drawn from isoclines constructed from the contours of constant angle.

2.3.2 Hot wire measurements.

The purpose of these measurements was mainly to obtain approximate results on the frequency and magnitude of the velocity fluctuations in the neighbourhood of the trailing edge. The measurements were made for an angle of attack of 8.2 degrees. The results obtained from the Sanborn recorder for the locations shown in Fig. 20, are presented in Fig. 21, those obtained with the oscilloscope at the same locations in Fig. 22. No periodic nature of the fluctuating frequencies within the response of the hot wire used (upper limit about 300 cycles per second) was observed.

The calibration curve for the hot wire is shown in Fig. 23. Knowing the average velocity at the points where hot wire measurements were taken, the magnitude of the fluctuations was estimated by assuming the average velocity to be the arithmetic mean of the fluctuating velocities. A graph of these results, where fluctuating velocity ΔW, devided by the upstream velocity W_∞ is plotted against angular position of the disk, β , for three radii, r/c, is presented in Fig. 24. These data are taken from the oscilloscope traces.

2.3.3 Lamp black traces.

To obtain a direct representation of the flow pattern, lamp black traces were made for the flow near the trailing edge for $\alpha = 0$, 4, 8.2, and 12 degrees. Two photographs are shown for each angle of attack. In the first, the lamp black originally covered the whole plate. In the second, only the two wings of the plate, extending upstream on each side of the airfoil were painted with lamp black.

The most interesting phenomenon was the existence of two small, counter-rotating vortices in the bubble behind the airfoil. The strength of these vortices was of the order of 1/2 per cent of the circulation around the airfoil. This estimate was based on the measured velocity at the edge of the vortex and the distance between the center and the edge of the vortex as determined from the lamp black traces. As may be seen from the photographs of the lamp black traces, reproduced in Fig. 25, the vortex on the suction side grows with angle of attack, while the pressure side vortex decreases in strength, such that at 12 degrees angle of attack (stall occurs at about 14 degrees) this vortex is hardly discernible.

2.3.4 Changes in trailing edge shape.

It seemed of interest to change the shape of the trailing edge, to investigate the effect on the flow near the trailing edge.

In the first experiment the semi-circular trailing edge was cut off such as to leave a square trailing edge. The contour plots of stagnation and static pressures, of velocity, constant flow angle and streamlines are presented in Fig. 26. The lamp black experiment (Fig. 25 e) produced the most easily recognized effect: the vortex motion near the trailing edge was much more intense. At the center of the two vortices relatively low pressures existed which caused the lamp black mixture to be sucked up from the plate to a height of about 3 inches from where it dropped back to the plate further downstream.

In the second experiment a short, cusped trailing edge shape was fixed to the airfoil. The cusp was designed such as to conform with the two streamlines which coincide with the surfaces of the airfoil in the flow with the semi-circular trailing edge. It was hoped that in this way the bubble behind the airfoil would be essentially eliminated without disturbing the rest of the flow pattern. The lamp black photograph (Fig. 25 f) shows that the vortices are nearly eliminated. Only the trace shown in Fig.25f showed a trace of a vortex on the suction side; other traces made under the same condition did not show any vortex motion.

Attempts were made to apply suction through a 1/16 inch wide slot at the trailing edge of the cusp. However, no meaningful data were obteined from this experiment.

2.3.5 Pressure distribution.

Along the surface of the airfoil 67 pressure holes were drilled in a 2 inch wide brass strip inserted in the wood of the airfoil 20 inches from the top. The pressures as read on a 30-tube manometer board, using .827 specific gravity Meriam manometer fluid, are shown in Fig. 27 for angles of attack of 0, 4, 8.2 and 12 degrees. On the same graphs are shown the pressure distributions as corrected for tunnel wall interference at corrected angles of attack (14).

2.3.6 Drag measurements.

The drag for different angles of attack and different trailing edge shapes was calculated according to Jone's formula (15):

$$c_d = 2\int_{-\delta/c}^{\delta/c} \frac{W}{W_\infty}\left(1 - \sqrt{1 + \frac{p_o - p_{or}}{p_{or} - p_r}}\right) d\left(\frac{y}{c}\right)$$

In the derivation of this formula it was assumed that no change of total pressure occurs in a stream-tube between a station close to the airfoil and far downstream. Although this assumption is not correct, experiments (15) have shown that the method gives results within 5 per cent of the correct value even when applied at distances of .02 c behind the airfoil.

The values obtained for the drag are relatively high (Fig. 28). Possible explanations for this are the thick trailing edge, the effect of the tunnel wall interference and the high free stream turbulence of the air in the tunnel.

The different trailing edge shapes were compared on the basis of equal distances from the trailing edge. The square trailing edge shows a 13 per cent higher drag coefficient than the semi-circular trailing edge, while the cusped trailing edge shows a 8 per cent lower drag coefficient. Since the pressure distribution around the airfoil did not change perceptibly for the different trailing edge shapes the differences in drag coefficient were expected to result from the pressure drag of the different trailing edges. By plotting the pressure coefficient against normal to the chord (Fig. 29) it was found that the square trailing edge gave a 15 per cent higher pressure drag than the semi-circular trailing edge, while the cusped trailing edge pressure drag was 5 per cent lower.

2.3.7 Transition measurements and boundary layer calculations.

The forward half of the airfoil was covered with a sheet of linen soaked with cobalt chloride, dissolved in water. In the turbulent boundary layer evaporation occurred at a higher rate than in the laminar boundary layer and th cobalt chloride changed from a pink to a blue colour when drying. A reproduction of the photographs, originally in colour, is shown in Fig. 30. The start of turbulent flow at individual points (at some of which a small roughness element could be discovered) from which turbulence spreads in a wedge-like fashion downstream can be recognized in the picture. Measuring distance from the leading edge of the airfoil along the surface of the pressure and suction side, the following values were obtained for various angles of attack, for the range of start of transition to fully turbulent flow:

α (degrees)	Pressure side (inches)	Suction side (inches)
0	2 - 7	3 - 8
4	1 - 3	8 - 12
8.2	.5 - 1	12 - 16
12	0 - .2	14 - 19

For boundary layer calculations transition was assumed to occur at the mean position of the above values. The laminar boundary layer was calculated by the method developed by Waltz (16), the turbulent boundary layer by the procedure of Rotta (17). The computations were made using the experimental pressure distribution at an angle of attack of 4 degrees. The calculated and experimental values of the displacement thickness near the trailing edge (.965 c) are given in the table below:

	Pressure side	Suction side
Experiment	.0016	.0031
Calculated	.0023	.0054

In view of the bad agreement between theory and experiment in the calculations of the displacement thickness, the experimental and theoretical values have been checked very carefully. No errors could be found. Since the boundary layer calculations were very time consuming and not of prime importance in this investigation, no futher boundary layer calculations were made.

2.3.7 Effective airfoil thickness and velocity profiles near the trailing edge.

Figure 31 shows the trailing edge of the airfoil to which is added the displacement thickness of the boundary layer and wake for angles of attack of 0, 4, 8.2 and 12 degrees. For calculating the displacement thickness from the experimental data, the velocity in the bubble right behind the airfoil was assumed to be zero. The effective shape of the airfoil, shown dashed in Fig. 31, shows no abrupt changes near the trailing edge. It should be noted that the mean direction of the effective shape on the pressure and suction side determines the camberline used for the calculations in section 3, and therefore the circulation and lift on the airfoil.

The velocity profiles do not indicate a reversal in direction typical of flow separation, even at 12 degrees angle of attack. A definite change in slope at the wall can, however, be recognized. Along the line determined by the coincidence of the streamlines which separated from the pressure and suction surface, a very low velocity is measured. This velocity rapidly increases in the downstream direction as is characteristic of wake flow.

3 THEORETICAL CALCULATION OF LIFT

3.1 Previous Work

The theory of the potential flow around an airfoil, as introduced by Kutta and Joukowski has been extended to include arifoils of arbitrary cross-sectional shape (1). Using conformal mapping the airfoil is transformed into a circle, around which the flow is easily calculated. The circulation is fixed by assuming a stagnation point at the geometric center of the trailing edge. The assumption of an ideal fluid and the somewhat arbitrary definition of the position of the trailing edge stagnation point cause the value of the lift calculated in this manner to differ from the experimentally observed lift by as much as 30 percent (21) even when no flow separation can be observed in the experiment. The cause of this discrepancy must be sought in the difference of the potential flow model from the experimental flow, as follows:

1.) Along the surface of the airfoil surrounded by a viscous fluid a boundary layer is formed.

2.) At the trailing edge the pressure is roughly equal to the static pressure of the flow at infinity.

3.) Downstream of the airfoil exists a region of low energy fluid, the wake.

An analysis made by J. H. Preston (2) shows that the effect of the wake on the circulation around the airfoil is a decrease of the order of one half per cent; it therefore can be considered as a second order effect.

The boundary layer changes the effective shape of the airfoil by an amount equal to the displacement thickness of the boundary layer. As the displacement thickness is usually different for the pressure and suction surface, an uncambered airfoil may become effectively cambered, for example, or the effective camber may be smaller than the design camber.

Stüper (3), Pinkerton (4), Preston (5) and Spence (6) investigated this effect theoretically. Only the last two authors mentioned, whose theories are quite similar had accurate experimental results to check their theories.

In these theories, the magnitude of the circulation was fixed by the requirement that the main stream velocities at the edge of the boundary layer of the pressure and suction surface are equal. This theorem was originally suggested by G. I. Taylor (7) expressed mathematically by Howarth (8) and applied by the latter to the calculation of the lift on an elliptical cylinder. It results from the argument that in steady flow the circulation around the airfoil is constant with time; the rate of shedding of vorticity into the wake therefore has to be the same for the pressure and suction side. Mathematically this can be expressed as

$$\int_0^{\delta_p} W \frac{\partial W}{\partial \psi} d\psi = \int_0^{\delta_s} W \frac{\partial W}{\partial \psi} d\psi$$

or

$$\frac{1}{2} W_p^2 = \frac{1}{2} W_s^2$$

where W_p and W_s are the velocities at the edge of the boundary layer on the suction and pressure side, respectively, and the integrals are written for a streamline coordinate system. These experiments and those of Preston (5) have shown that $.95 < \frac{W_p}{W_s} < 1.05$, depending on the specific angle of attack and airfoil shape. This may be due to the inaccuracy in determining the two points at the edge of the boundary layer lying on the same normal to the streamlines passing the trailing edge. Another error may be introduced by the unsteadiness of the flow.

Using conformal mapping, adding the displacement thickness by means of a source distribution, Preston and Spence (5 and 6) obtain values for the calculated lift for an 11.8 per cent thick, symmetrical Joukowski airfoil and a 12/40 Piercy airfoil which agree within 3% with experiment. As the method is based on conformal mapping, the calculations involved are quite laborious for an airfoil of arbitrary shape.

3.2 Description of the Flow of a Viscous Fluid around an Airfoil

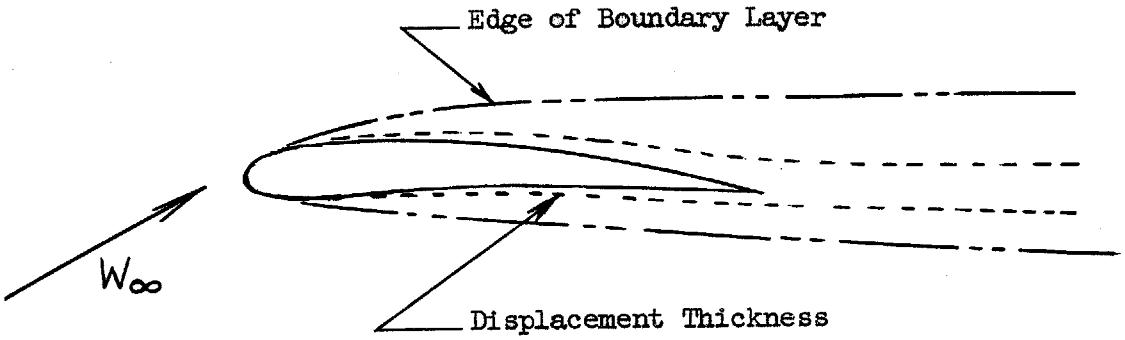

Figure 1. Flow of a viscous fluid around an airfoil.

The boundary layer which forms along the surface of the airfoil displaces the streamlines outside of the boundary layer by an amount equal to the displacement thickness δ^* defined by

$$\frac{\delta^*}{c} = \int_0^{\delta/c} \left(1 - \frac{u}{U}\right) d\left(\frac{y}{c}\right)$$

Near the leading edge, where the loading of the airfoil is highest, the displacement thickness is small and consequently also the change in effective shape of the airfoil. Towards the trailing edge the rate of growth as well as the magnitude of the displacement thickness increases. Assuming the airfoil operating in the unstalled region, the fluid will leave (separate from) the surface at the trailing edge in a direction essentially tangent to the surface of the pressure and suction side. If the trailing edge thickness is finite, say of the order of 0.02 c, the fluid will separate from the surface of the airfoil without flowing around the trailing edge, forming an air bubble (see section 2) as shown in Figure 2.

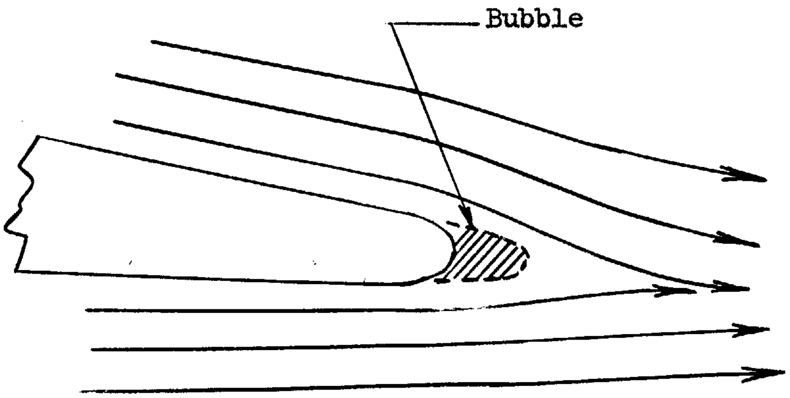

Figure 2. Flow around Trailing Edge of an Airfoil with Finite Trailing Edge Thickness.

The pressure at the surface of the airfoil in this region is approximately equal to the static pressure at infinity.

3.3 Application of Thin Airfoil Theory to the Flow of a Viscous Fluid around an Airfoil

3.3.1 General Aspects

In this section the basic features of thin airfoil theory will be reviewed. Similar presentations are given in References 9 - 11.

The first assumption in thin airfoil theory is that the y - coordinate of any point on the airfoil is small compared to the chord of the airfoil (Figure 3), the second that the flow around the cambered airfoil can be calculated from the superposition of the flow around a basic thickness form and an infinitely thin meanline.

The coordinates of the basic thickness form are obtained from

$$y_t = \frac{y_s - y_p}{2} \tag{1}$$

those of the meanline from

$$y_c = \frac{y_s + y_p}{2} \tag{2}$$

In complex coordinates the velocity induced at a point due to a singularity g (z)dz (source, sink or vortex) located at z is

$$u - iv = \frac{g(z)\,dz}{2\pi(z - \bar{z})} \tag{3}$$

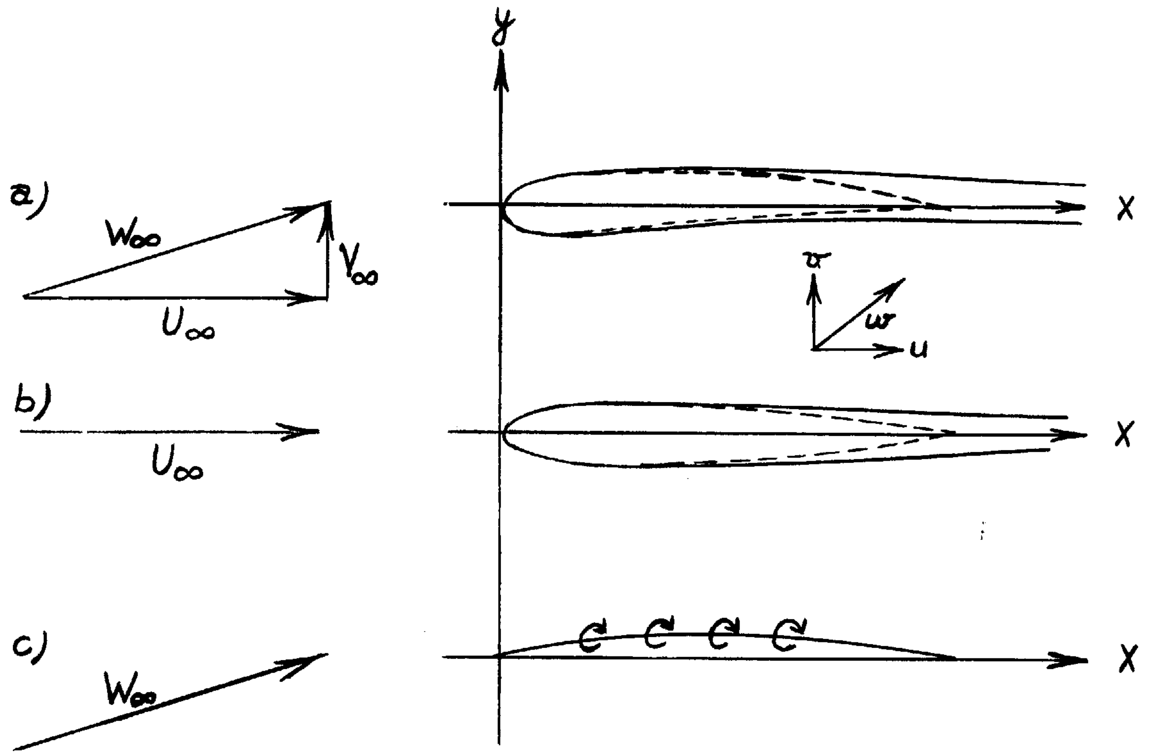

Figure 3. Coordinate System for Thin Air Foil Theory.

Thin airfoil theory assumes distributed sources and sinks for the "basic thickness airfoil" (Figure 3b) and a vortec distribution for the meanline (Figure 3c). The velocity on the surface of the airfoil of unit chord, i.e., a point $\bar{z}$ due to all singularities is then

$$u - iv = \frac{1}{2\pi}\int_0^1 \frac{g(z)\,dz}{z - \bar{z}} \tag{4}$$

It is assumed that the y - coordinate is small compared to the chord, and therefore $z - \bar{z} \approx x - \bar{x}$; also the singularities are located on the x - axis. One obtains then for the velocity induced in the x - direction at the surface of the basic airfoil (approximately the same as on the x - axis)

$$u = \frac{1}{2\pi}\int_0^1 \frac{q(x)}{x-\bar{x}}\,dx \tag{5}$$

and for the velocity induced normal to the meanline (approximately the same as normal to the x - axis)

$$v = \frac{1}{2\pi}\int_0^1 \frac{\gamma(x)}{x-\bar{x}}\,dx$$

where

$$g(z) \approx g(x) = q(x) + i\,\gamma(x)$$

3.3.2 Calculation of the Velocity Distribution of the Basic Thickness Airfoil.

The boundary condition for the basic airfoil is determined by writing the continuity equation for a small element of the airfoil (see Appendix 1). It follows

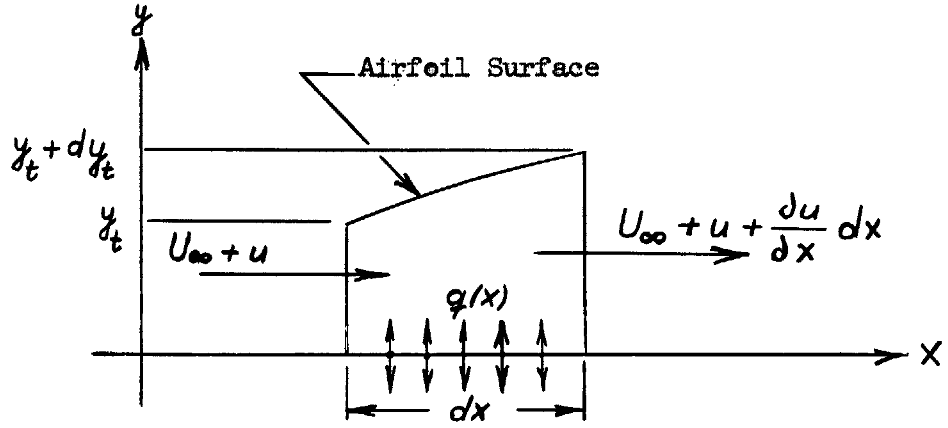

Figure 4. Flow through an Elemental Section of the Basic Thickness Airfoil.

$$\frac{1}{2} q(x)\,dx = U_\infty\, dy + \int_0^{y_t} \frac{\partial u}{\partial x}\, dx\, dy + \int_{y_t}^{y_t + dy_t} u\, dy \tag{7}$$

If $y_t \ll 1$, the variation of u between the x-axis and the surface of the airfoil is small and one can write

$$u = u(x, y) \approx u(x) \tag{8}$$

Equation (7) can then be written as

$$\frac{1}{2} q(x) = U_\infty \frac{dy_t}{dx} + \frac{d}{dx}(u \cdot y_t) \tag{9}$$

Thin airfoil theory usually neglects the second term of the right hand side of equation (9). Integrating equation (9) between the leading and trailing edge gives

$$\frac{1}{2}\int_0^1 q(x)\, dx = (U_\infty + u) y_t \Big|_0^1 \tag{10}$$

For a closed airfoil this integral equals zero as the sinks just balance the sources. For the airfoil surrounded by a viscous fluid the integral depends on the total thickness at the trailing edge, i. e. the thickness of the airfoil plus the displacement thickness of the boundary layers. (See Eq. 14).

The next step in the development is to assume q(x) as an infinite series of the form

$$q(x) = 2U_\infty \left(B_0 \operatorname{ctn} \frac{\varphi}{2} + \sum_1^\infty B_n \sin n\varphi\right) \tag{11}$$

with the coordinate transformation

$$\frac{x}{c} = \frac{1}{2}(1 - \cos\varphi) \tag{12}$$

If the coefficients B_n , $0 < n < \infty$, are known, one can calculate u from Eq. (5). To determine these coefficients one first substitutes (11) and (12) into (5) and the resulting equation into (9) and finds (see Appendix 2)

$$B_0\left(\operatorname{ctn}\frac{\varphi}{2} - \frac{dy_t}{dx}\right) + \sum_1^{\infty} B_n \sin n\varphi\left(1 - \frac{y_t}{c}\frac{2n}{\sin\varphi} + \frac{dy_t}{dx}\operatorname{ctn} n\varphi\right) = \frac{dy_t}{dx} \tag{13}$$

and from the substitution of (11), (12) and (5) into (10)

$$B_0 + \frac{1}{2}B_1 = \frac{2y_{te}}{\pi c}\left(1 + B_0 + B_1 - B_2 + B_3 - \ldots\right) \tag{14}$$

Neglecting u in Eqs. (9) and (10) leads to the equivalent of Eqs. (13) and (14) in the form

$$B_0 \operatorname{ctn}\frac{\varphi}{2} + \sum_1^{\infty} B_n \sin n\varphi = \frac{dy_t}{dx} \tag{15}$$

$$B_0 + \frac{1}{2}B_1 = \frac{2y_t}{\pi c} \tag{16}$$

Equations (15) and (16) are the equations of thin airfoil theory where the right hand side of Eq. (16) is taken equal to zero. Equation (15) can be integrated to give

$$\frac{1}{2}B_0(\varphi + \sin\varphi) + \frac{1}{8}B_1(2\varphi - \sin 2\varphi) + \frac{1}{12}B_2(3\sin\varphi - \sin 3\varphi) +$$

$$+ \frac{1}{16}B_3(2\sin 2\varphi - \sin 4\varphi) + \ldots = \frac{y_t}{c} \qquad (17)$$

Rather than fulfilling Eqs. (13) to (17) at every point along the airfoil, one uses only a finite number of terms, r, and determines B_0, B_1, . . . B_r by writing the equations at r points and solving the resulting set of r simultaneous equations for the unknowns B_n.

Having determined the B_n's, the velocity distribution at the surface of the airfoil is found from the substitution of Eqs. (11) and (12) into Eq. (5) to give (see Appendix 2)

$$\frac{u}{U_\infty} = B_0 - \sum_1^r B_n \cos n\varphi \qquad (18)$$

As this is the component of the induced velocity in the x-direction on the x-axis, one can calculate the velocity tangential to the airfoil surface, w, approximately by

$$\frac{w}{U_\infty} = \frac{u}{U_\infty} \frac{1}{\sqrt{1 + {dy_t/dx}}} \qquad (19)$$

Summarizing, the steps in the calculation of the velocity distribution around the basic thickness airfoil are

1) Determine the coefficients B_n from Eqs. (13) and (14), (15) and (16) or (16) and (17) by selecting r points along the airfoil

to give r simultaneous equations. For airfoils of maximum thickness smaller than 0.12 c, Eqs. (16) and (17) give good agreement with experiment; for thicker airfoils Eqs. (13) and (14) are recommended.

2) Calculate u/U from Eq. (18).

3) The velocities at the surface of the airfoil are then determined from Eq. (19).

3.3.3 Calculation of the velocity distribution around the meanline.

For a cambered airfoil or for an airfoil at angle of attack the flow around the infinitely thin meanline (Eq. 2) has to be solved in addition to the flow around the basic thickness airfoil.

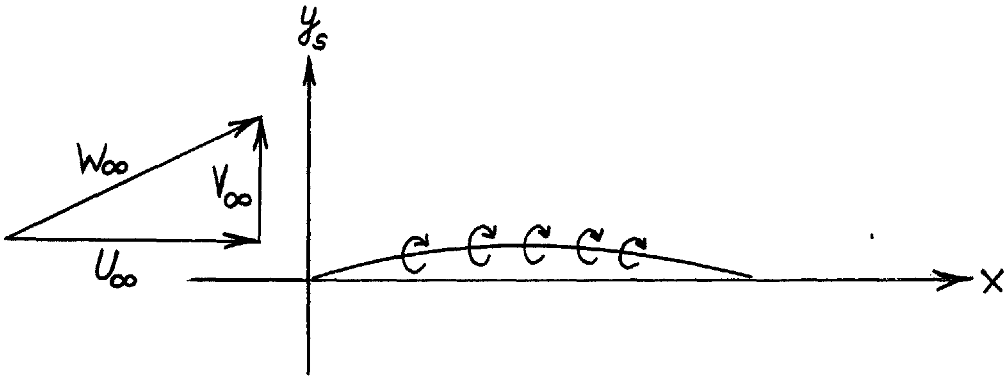

Figure 5. Flow around the meanline.

The boundary condition for this problem is given by the condition that no flow occurs across the meanline, i. e. that the meanline becomes a streamline. Remembering that this flow is superimposed on the flow around the basic thickness airfoil, denoting by subscripts q the velocities induced by the source and sink distribution of that solution, and by subscripts γ the velocities induced by the vortex distribution of Fig. 5, the boundary condition is expressed mathematically by

$$\frac{V_\infty + v_q + v_\gamma}{U_\infty + u_q + u_\gamma} = \frac{dy_c}{dx} \qquad (20)$$

v_q is the velocity induced at the meanline (approximately equal to the camberline) due to the source and sink distribution of the basic thickness airfoil. It is of opposite sign above and below the meanline; on the meanline, however, this velocity is equal to zero. A similar argument can be made for the term u_γ. According to thin airfoil theory the position of the meanline is approximated by its projection on the x-axis. u_γ then has opposite signs on each side of the x-axis and is parallel to it; on the x-axis itself, however, it becomes zero.

Under the assumption of thin airfoil theory, v_q and u_γ are therefore equal to zero on the meanline. But even without these assumptions it can be shown that their magnitude compares to the magnitude of v_γ and u_q as $\sin^2\epsilon$ to $\cos^2\epsilon$, where ϵ is the slope of the meanline. Equation (20) therefore becomes

$$\frac{V_\infty + v_\gamma}{U_\infty + u_q} = \frac{dy_c}{dx} \qquad (21)$$

which is equivalent to

$$\frac{v_\gamma}{U_\infty} = \frac{dy_c}{dx}\left(1 + \frac{u_q}{U_\infty}\right) - \alpha \qquad (22)$$

where $\alpha = V_\infty/U_\infty$, i. e. the tangent of the angle of attack on the airfoil. Thin airfoil theory assumes $u_q/U_\infty \approx 0$. A comparison of the different quantities of Eq. (20), calculated for an 11.8 per cent thick symmetrical Joukowski airfoil at an angle of attack of 6 degrees is shown in Fig. 7.

The further development of this section is quite similar to the solution for the flow around the basic thickness airfoil. The vortex distribution is assumed in the form

$$\gamma(x) = 2U_\infty\left(A_0 \operatorname{ctn}\frac{\varphi}{2} + \sum_1^\infty A_n \sin n\varphi\right) \tag{23}$$

Substituting this into Eq. (4) gives

$$\frac{v}{U_\infty} = A_0 - \sum_1^\infty A_n \cos n\varphi \tag{24}$$

To determine the coefficients A_n, Eq. (24) is introduced into Eq. (22) to give

$$A_0 - \sum_1^\infty A_n \cos n\varphi = \frac{dy_c}{dx}\left(1 + \frac{u_q}{U_\infty}\right) - \alpha \tag{25}$$

Approximating the infinite series in Eq. (25) by r terms, one again obtains r simultaneous equations for the solution of the coefficients A_0, A_1, A_2 . . . A_r .

Across the vortex sheet, represented by the meanline, occurs a discontinuity in velocity at a point x of magnitude $\gamma(x)$. The induced velocity in the x-direction at the surface of the airfoil is therefore on the suction surface

$$\frac{u_s}{U_\infty} = 1 + \frac{u_q}{U_\infty} + \frac{u_\gamma}{U_\infty}$$

$$\frac{u_s}{U_\infty} = 1 + \frac{u_q}{U_\infty} + \frac{1}{2}\gamma(x) \tag{26}$$

and on the pressure surface

$$\begin{aligned}\frac{u_p}{U_\infty} &= 1 + \frac{u_q}{U_\infty} - \frac{u_\gamma}{U_\infty} \\ &= 1 + \frac{u_q}{U_\infty} - \frac{1}{2}\gamma(x)\end{aligned} \tag{27}$$

3.3.4 Calculation of the lift coefficient.

As shown by G. I. Taylor (7) the lift on an airfoil in a viscous fluid is given by the Kutta-Joukowski theorem

$$L = \rho W_\infty \Gamma$$

provided Γ is determined around a circuit at the boundary of which the disturbance caused by the airfoil is small compared to the velocity at infinity. He suggests that this is approximately true for a circuit close to the airfoil. This is shown to be correct by J. H. Preston (2) by an analysis which indicates that the net circulation in the wake is small. The lift coefficient is therefore

$$\begin{aligned}c_\ell &= \frac{L}{\frac{1}{2}\rho W_\infty^2 c} \\ &= \frac{\rho W_\infty \Gamma}{\frac{1}{2}\rho W_\infty^2 c}\end{aligned}$$

As $\Gamma = \int_0^1 \gamma(x)\,dx$ the lift coefficient can be written as

$$c_\ell = 2\left(A_0 + \frac{1}{2}A_1\right)\cos\alpha \tag{28}$$

3.3.5 Summary of the solution for the flow of a viscous fluid around an airfoil.

To determine the lift on an airfoil submerged in a real fluid by this method, the displacement thickness of the boundary-layer along the pressure and suction surface of the airfoil is assumed to be known.

One first plots the airfoil plus displacement thickness, added to the surface of the airfoil, in a large scale and determines the basic thickness airfoil, Eq. (1), and the meanline, Eq. (2). From past calculations it was concluded that a four term approximation to the infinite series of Eqs. (11) and (23) give good agreement with experiment. One therefore determines the coordinates and slopes of the basic thickness airfoil and the meanline at four stations along the chord of the airfoil, one of which is the trailing edge. It is suggested that the other three stations are chosen such as to define the shape at characteristic points (like, for example, the point of maximum thickness) of the airfoil rather than at three fixed stations, independent of the airfoil shape, as proposed in Reference 11.

If the airfoil has a maximum thickness greater than about 0.12 c, one calculates the coefficients B_n from the simultaneous equations

$$\begin{aligned} &B_0\left(\operatorname{ctn}\frac{\varphi_r}{2}-\frac{dy_{tr}}{dx}\right)+B_1\left(\sin\varphi_r-\frac{2y_{tr}}{c}+\frac{dy_{tr}}{dx}\cos\varphi_r\right)+B_2(\sin 2\varphi_r - \\ &-8\frac{y_{tr}}{c}\cos\varphi_r+\frac{dy_{tr}}{dx}\cos 2\varphi_r)+B_3[\sin 3\varphi_r-6\frac{y_{tr}}{c}(1+2\cos\varphi_r)+ \\ &\qquad +\frac{dy_{tr}}{dx}\cos 3\varphi_r=\frac{dy_{tr}}{dx} \end{aligned} \tag{29}$$

and

$$B_0+\frac{1}{2}B_1 = \frac{2}{c}\frac{y_{te}}{\pi}\left(1+B_0+B_1-B_2+B_3\right) \tag{14}$$

where r = 1, 2, 3.

For airfoils below 0.12 maximum thickness good agreement with experiment is obtained by using the equations

$$\frac{1}{2}B_0(\varphi_r+\sin\varphi_r)+\frac{1}{8}B_1(2\varphi_r-\sin 2\varphi_r)+\frac{1}{12}B_2(3\sin\varphi_r-\sin 3\varphi_r) + \\ + \frac{1}{16}B_3(2\sin\varphi_r-\sin 4\varphi_r) = \frac{y_t}{c} \tag{30}$$

and

$$B_0+\frac{1}{2}B_1 = \frac{2}{c}\frac{y_{te}}{\pi} \tag{16}$$

Having determined the coefficients by either Eqs. (29) and (14) or Eqs. (30) and (16), the velocity distribution for the basic thickness airfoil is calculated from

$$\frac{u_\varphi}{U_\infty} = B_0 - B_1\cos\varphi - B_2\cos 2\varphi - B_3\cos 3\varphi \tag{31}$$

Superimposed on the basic thickness airfoil is the flow around the meanline. At first sight one would replace the chordline of the original airfoil by that due to the airfoil with boundary-layer and make the calculations based on the x' - y' coordinate system, rather than the x - y coordinate system as is usually done. It is proposed, however, to keep the original coordinate system for the following reason:

The boundary condition for the meanline solution is given by Eq. (22)

$$\frac{v_r}{U_\infty} = \frac{dy_c}{dx}\left(1+\frac{u_\varphi}{U_\infty}\right) - \alpha \tag{22}$$

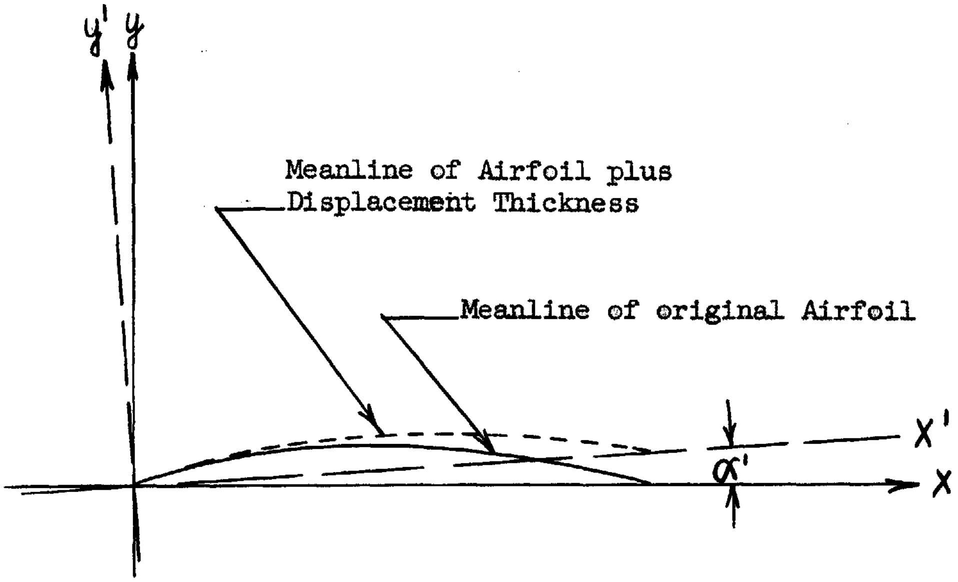

Figure 6. Change in meanline due to the displacement thickness of the boundary-layer.

If $u_q = 0$, i. e. for an airfoil consisting only of an infinitely thin meanline, the right hand side of Eq. (22) would not be changed by a rotation of the coordinate system by the angle α'. (Thin airfoil theory assumes $u_q \approx 0$ in Eq. (22) for airfoils of finite thickness). As, however, in this solution $u_q \neq 0$, i. e. the effect of thickness is included in Eq. (22), a rotation of the reference coordinate system would change the right hand side of Eq. (22). Solving then for the pressure distribution, this results in a higher loading than is actually the case. This may be explained in the folowing way:

The A_0 - term in the solution for the flow around the meanline represents the induced velocities due to a flat plate airfoil. The following terms, A_n , $n > 0$, are of second order and account for the difference in the meanline from the flat plate. A change in the reference coordinate system means a change of the flat plate solution, i. e. the first order term if $u_q \neq 0$.

The change in the meanline due to the displacement thickness is, however, definitely a second order effect and must be included as such in the theory. This is the case if the reference coordinate system is not changed. In calculating the effect on the circulation due to the boundary-layer, the term dy_c/dx in Eq. (22) is therefore determined with respect to the original x - y coordinate system, formed by the chord line of the airfoil without boundary layer.

Using again a four-term approximation to the infinite series in Eq. (23), the simultaneous equations for the determination of the coefficients A_n are

$$A_0 - A_1\cos\varphi_r - A_2\cos 2\varphi_r - A_3\cos 3\varphi_r = \frac{dy_c}{dx}\left(1+\frac{u_q}{U_\infty}\right) - \alpha \qquad (32)$$

where r = 1, 2, 3.

The induced velocity at the surface of the meanline follows then from

$$\frac{u_\gamma}{U_\infty} = \pm\left(A_0 \operatorname{ctn}\frac{\varphi}{2} + A_1\sin\varphi + A_2\sin 2\varphi + A_3\sin 3\varphi\right) \qquad (33)$$

where the plus and minus sign refers to the suction, respectively pressure side of the meanline.

The total velocity at the surface of the airfoil is then calculated from

$$\frac{W}{W_\infty} = \frac{W}{U_\infty}\cos\alpha$$

$$= \frac{1}{\sqrt{1+\left(\frac{dy}{dx}\right)^2}}\left(1 + \frac{u_q}{U_\infty} \pm \frac{u_\gamma}{U_\infty}\right)\cos\alpha \qquad (34)$$

where the plus and minus signs are again written for the pressure and suction side, respectively, and dy/dx is the corresponding slope at the surface of the airfoil plus displacement thickness.

The lift coefficient is calculated from Eq.(28):

$$c_\ell = 2\pi \left(A_0 + \frac{1}{2} A_1\right) \tag{28}$$

Concluding this section it is emphasized that the above outlined procedure has to be repeated for each angle of attack as the displacement thickness changes with angle of attack. A significant simplification, without effecting appreciably the accuracy of the calculated results, may be made by neglecting the change in velocity distribution of the basic thickness airfoil due to the displacement thickness and repeating only the calculations depending on the coefficients A_n.

3.3.6 Comparison with experiment.

The calculation procedure outlined above was used to calculate the lift coefficient and pressure distribution for a 11.8 per cent thick symmetrical Joukowski airfoil and a 12/40 Piercy airfoil for which the experimentally determined displacement thickness along the surface of the airfoil and the pressure distribution were known (5, 19, 20). Both airfoils were at an angle of attack of 6 degrees. The comparison between theory and experiment with respect to pressure distribution is shown in Figs. 8 and 9. The table below summarizes the results of the calculations of the lift coefficients, together with calculations made by Preston (5) and Spence (6) using conformal mapping.

	Modified thin airfoil theory		Preston		Spence		Experiment
	C_{l_o}	C_l	C_{l_o}	C_l	C_{l_o}	C_l	C_l
Joukowski Airfoil $\alpha = 6°$	.657	.594	.694	.633*	.694	.631*	.612
12/40 Piercy Airfoil $\alpha = 6°$	.657	.537	.774	.561*	.774	.561*	.538

* Based on the experimental velocity at the edge of the boundary layer
C_{l_o} = calculated lift coefficient for unmodified airfoil
C_l = lift coefficient calculated for airfoil with boundary layer.

It is of interest to note that the lift coefficient for an uncambered airfoil, calculated by thin airfoil theory, is a function of the angle of attck only. It is independent of the airfoil shape, and represents the lift coefficient of a flat plate. The uncorrected lift coefficient C_{l_o} , calculated by thin airfoil theory is lower than the lift coefficient calculated by conformal mapping.

4 ELECTRICAL ANALOG

Due to the straight tunnel walls a theoretical solution for the flow around the airfoil, used in the experiment, would have been quite difficult. A relaxation solution would be too laborious; the only other way would be to apply the tunnel wall corrections in reverse, i.e., compute the flow around the airfoil in an infinite medium and then calculate the effect of the tunnel walls.

A much more attractive method presented itself in the electrical analog. The two possibilities were the electrolytic tank (Reference 18) or the uniform plane conductor, i.e. Teledeltos paper (a product of the Union Telegraph Co.). As the former was not directly available and in any case would require a one half to one third scale model of the actual experiment, it was decided to use Teledeltos paper, even though the non-uniformity of the paper decreases the accuracy.

The Teledeltos paper is evenly coated with graphite and has a resistance of about 3000 Ohms per centimeter. The constant voltage boundaries, corresponding to streamlines in the analogy, were represented by gluing flat rolled braided wire shielding to the surface of the paper, assuring electrical contact by the application of Du Pont made No. 4922 silver paint. Streamlines were traced by using a pointed metal probe, connected through a microammeter to a continuously variable rheostat. A schematic drawing of the set up for the electrical analog is shown in Figure 32, a photograph of the actual set up in Figure 33.

4.1 Characteristics of the Teledeltos Paper.

Tests were made to check the uniformity of the paper by setting up a model of the uniform flow in a two-dimensional duct.

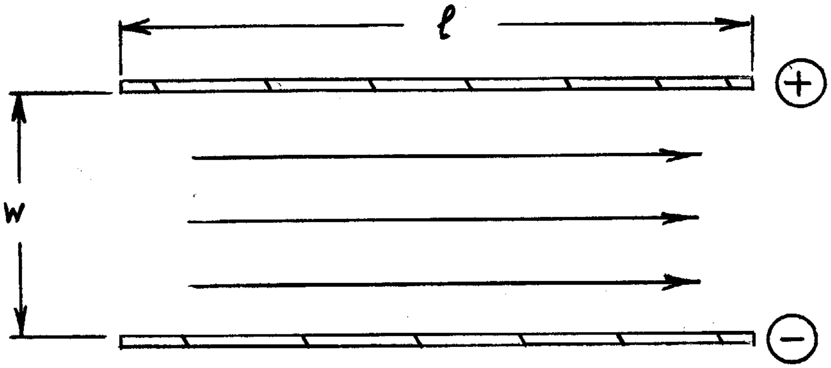

Dividing w into 10 equal parts using the measuring probe, connected to the rheostat, the latter being adjusted to 10 equal voltage increments, gave a maximum deviation of .05 inches from the geometric division. The streamlines were parallel to the terminals if ℓ was taken along or perpendicular to the roll of paper. If ℓ was taken at 45 degrees to the longitudinal direction of the roll the streamlines were inclined 2 degrees with respect to ℓ in the center decreasing gradually to 0 degrees as the terminals were approached.

Another test of the uniformity of the paper was made using the potential vortex. The results of this flow showing the deviation between the computed and measured streamlines, are shown in Figure 34.

4.2 Gradient Measurements.

If ψ is the stream function of the flow, the velocity at a point is given by the gradient of ψ at that point. As constant ψ - lines were analogous to constant voltage lines it was necessary to measure the voltage gradients on the paper.

For this purpose a probe with three needle points, extending below a lucite plate, was constructed (Figure 34). Referring to the figure on the left, the three needle points are represented by the points 1, 2 and 3, the gradient to be measured is at P. In the first step for the gradient measurements, terminals 1 and 2 are connected to a Leeds and Northrup potentiometer (Range .01 to 80.5 mV). The probe was then turned until no potential difference was indicated, i.e. points 1 and 2 were located on the same streamline. The gradient at P was then taken as the arithmetic mean of the potential difference between point 1 - 3 and 2 - 3, divided by the height of the triangle 1 - 2 - 3 with 1 - 2 as base. The distance between the probe terminals was approximately .125 inches. The exact distance was not determined as all gradient measurements were nondimensionalized by the gradient measured with the same probe for uniform upstream flow.

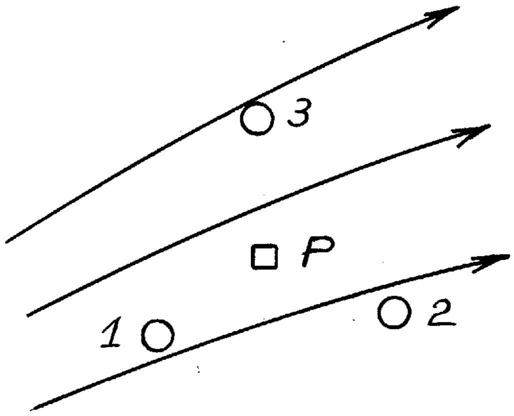

To explore the reliability of the data for gradients obtained in this way tests were made on uniform flow fields, similar to the one used in section 4.1, of length ℓ and width w, the results of which are presented in the table below. The error is expressed as per cent deviation from the arithmetic mean of all readings.

l	w	Maximum Deviation Per cent	Minimum Deviation Per cent	Mean Deviation Per cent	Number of Readings
20	30	4.5	- .3	0.3	12
20	20	-3.5	- .4	-0.4	11
20	20	-4.8	1.2	0.4	11
10	18	3.3	-1.1	-1.5	6
10	18	-6.6	-1.1	0.1	6

Similar measurements were made on the potential vortex analog. The mean deviation from the calculated gradients was 2 and 2.8 per cent for two sets of readings.

It was concluded that velocity can be determined from the electric analog using Teledeltos paper within error limits of ±1.5 per cent of the correct value.

4.3 Electrical analog for the airfoil in the tunnel at an angle of attack of 4 degrees.

As the Teledeltos paper is available in a maximum width of 31 inches a 1/3 scale model of the airfoil in the tunnel with straight walls was first set up. The circulation was fixed by the requirement that the stagnation streamline, which has the same potential as the airfoil, should leave the trailing edge at the geometric center. From the one third scale model two streamlines were determined, having a maximum distance of 10 inches between then, one being on each side of the airfoil. The coordinates of these two streamlines were recorded and a full scale model was constructed. The pressure distribution around the airfoil, shown in Figure 36, was determined by measuring the gradients on this model. The agreement in pressure distribution with experiment is fair, the integrated value of the force coefficient normal to the chord agrees to within less than 1 per cent with experiment. One would expect that the theoretical force coefficient is higher than that determined experimentally; the good agreement between the analog and the experiment must therefore be considered accidental.

It was then tried to add the displacement thickness of the boundary layer and the wake in the analog. The position of the wake was determined from experiment to a distance of .08 c downstream of the airfoil, from where it was assumed that the displacement thickness stays constant and follows the direction of the stagnation streamline leaving the trailing edge in the potential flow model. To fix the circulation, the same front stagnation point was assumed as determined experimentally for the flow in the tunnel.

Although good agreement with experiment in pressure distribution is obtained for the suction side, the velocities indicated on the pressure side are too low, i.e. the pressure is too high (Figure 37). The force normal to the chord is therefore 15 per cent higher than the experimental value. The large discrepancy is probably due to the uncertainty in determining the front stagnation point by experiment.

Concluding it can be said that the electrical analog is a quick and easily understood method for the determination of the potential flow around an airfoil, giving results which are within the range of discrepancy between experimental results and exact potential flow computations. The analog cannot be used to determine the effect of the displacement thickness of the boundary layer and wake due to the difficulty in establishing the circulation.

5 CONCLUSIONS

5.1 Experimental results

A change in trailing edge contour from the semi-circular to first a square and then a cusped trailing edge had no perceptible effect on the pressure distribution, and consequently the lift, of the airfoil.

Drag calculations, however, gave a 13 per cent higher drag coefficient for the square trailing edge and an 8 per cent lower drag coefficient for the cusped trailind edge than for the semi-circular trailing edge. The difference was accounted for by the change in pressure drag on the specific trailing edge.

Visualization of transition by means of cobalt chloride indicated the start of transition at isolated spots, from where turbulence spread downstream in a wedgelike fashion.

Measurements show a bubble of low energy fluid extending approximately 0.04 c beyond the trailing edge of the airfoil. The size of the bubble was essentially independent of the angle of attack. This region was characterized by two other phenomena:

1.) Relatively large aperiodic flow fluctuations were observed.

2.) The flow pattern inside the bubble, as shown by lamp black traces, showed the existence of two small vortices, one on each side of the extension of the chord line. The strength of these vortices depended on the specific shape of the airfoil trailing edge as well as the angle of attack. For a semicircular trailing edge the strength was of the order of one half per cent of the circulation around the arifoil. As the angle of attack was increased, the vortex on the suction side increased in strength, while close to stall the vortex on the pressure side vanished.

The bubble extends the airfoil downstream, virtually making a thin trailing edge. When adding the displacement thickness of the boundary layer, including the bubble, to the airfoil a continuous effective contour resulted. From this it was concluded that a potential flow theory, fulfilling the boundary condition of the effective airfoil shape and including the displacement thickness of the wake, should give good agreement with experiment.

5.2 Theoretical Calculations

Thin airfoil theory modified to include terms of second order was used to calculate the decrease in lift on an airfoil due to the boundary layer. This theory presents a fairly simple way of calculating the lift and the pressure distribution in two-dimensional flow provided the displacement thickness of the boundary layer is known along the surface of the airfoil. The agreement with experiment for two symmetrical airfoils, a 11.8 per cent thick Joukowski airfoil and a 12/40 Piercy airfoil is good. To prove its general validity for airfoils with camber more experimental data are needed.

5.3 Electrical Analog

A theoretical solution for the potential flow around the modified NACA 0015 airfoil in the tunnel was obtained by the use of Teledeltos paper. A special probe was constructed, by means of which the velocity could be directly determined from the analog. The analog fails, however, if the displacement thickness of the boundary layer and the wake is added to the potential flow model due to the difficulty in fixing the circulation.

APPENDIX A

Derivation of the boundary condition for the basic airfoil (equation 7).

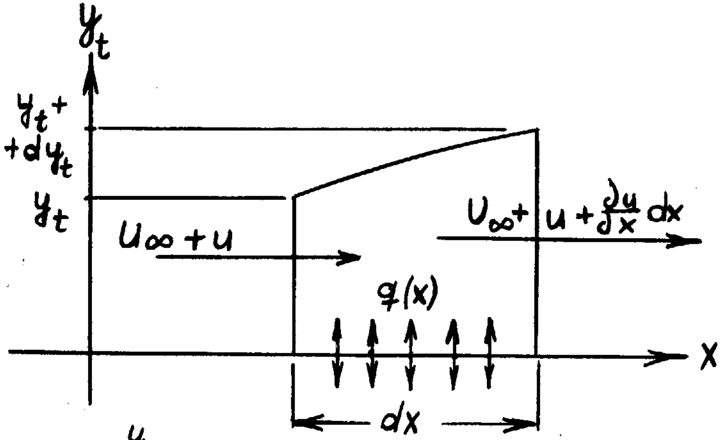

Writing the continuity equation for the airfoil element shown at the left gives:

$$U_\infty y_t + \int_0^{y_t} u\,dy + \frac{1}{2}q(x)\,dx = U_\infty(y_t + dy_t) + \int_0^{y_t+dy_t}\left(u + \frac{\partial u}{\partial x}dx\right)dy$$

$$U_\infty y_t + \int_0^{y_t} u\,dy + \frac{1}{2}q(x)\,dx = U_\infty y_t + U_\infty dy_t + \int_0^{y_t} u\,dy + \int_{y_t}^{y_t+dy_t} u\,dy +$$
$$+ \int_0^{y_t}\frac{\partial u}{\partial x}dx\,dy + \int_{y_t}^{y_t+dy_t}\frac{\partial u}{\partial x}dx\,dy$$

which becomes, neglecting the last, second order term

$$\frac{1}{2}q(x)\,dx = U_\infty dy_t + \int_0^{y_t}\frac{\partial u}{\partial x}dx\,dy + \int_{y_t}^{y_t+dy_t} u\,dy$$

If $u = u(x,y) \approx u(x)$, the above equation is changed to

$$\frac{1}{2}q(x)\,dx = U_\infty dy_t + du\,y_t + u\,dy_t$$

or

$$\frac{1}{2}q(x) = U_\infty\frac{dy_t}{dx} + \frac{d}{dx}(u\,y_t)$$

APPENDIX B

Determination of the coefficients B_n for the sink and source distribution (equation 13).

Substituting (11) and (12) into (5) gives

$$u = \frac{1}{2\pi}\int_0^{\pi} \frac{2U_\infty\left(B_0 \operatorname{ctn}\frac{\varphi}{2} + \sum_1^\infty B_n \sin n\varphi\right)}{\frac{1}{2}(\cos\varphi - \cos\overline{\varphi})} \cdot \frac{1}{2}\sin\varphi \, d\varphi \qquad (B\cdot1)$$

For the integration the formula

$$\int_0^{\pi} \frac{\cos n\varphi}{\cos\varphi - \cos\overline{\varphi}}\, d\varphi = \pi \frac{\sin n\varphi}{\sin\varphi}$$

is very helpful. One obtains then

$$\int_0^{\pi} \frac{\operatorname{ctn}\frac{\varphi}{2}\sin\varphi}{\cos\varphi - \cos\overline{\varphi}}\, d\varphi = \pi$$

$$\int_0^{\pi} \frac{\sin^2\varphi}{\cos\varphi - \cos\overline{\varphi}}\, d\varphi = -\pi\cos\varphi$$

$$\int_0^{\pi} \frac{\sin 2\varphi \sin\varphi}{\cos\varphi - \cos\overline{\varphi}}\, d\varphi = -\pi\cos 2\varphi$$

etc., so that equation (A-1) becomes

$$u = U_\infty\left(B_0 - \sum_1^\infty B_n \cos n\varphi\right) \qquad (B\cdot2)$$

From the combination of equation (A-2) and equation (9) follows

$$U_\infty\left(B_0 \operatorname{ctn}\frac{\varphi}{2} + \sum_1^\infty B_n \sin n\varphi\right) = U_\infty \frac{dy_t}{dx} + 2\frac{y_t}{c} U_\infty \cdot$$

$$\cdot \sum_1^\infty \frac{nB_n \sin n\varphi}{\sin\varphi} + \frac{dy_t}{dx} U_\infty\left(B_0 - \sum B_n \cos n\varphi\right)$$

or

$$B_0\left(\operatorname{ctn}\frac{\varphi}{2} - \frac{dy_t}{dx}\right) + \sum_1^\infty B_n \sin n\varphi\left(1 - \frac{y_t}{c}\frac{2n}{\sin\varphi} + \frac{dy_t}{dx} \operatorname{ctn} n\varphi\right) =$$

$$= \frac{dy_t}{dx}$$

APPENDIX C

Airfoil Coordinates

$\frac{x}{c}$	Modified NACA 0015 Profile. ±y/c	Piercy 12/40 Airfoil ±y/c	Joukowski Airfoil ±y/c
0	0	0	0
.025	.0327	.0201	.0276
.05	.0444	.0273	.0376
.075	.0525	.0337	.0443
.1	.0585	.0390	.0491
.2	.0717	.0520	.0581
.3	.0750	.0578	.0583
.4	.0725	.0598	.0534
.5	.0662	.0577	.0454
.6	.0570	.0523	.0356
.7	.0460	.0447	.0250
.8	.0351	.0327	.0145
.9	.0243	.0185	.0055
1.0	0	0	0
	r = .015*		

*Trailing edge radius.

BIBLIOGRAPHY

1. Garrick, I. E., "On the Plane Potential Flow Past a Lattice of Arbitrary Airfoils, NACA Rep. No. 788.

2. Preston, J. H., "Note on the Circulation in Circuits which cut the Streamlines in the Wake of an Aerofoil at Right-Angles", R and M No. 2957, 1956.

3. Stuper, J., "Auftriebsverminderung eines Flügels durch seinen Widerstand, Z. F. M. 24, 1933.

4. Pinkerton, R. M., "Calculated and Measured Pressure Distributions over the Midspan Section of NACA 4412 Aerofoil", NACA T. R. 563, 1936.

5. Preston, J. H., "The Calculation of Lift Taking Account of the Boundary Layer", R and M No. 2725, 1953.

6. Spencer, D. A., "Prediction of the Characteristics of Two-Dimensional Airfoils", Journal Aero. Sci. Vol. 21, No. 9, September 1954.

7. Bryant, E. W. and Williams, D. H., "An Investigation of the Flow around an Aerofoil of Infinite Span", R and M 989, 1924, Appendix by G. I. Taylor).

8. Howarth, L., "The Theoretical Determination of the Lift Coefficient of a Thin Elliptic Cylinder", Proc. Roy. Soc. A, 149, 1935.

9. Munk, Max, M., "Elements of the Wing Section Theory and of the Wing Theory", NACA Rep. No. 191, 1924.

10. Allen, J. H., "General Theory of Airfoil Sections having Arbitrary Shape or Pressure Distribution", NACA TR. No. 833, 1954.

11. Schlichting, H., "Berechnung der reibungslosen inkrompressiblen Strömung für ein vorgegebenes ebenes Schaufelgitter", V D I - Forschungsheft 447, 1955.

12. Riegels, F., "Das Umströmungsproblem bei in'ompressiblen Potentialströmungen", Ing. Arch. Vol. 16, 1948.

13. Lamb, Horace, Hydrodynamics 6th Edition, Dover Publication, pp. 84-85.

14. Allen, Julian, H. and Vincenti, Walter G., "Wall Interference in a Two-Dimensional flow Wind Tunnel, with Consideration of the Effect of Compressibility".

15. Jones, Melvill B., "Measurement of Profile Drag by the Pitot - Traverse Method", R and M No. 1688, 1936.

16. Walz, A., "Anwendung des Energiezatzes von Wieghardt auf ein-parametrige Geschwindigkeitsprofile in laminaren Grenzschichten", Ing. Arch. 16, p. 243, 1947.

17. Rotta, J., "Näherungsverfahren zur Berechnung turbulenter Grenzschichten unter Benützung des Energiesatzes", Mitteilung aus dem Max-Plank Institut fur Strömungsforschung, Nr. 8, 1953.

18. Malavard, L. C., "The Use of Rheoelectrical Analogies in Aerodynamics", AGARDograph 18, August 1956.

19. Preston, J. H., Sweeting, N. E., Cox, D. K., "The Experimental Determination of the Two-Dimensional Interference on a Large Chord Piercy 12/40 Aerofoil in a Closed Tunnel Fitted with a Flexible Roof and Floor", R and M No. 2007, 1944.

20. Preston, J. H., Sweeting, N. E., "The Experimental Determination of the Boundary Layer and Wake Characteristics of a Simple Joukowski Aerofoil, with Particular Reference to the Trailing Edge Region", R and M No. 1998, 1943.

21. Abbott, Ira H., Von Doenhoff, Albert E., Stivers, Louis, S. "Summary of Airfoil Data", NACA Rep. 824, 1945.

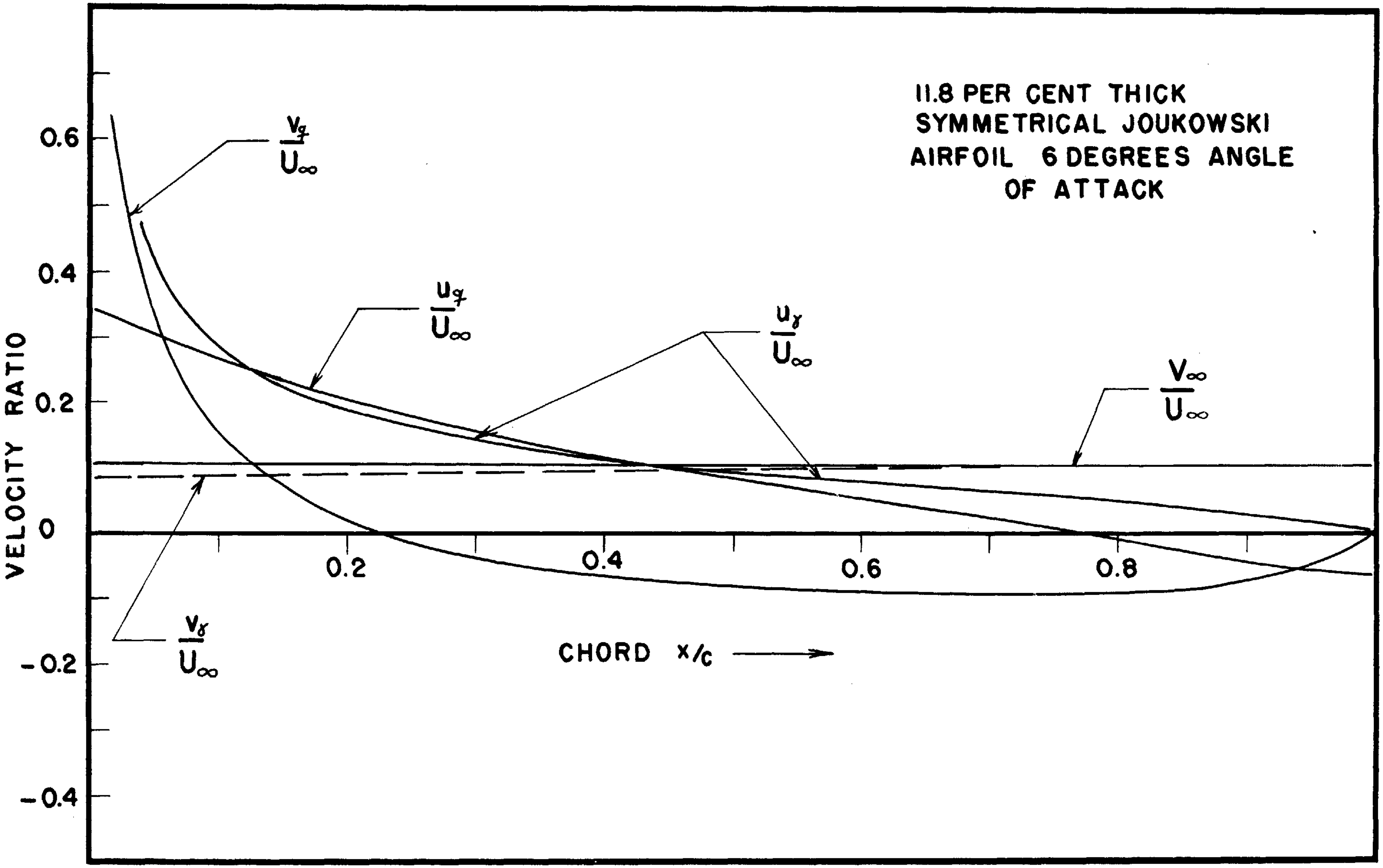

FIG. 7 – RELATIVE MAGNITUDE OF THE INDUCED VELOCITIES IN THIN AIRFOIL THEORY

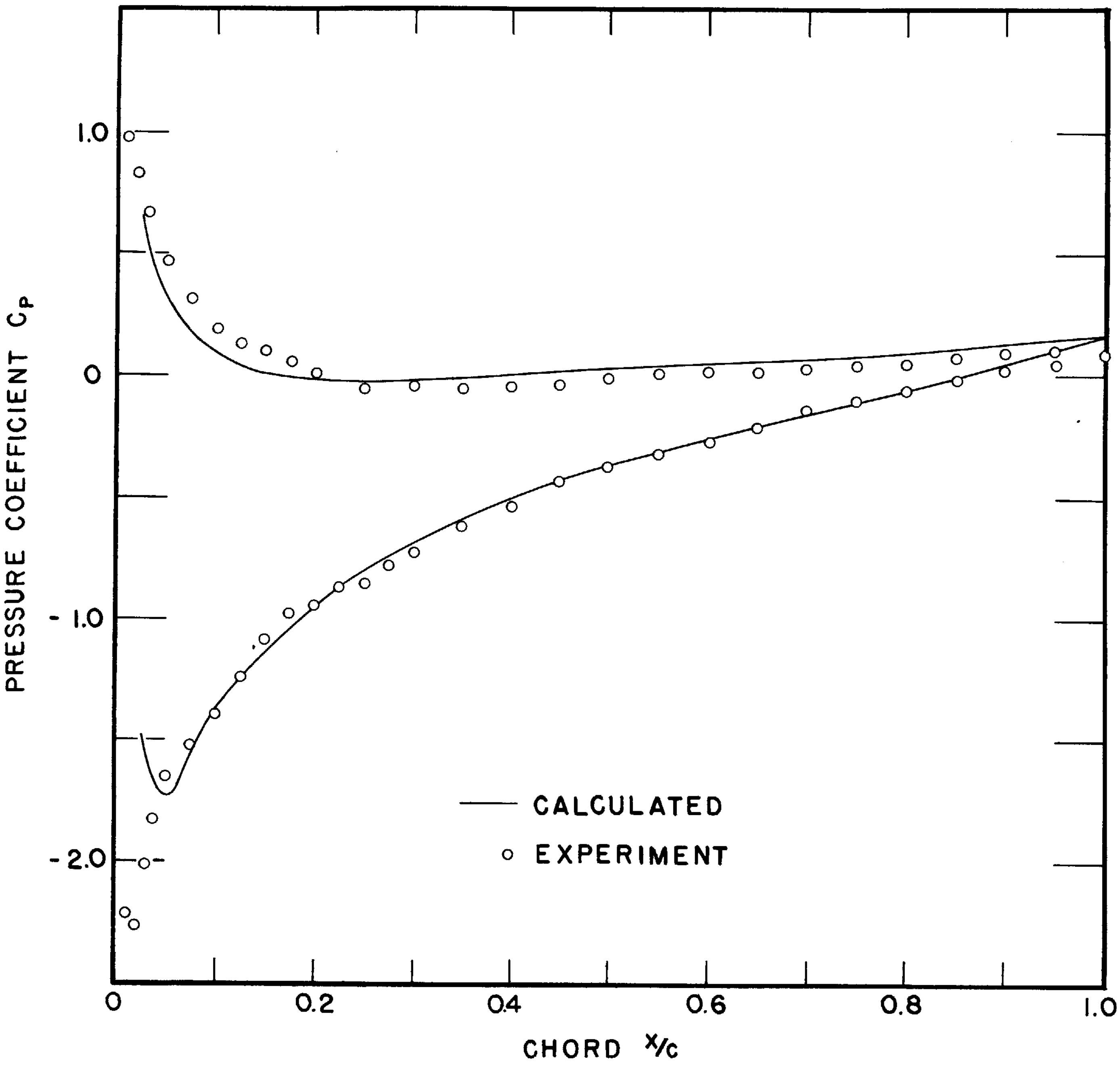

FIG. 8 – PRESSURE DISTRIBUTION FOR A 11.8 PER CENT THICK SYMMETRICAL JOUKOWSKI AIRFOIL AT 6 DEGREES ANGLE OF ATTACK

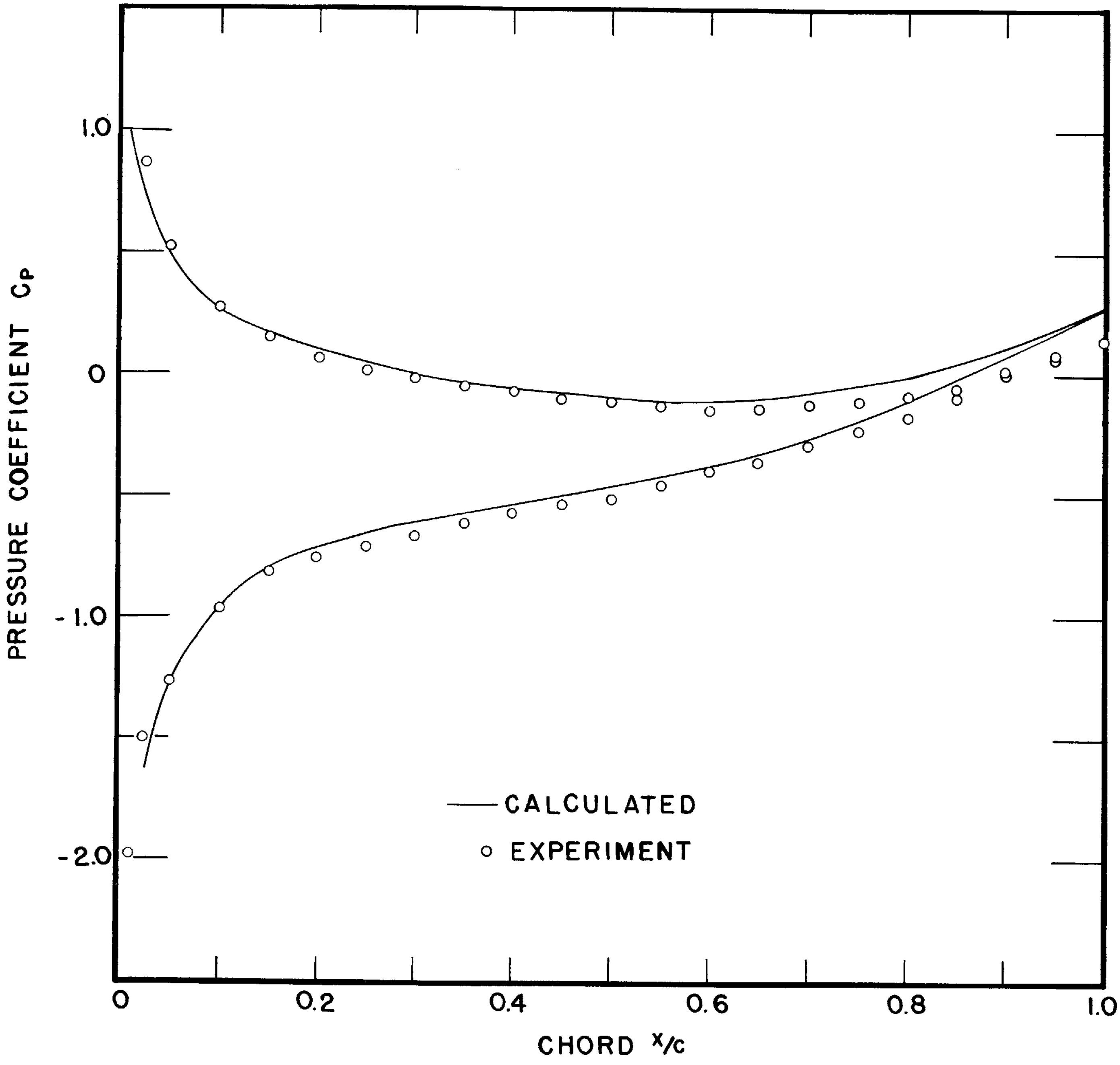

FIG. 9 - PRESSURE DISTRIBUTION FOR A 12/40 PIERCY AIRFOIL AT 6 DEGREES ANGLE OF ATTACK

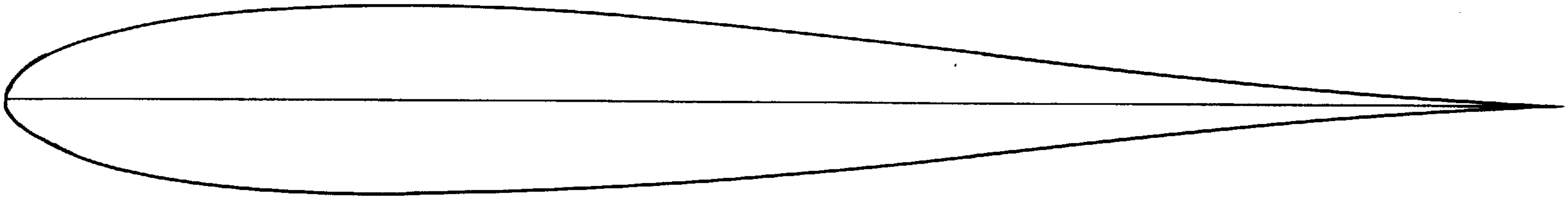

11.8 PER CENT THICK SYMMETRICAL JOUKOWSKI AIRFOIL

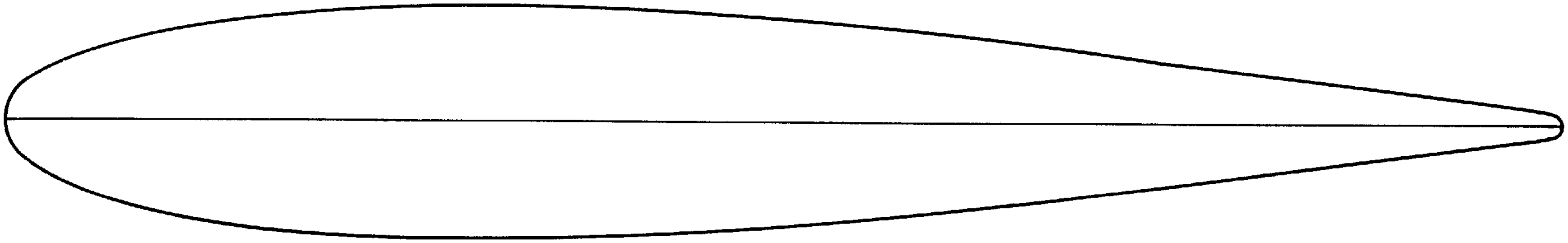

MODIFIED NACA 0015 AIRFOIL

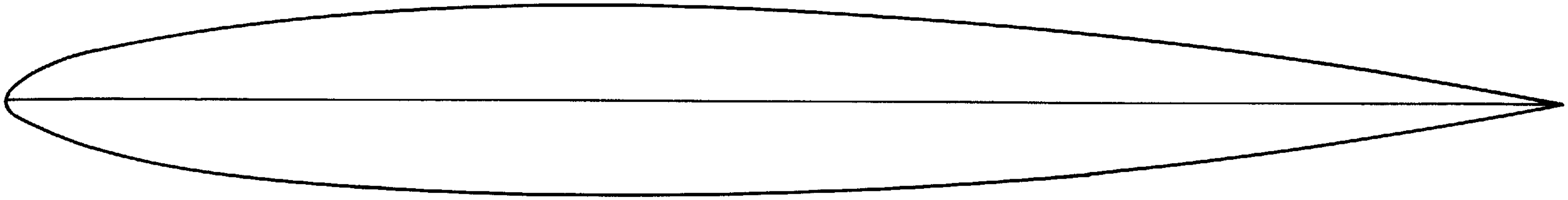

PIERCY 12/40 AIRFOIL

FIG. 10 – AIRFOIL SECTIONS

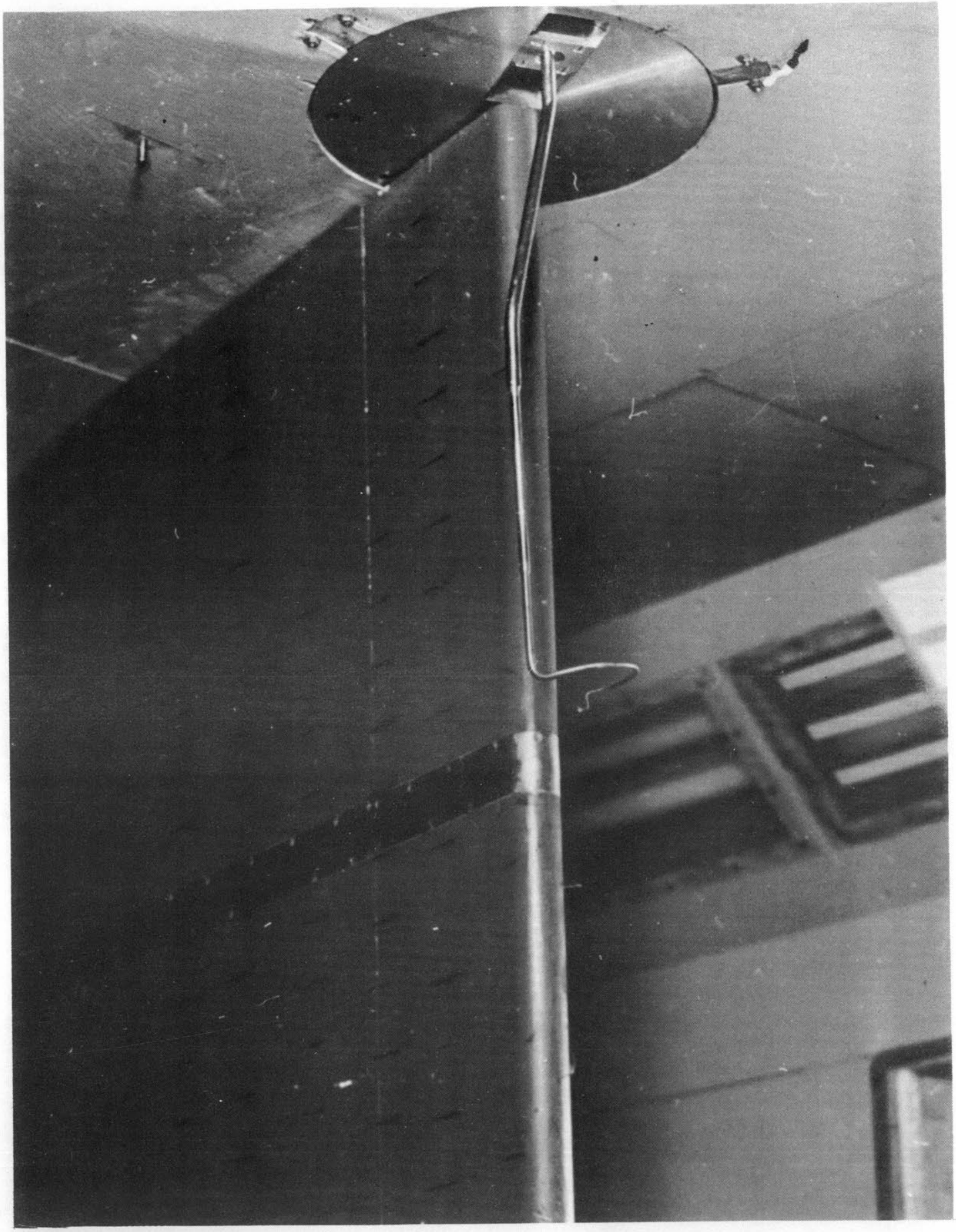

FIG. 11 – VIEW OF TEST REGION AND TOP WALL OF TUNNEL

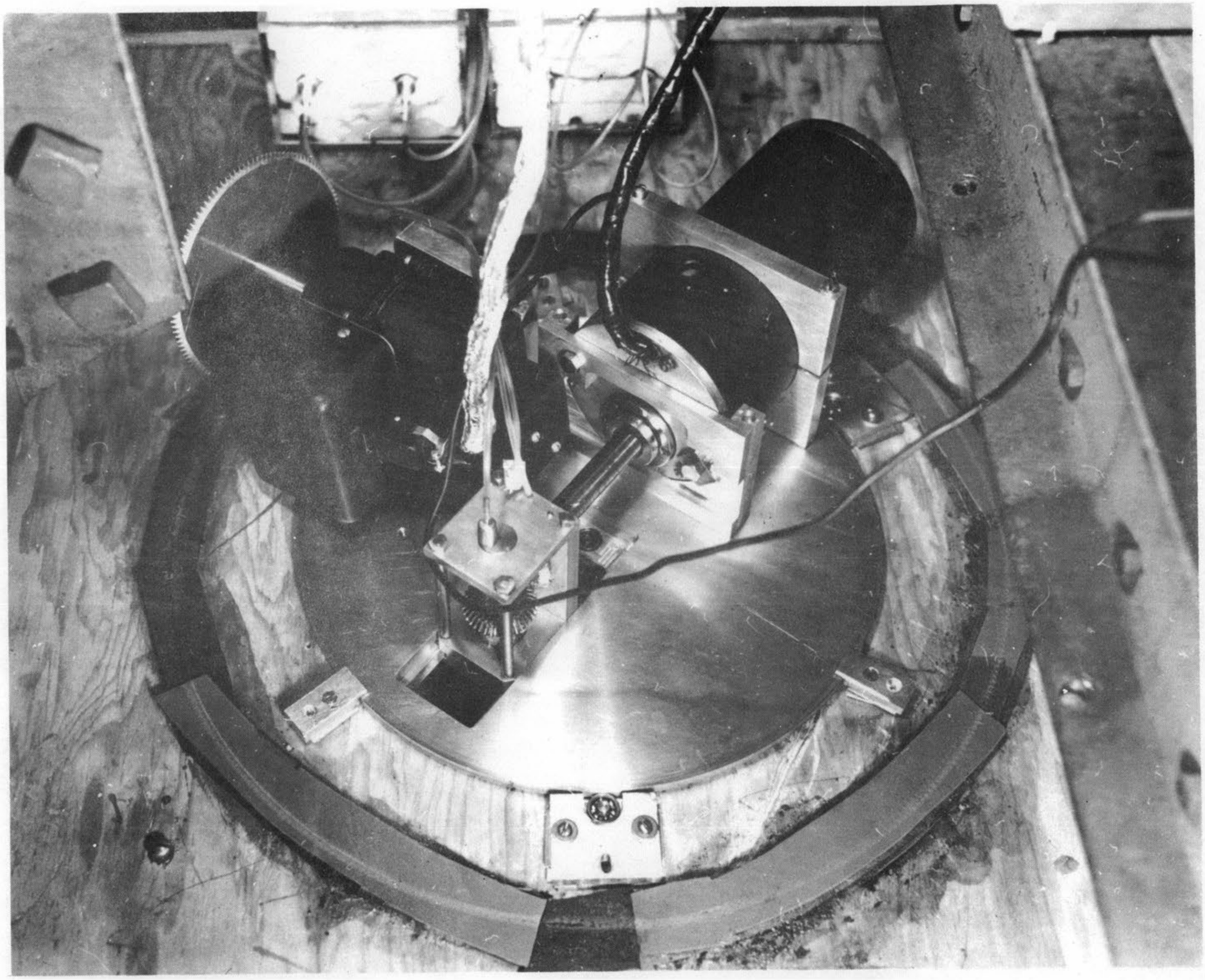

FIG. 12 – TRAVERSING MECHANISM

FIG. 13 — GENERAL VIEW OF TUNNEL TEST SECTION

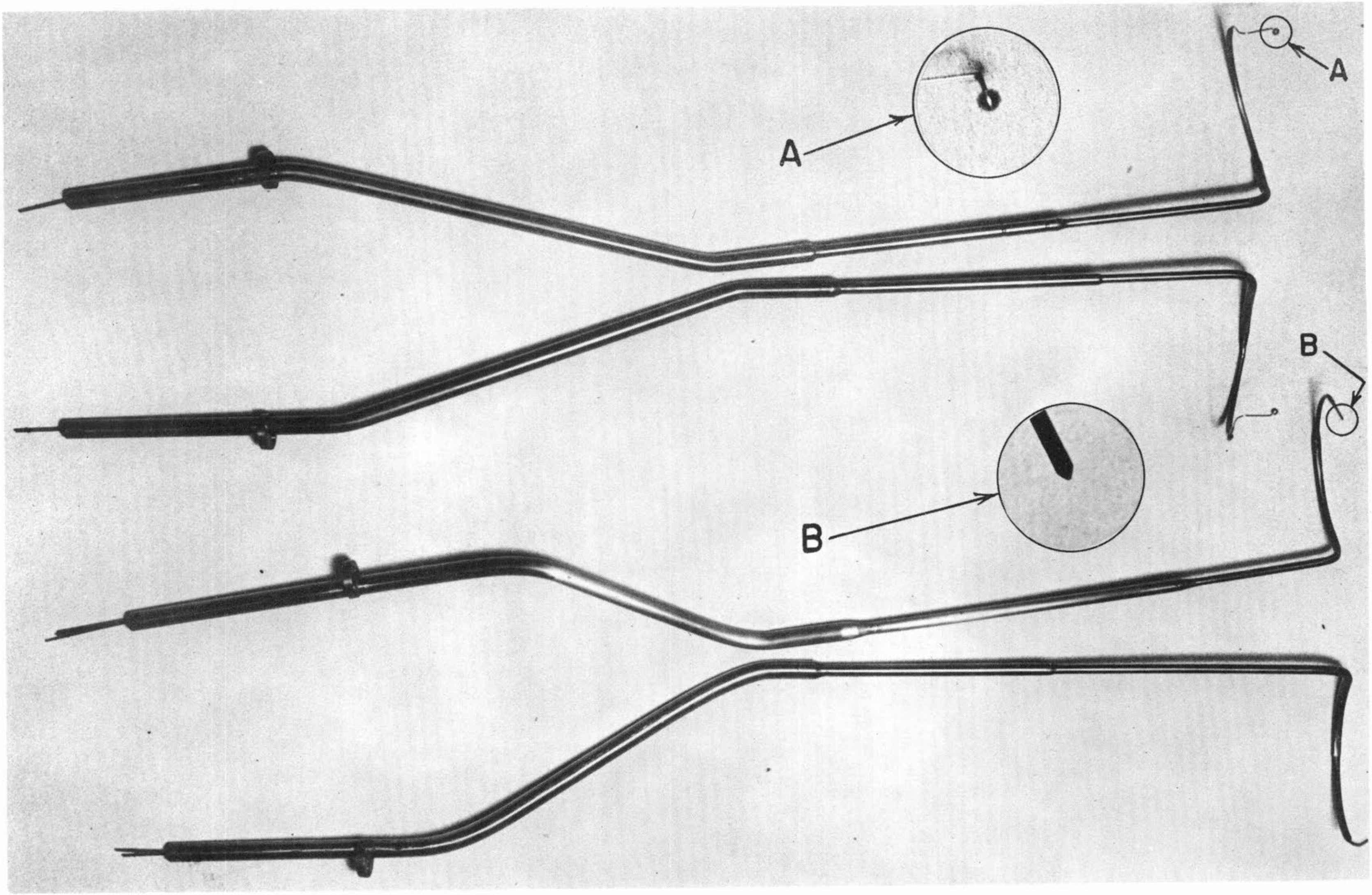

FIG. 14 – MEASURING PROBES

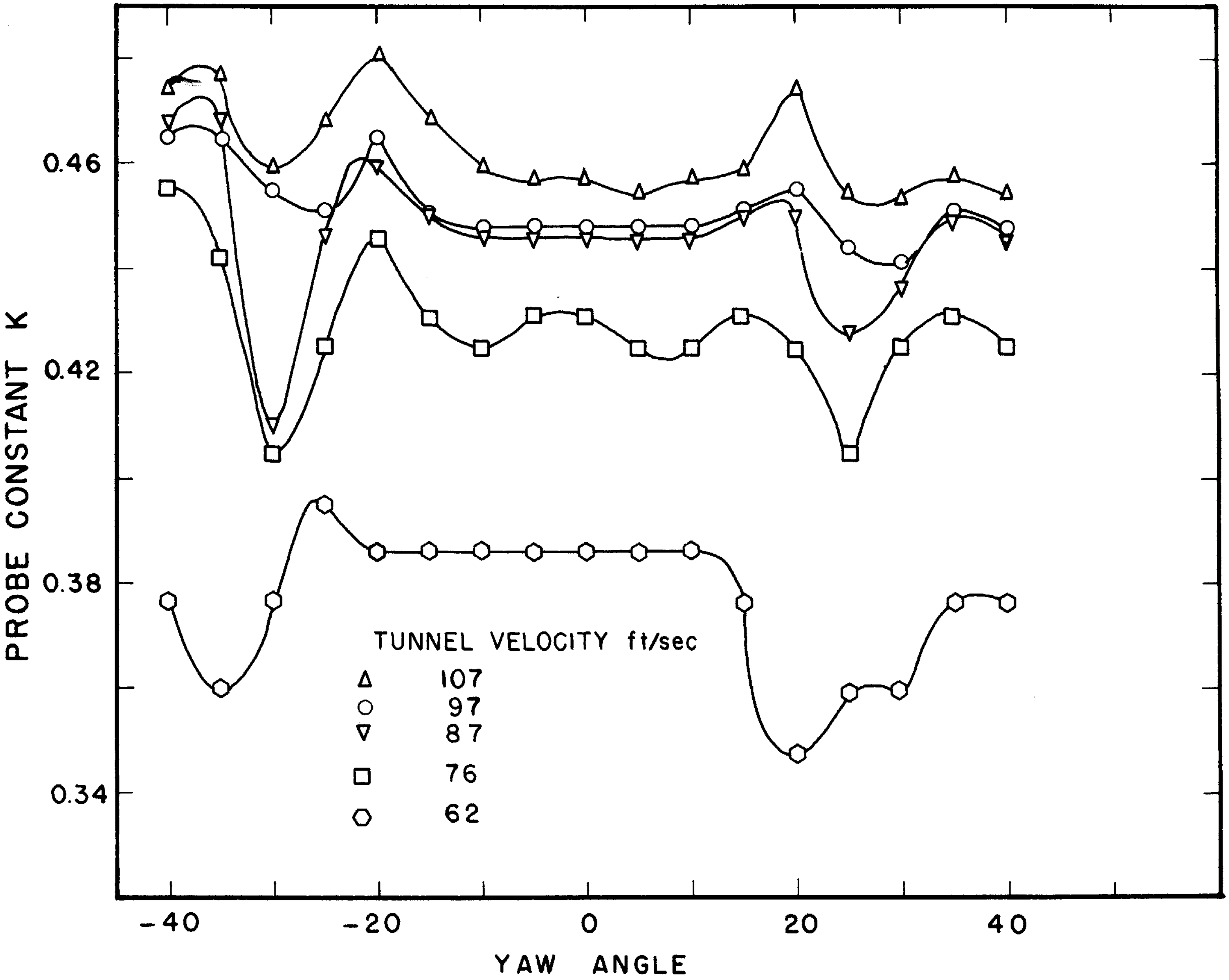

FIG. 15 – CALIBRATION CURVE FOR SPHERE STATIC PROBE

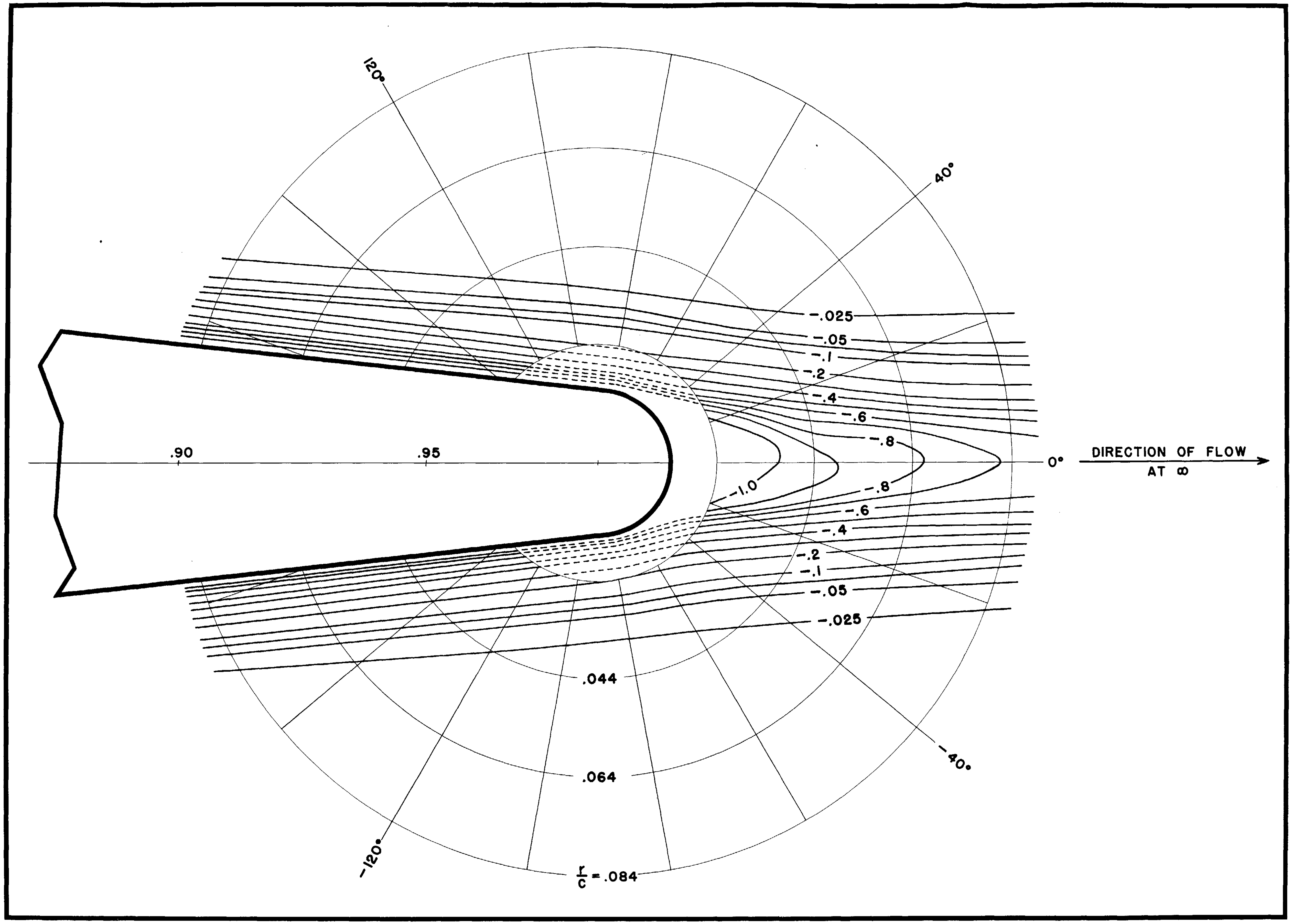

FIG. 16 - CONTOUR PLOT OF THE FLOW AROUND THE TRAILING EDGE OF THE AIRFOIL AT 0 DEGREE ANGLE OF ATTACK.
a - LINES OF CONSTANT STAGNATION PRESSURE.

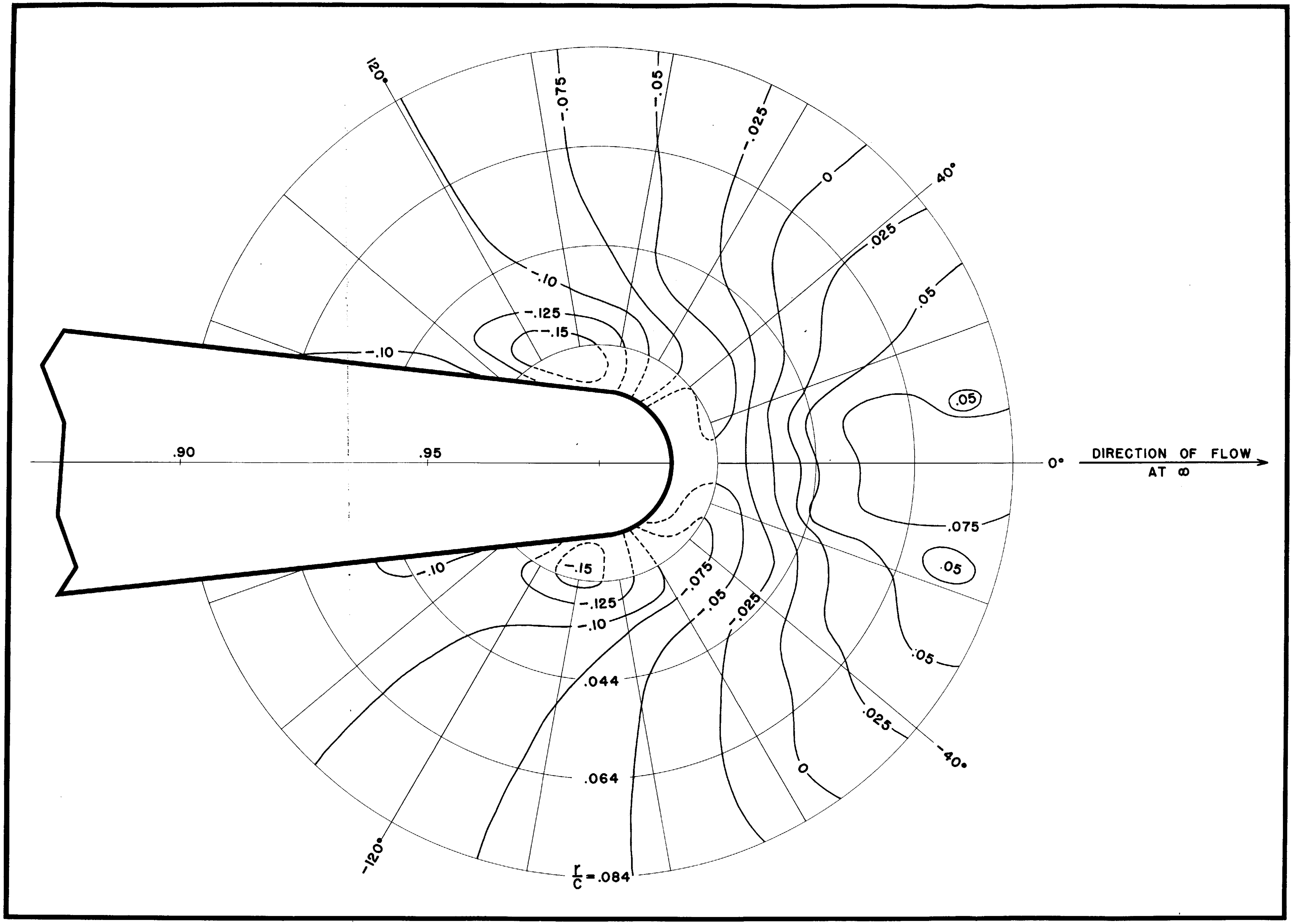

FIG. 16 - CONTINUED. b-LINES OF CONSTANT STATIC PRESSURE.

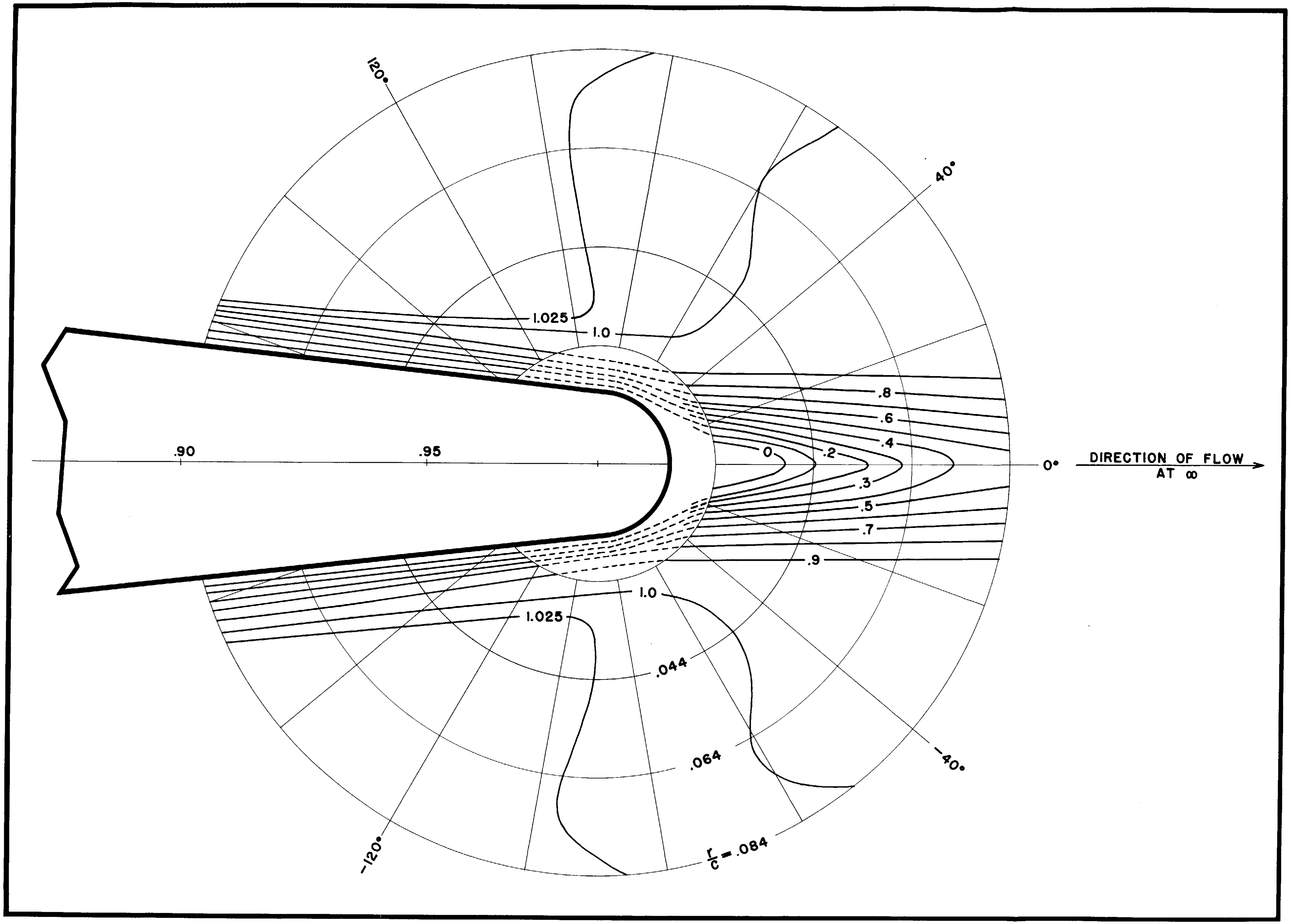

FIG. 16 – CONTINUED. c – LINES OF CONSTANT VELOCITY.

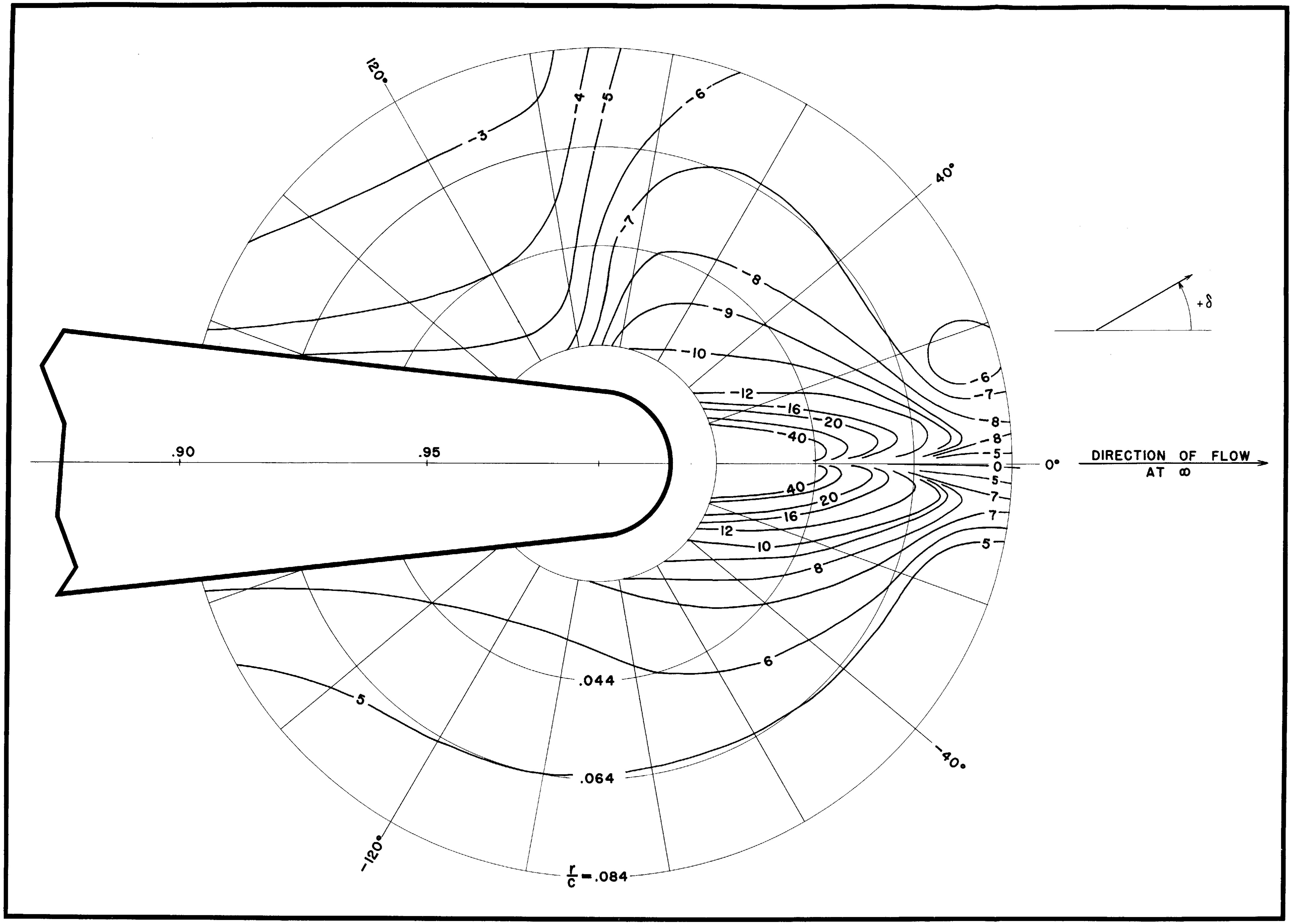

FIG. 16 — CONTINUED. d–LINES OF CONSTANT FLOW ANGLE–DEGREES.

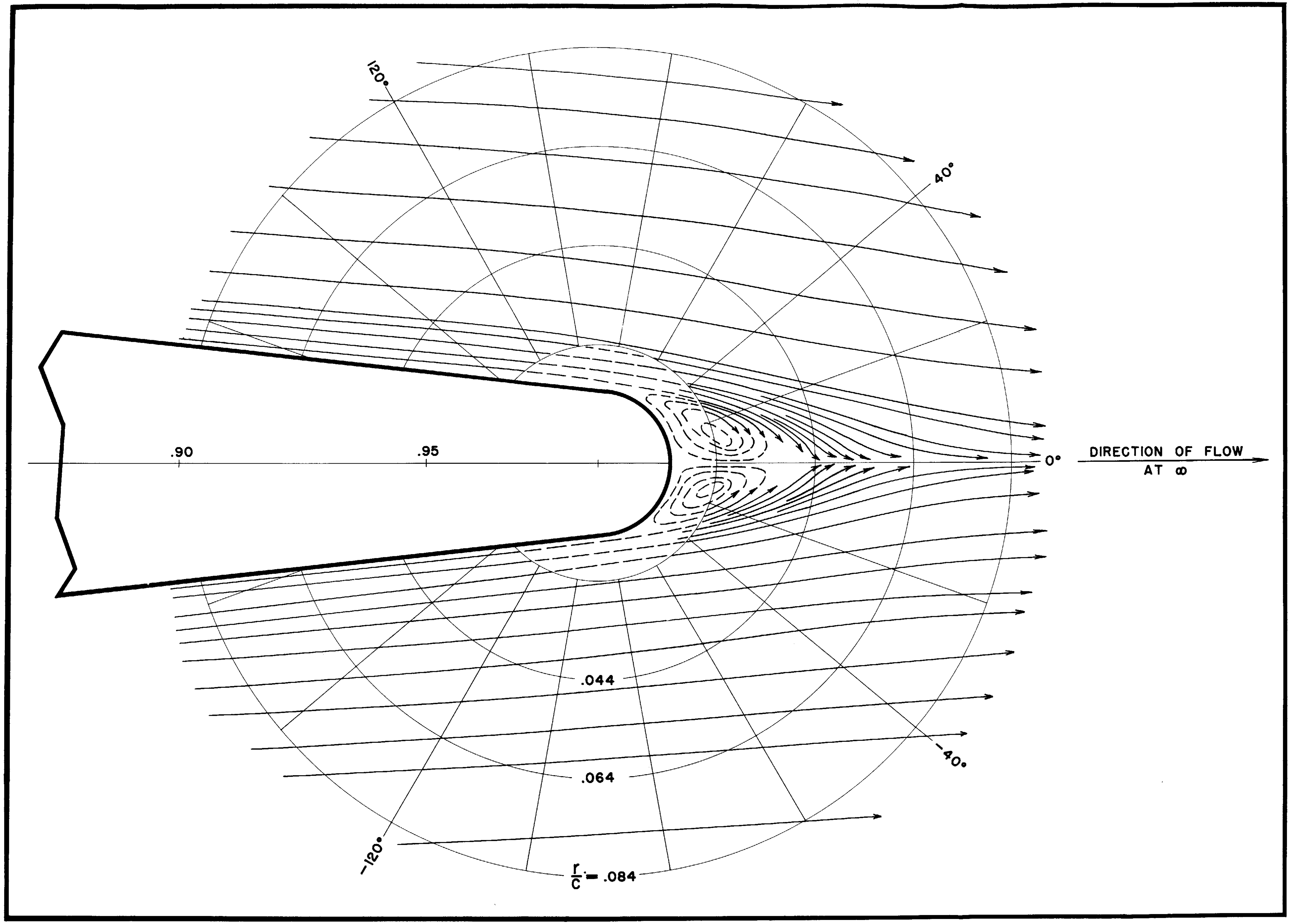

FIG. 16 – CONTINUED. e – STREAMLINES.

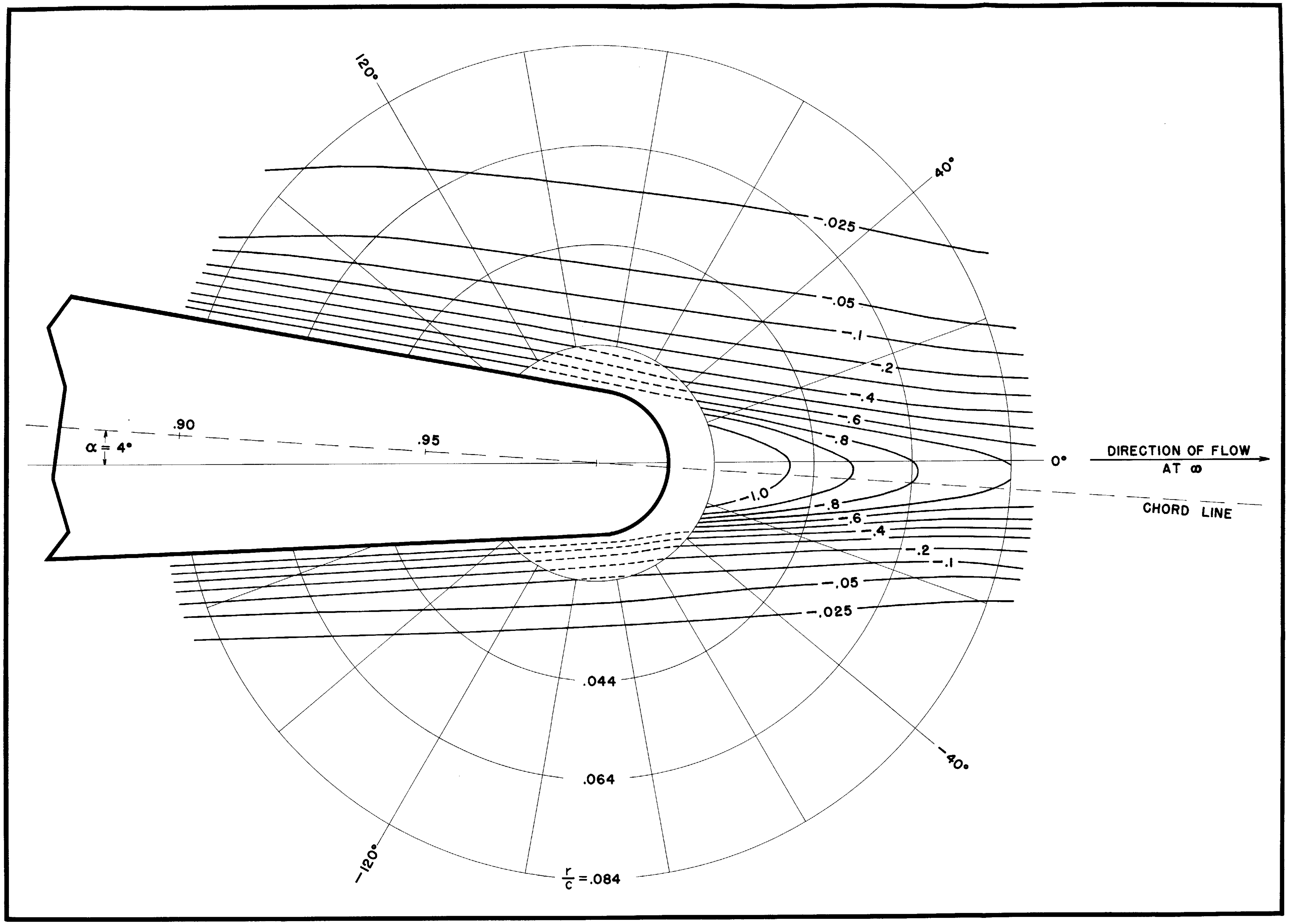

FIG. 17 - CONTOUR PLOT OF THE FLOW AROUND THE TRAILING EDGE OF THE AIRFOIL AT 4 DEGREES ANGLE OF ATTACK.

a - LINES OF CONSTANT STAGNATION PRESSURE.

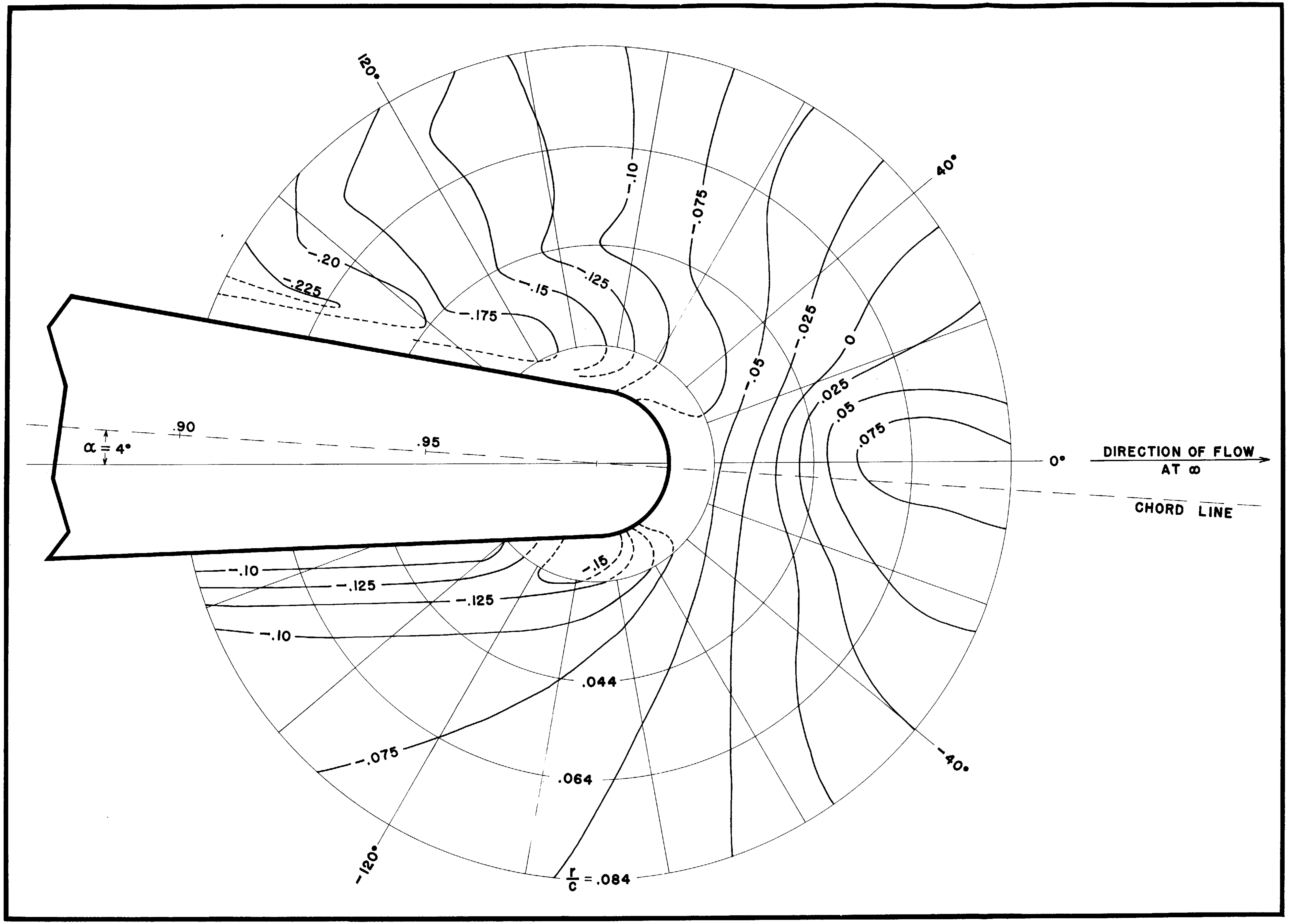

FIG. 17- CONTINUED. b- LINES OF CONSTANT STATIC PRESSURE.

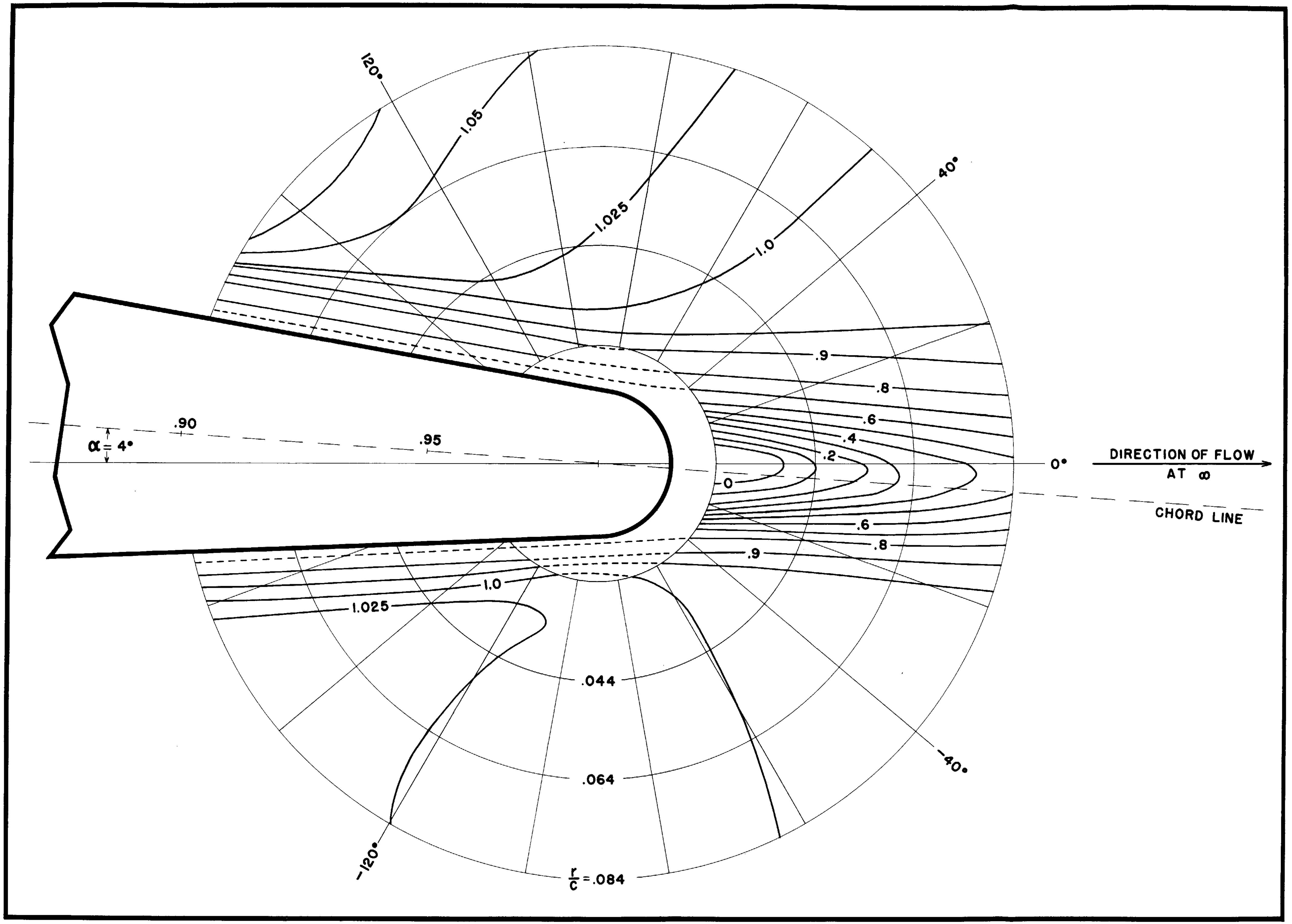

FIG. 17 - CONTINUED. c-LINES OF CONSTANT VELOCITY.

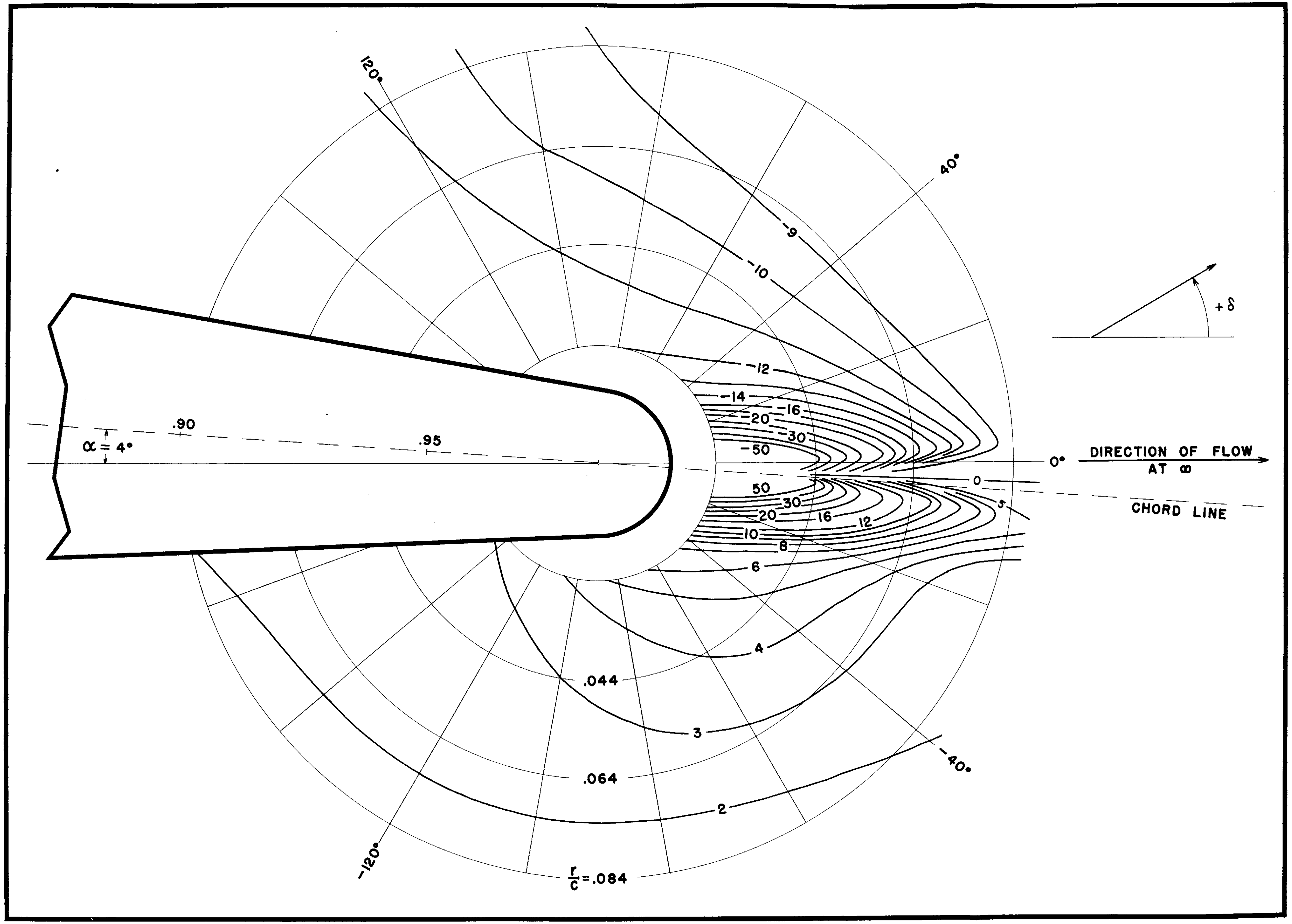

FIG. 17 - CONTINUED. d - LINES OF CONSTANT FLOW ANGLE - DEGREES.

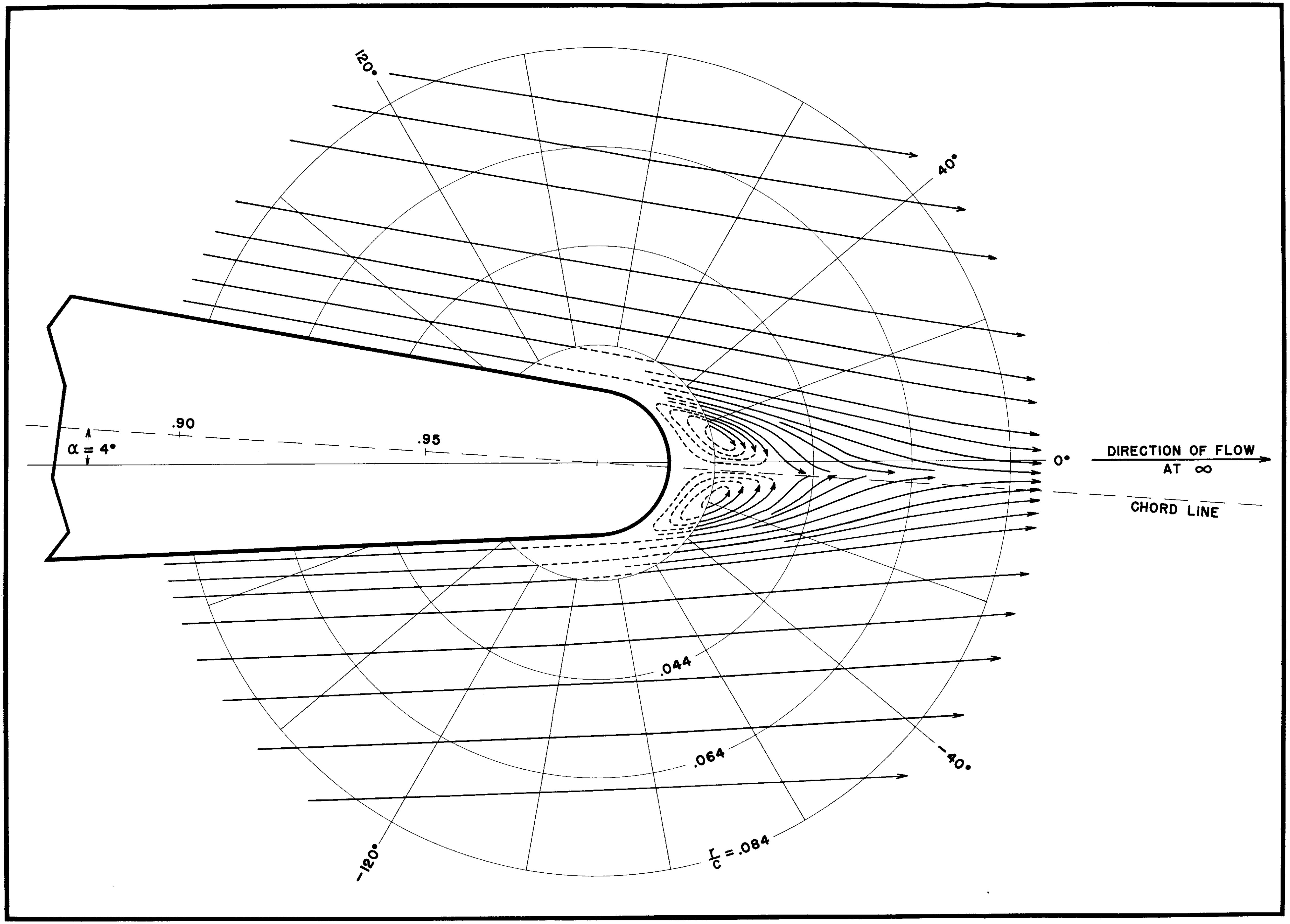

FIG. 17– CONTINUED. e– STREAMLINES.

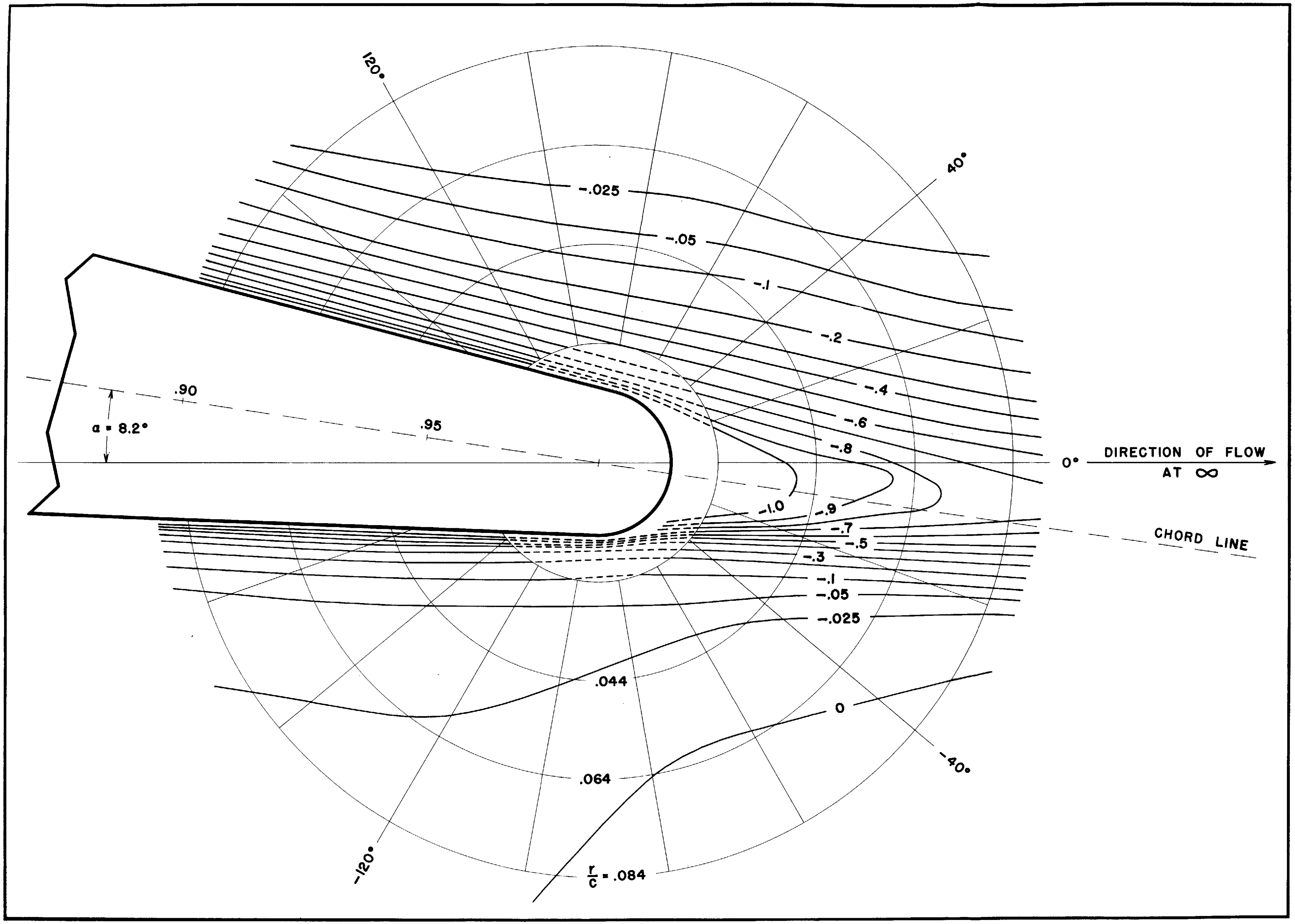

FIG. 18 – CONTOUR PLOT OF THE FLOW AROUND TRAILING EDGE OF THE AIRFOIL AT 8.2 DEGREES ANGLE OF ATTACK.

a – LINES OF CONSTANT STAGNATION PRESSURE.

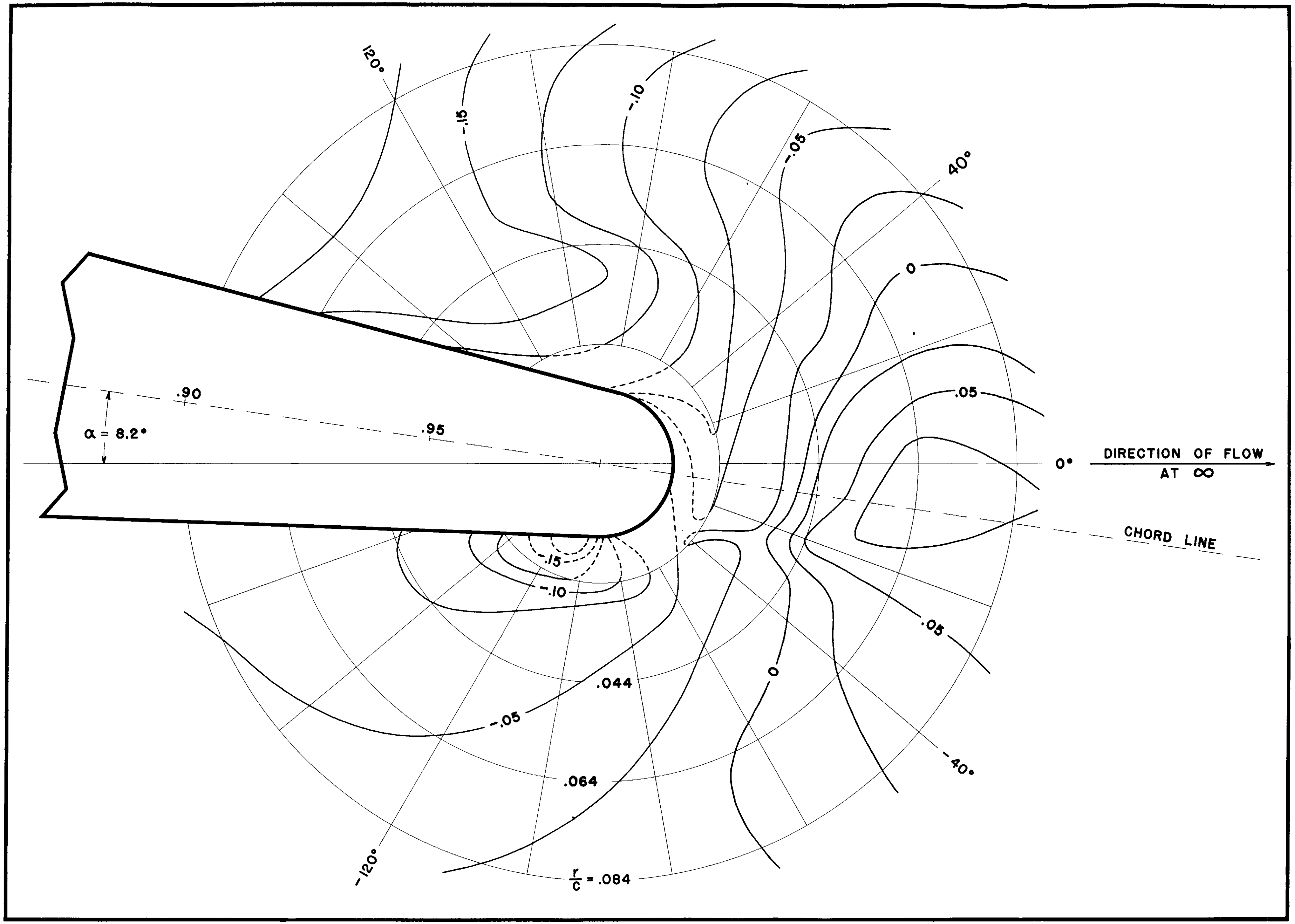

FIG. 18 - CONTINUED. b - LINES OF CONSTANT STATIC PRESSURE.

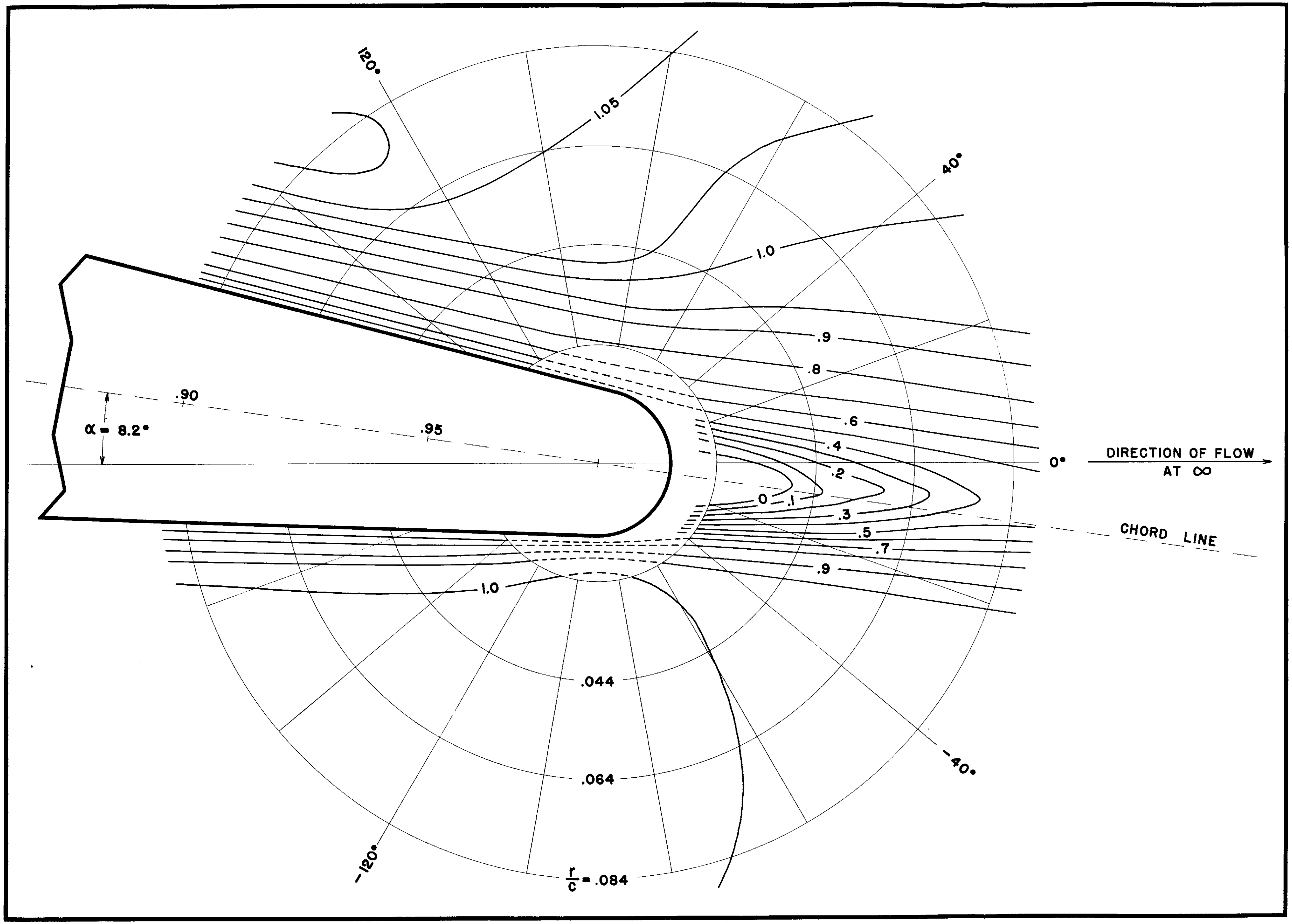

FIG. 18 - CONTINUED. c - LINES OF CONSTANT VELOCITY.

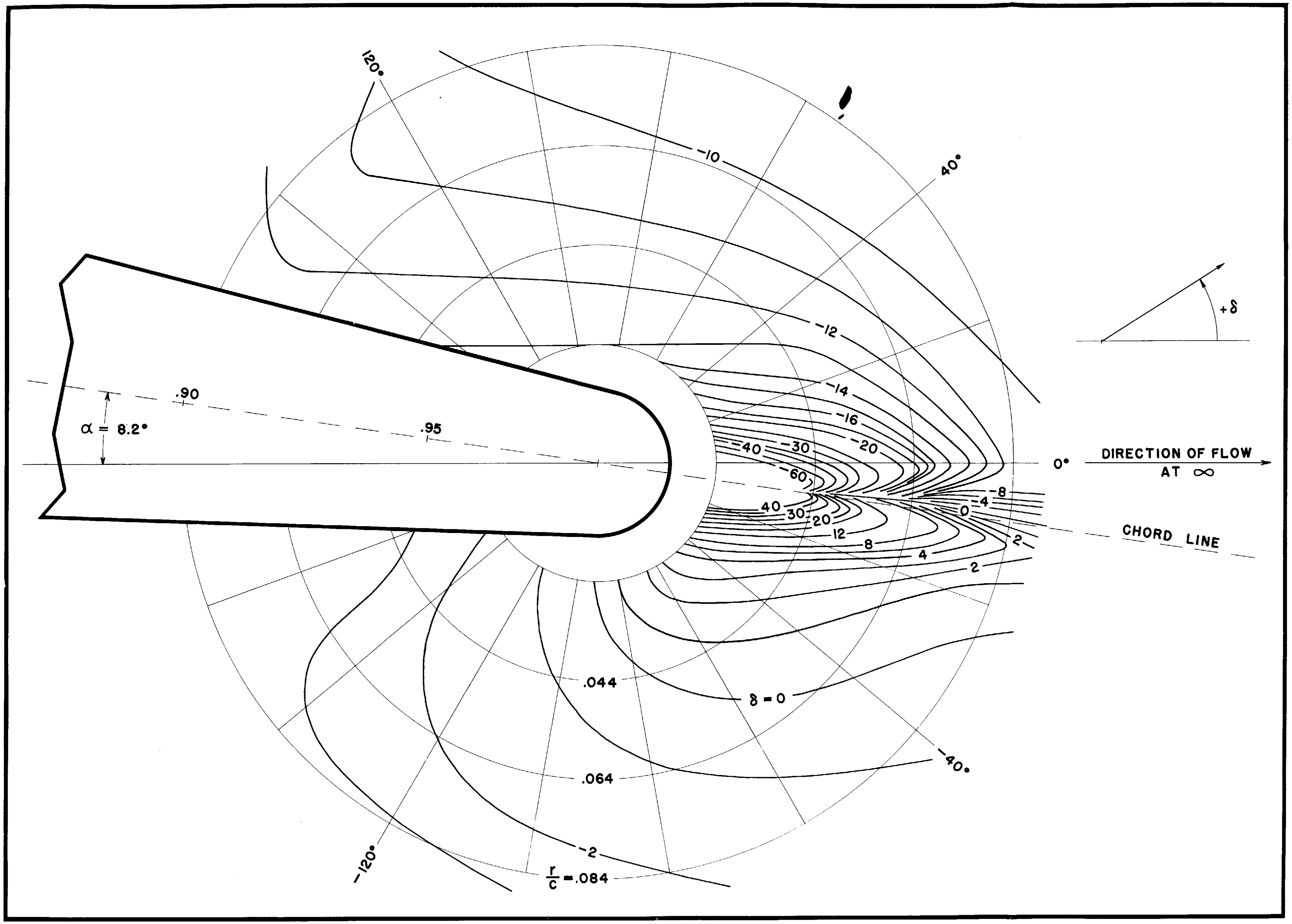

FIG. 18 - CONTINUED. d - LINES OF CONSTANT FLOW ANGLE - DEGREES.

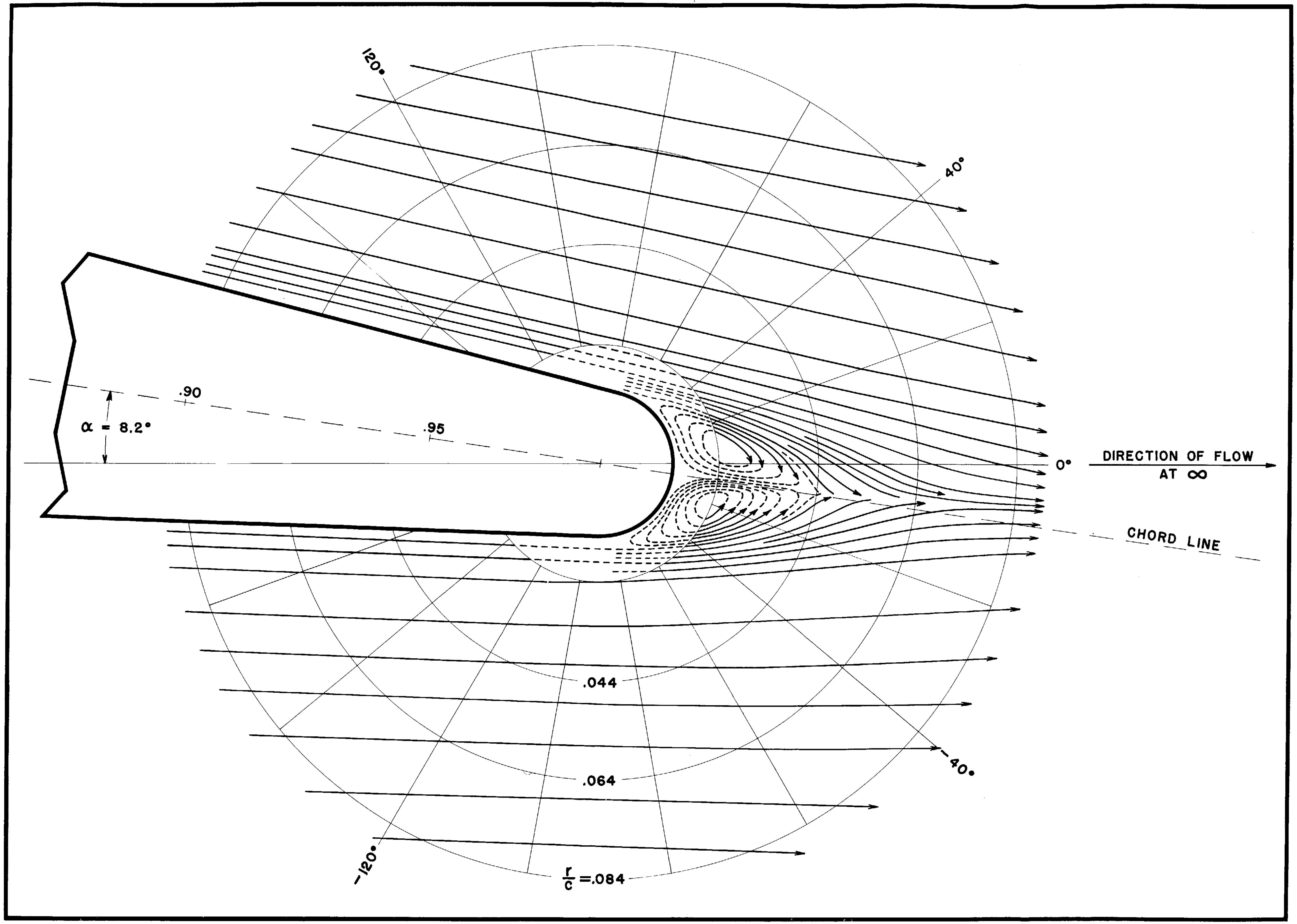

FIG. 18 — CONTINUED. e — STREAMLINES.

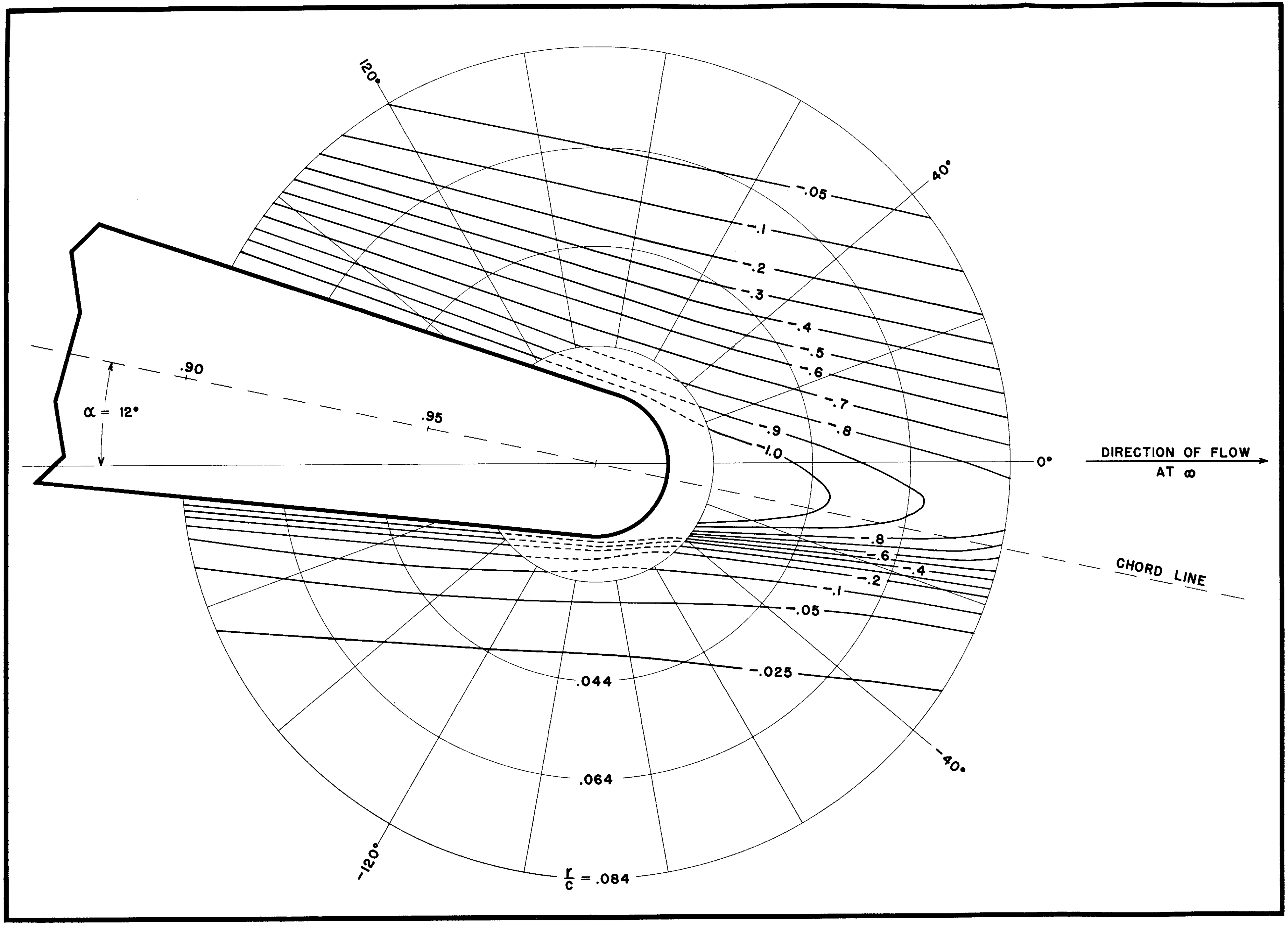

FIG. 19 - CONTOUR PLOT OF THE FLOW AROUND THE TRAILING EDGE OF THE AIRFOIL AT 12 DEGREES ANGLE OF ATTACK.
a - LINES OF CONSTANT STAGNATION PRESSURE.

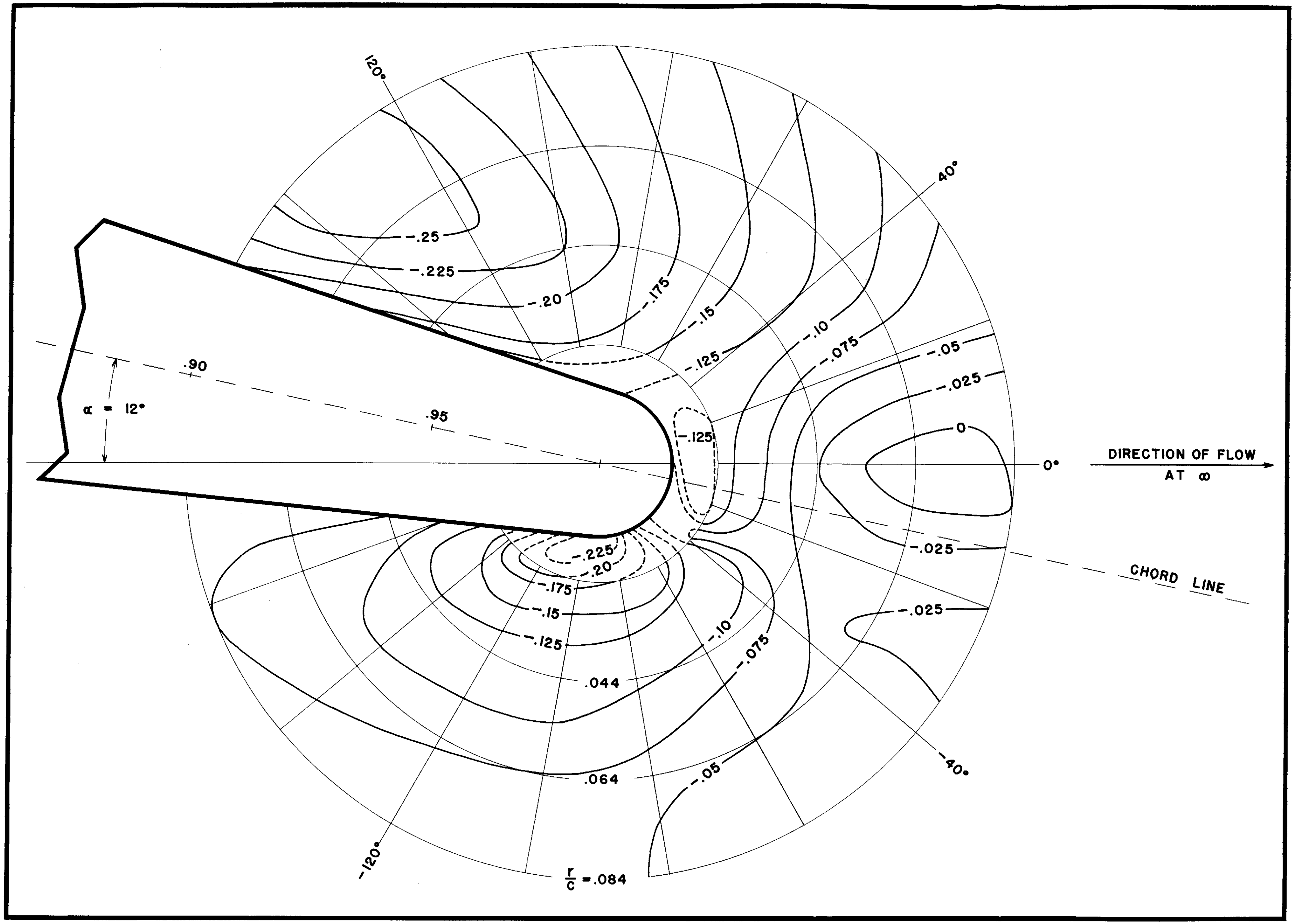

FIG. 19 - CONTINUED. b- LINES OF CONSTANT STATIC PRESSURE.

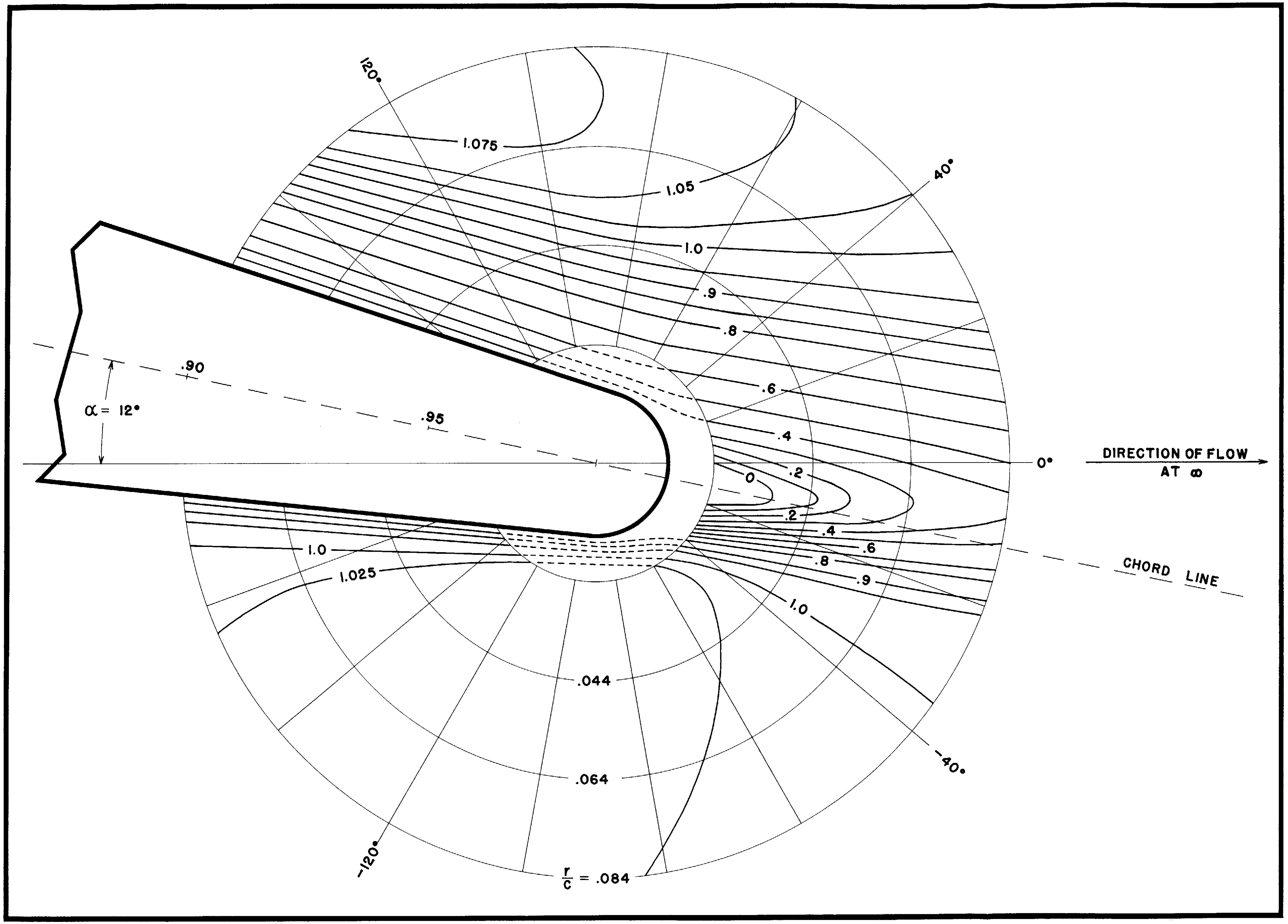

FIG. 19 — CONTINUED. c — LINES OF CONSTANT VELOCITY.

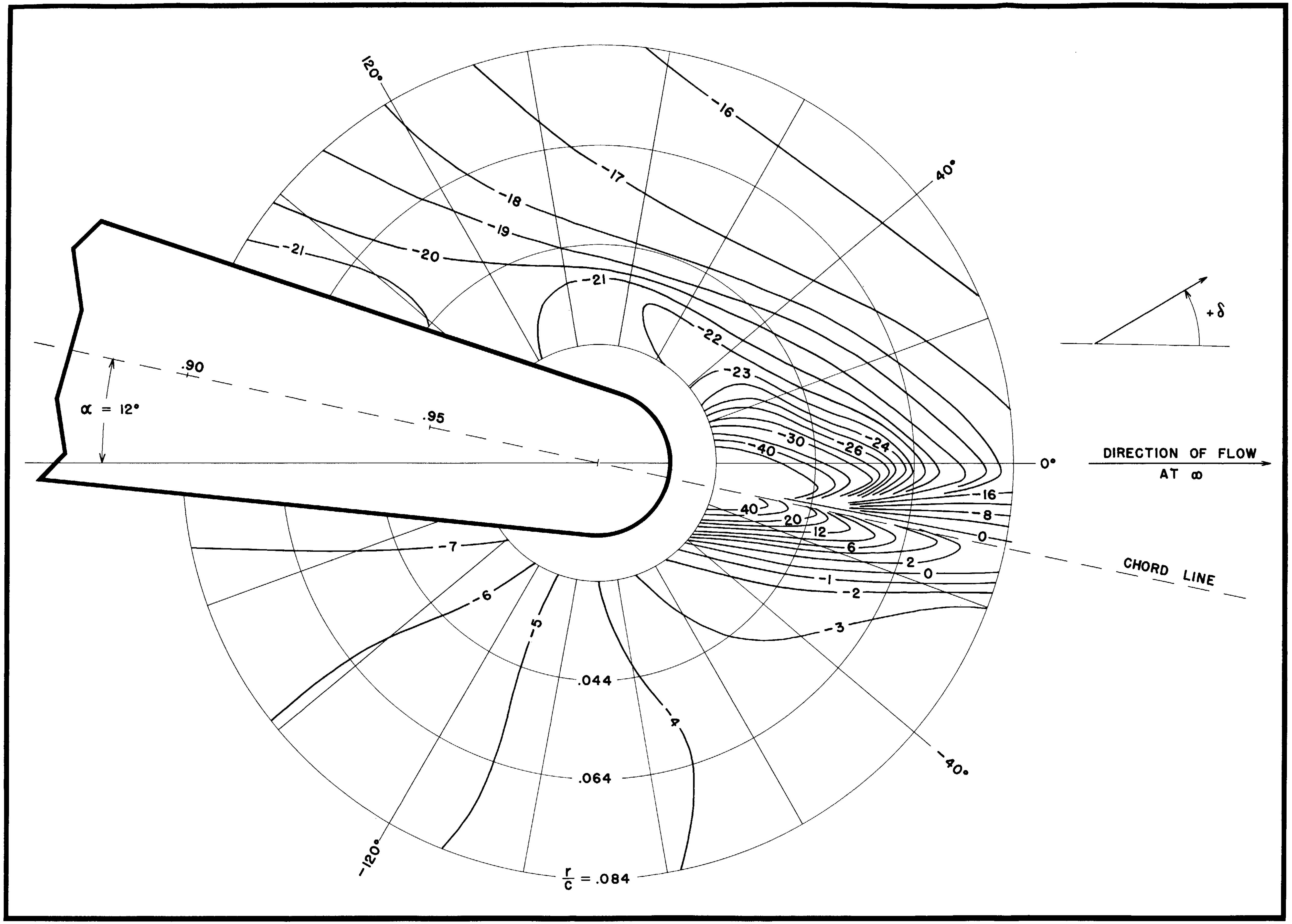

FIG. 19 - CONTINUED. d - LINES OF CONSTANT FLOW ANGLE-DEGREES.

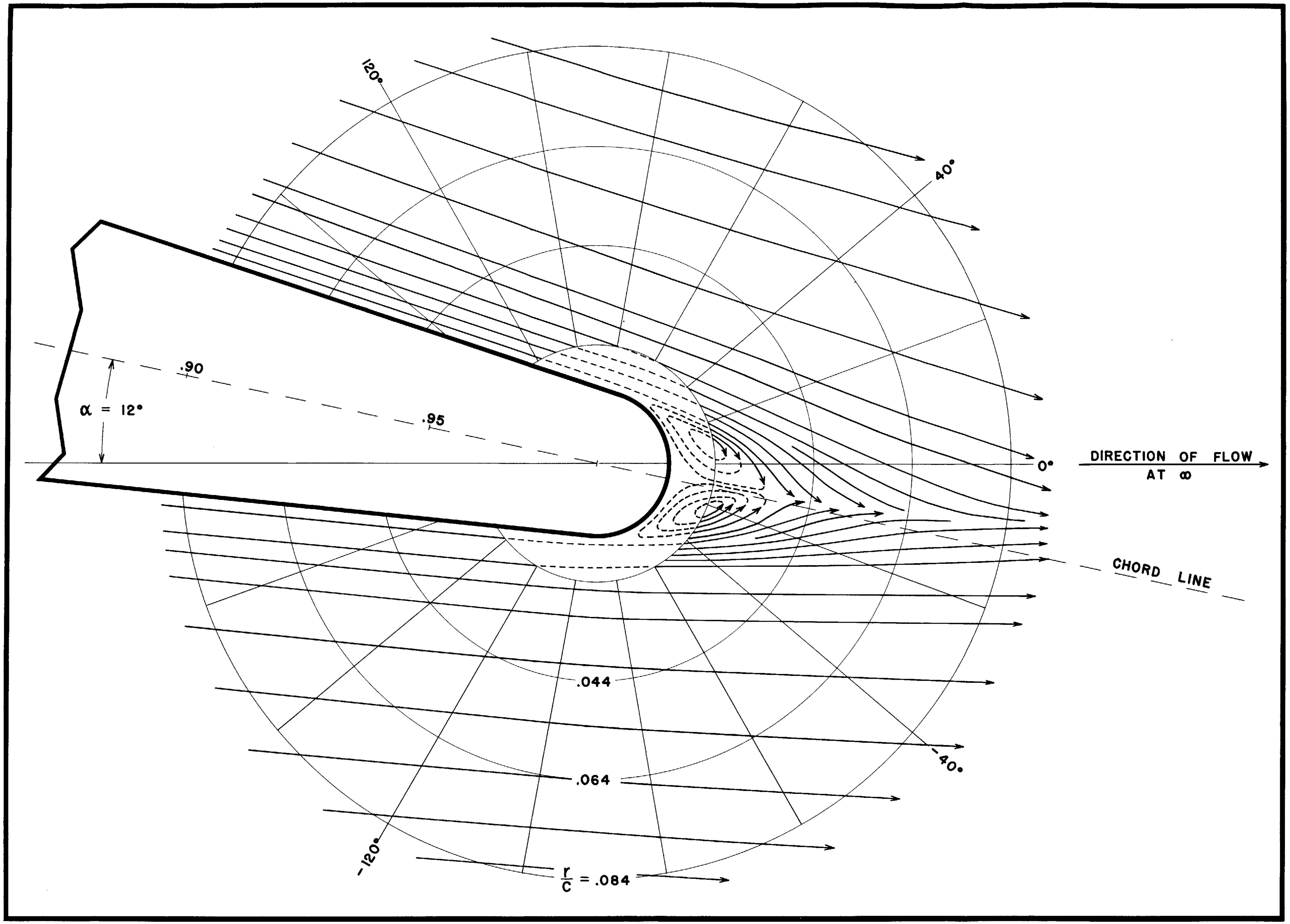

FIG. 19 - CONTINUED. e- STREAMLINES.

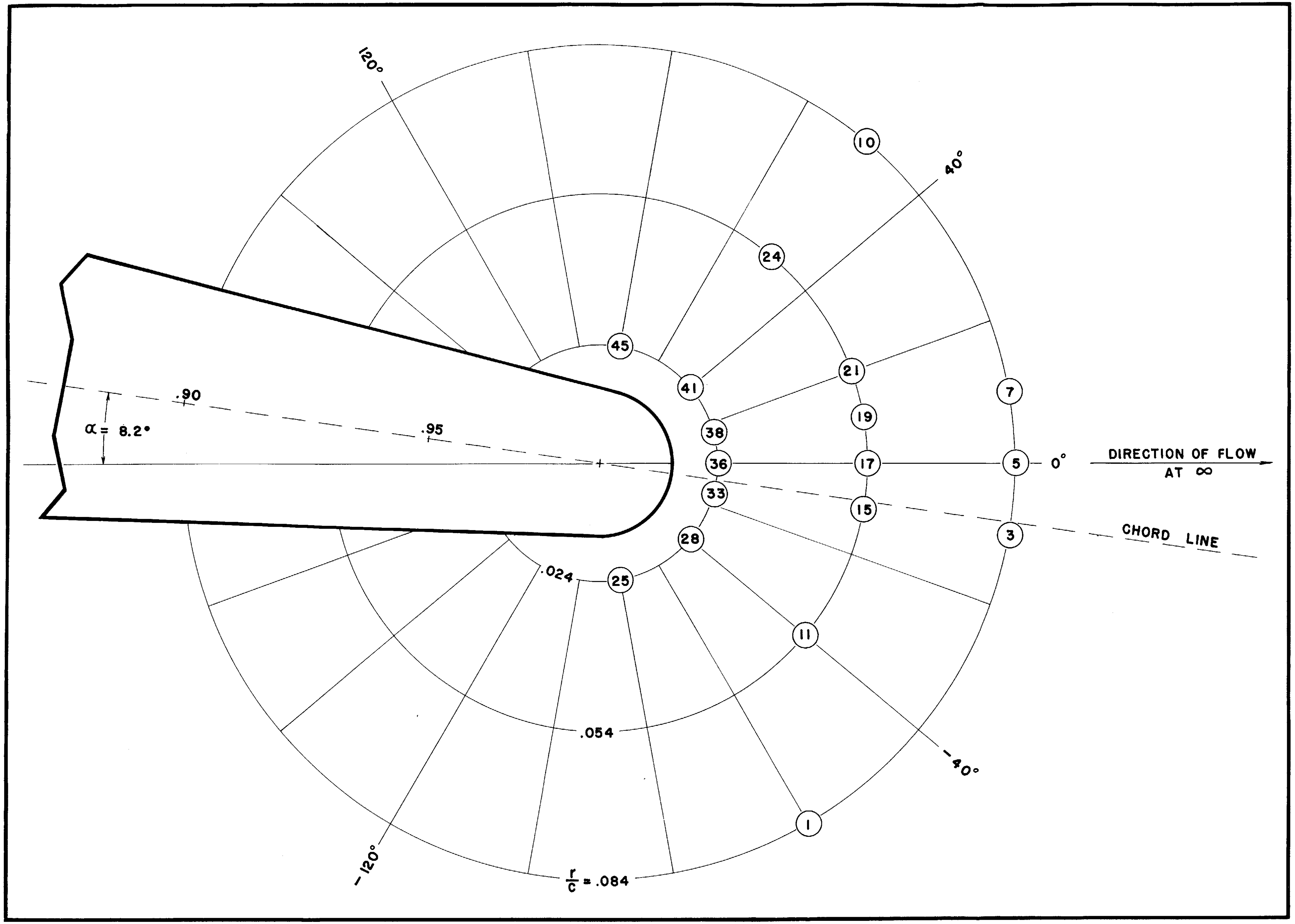

FIG. 20 — LOCATION OF HOT WIRE MEASUREMENTS

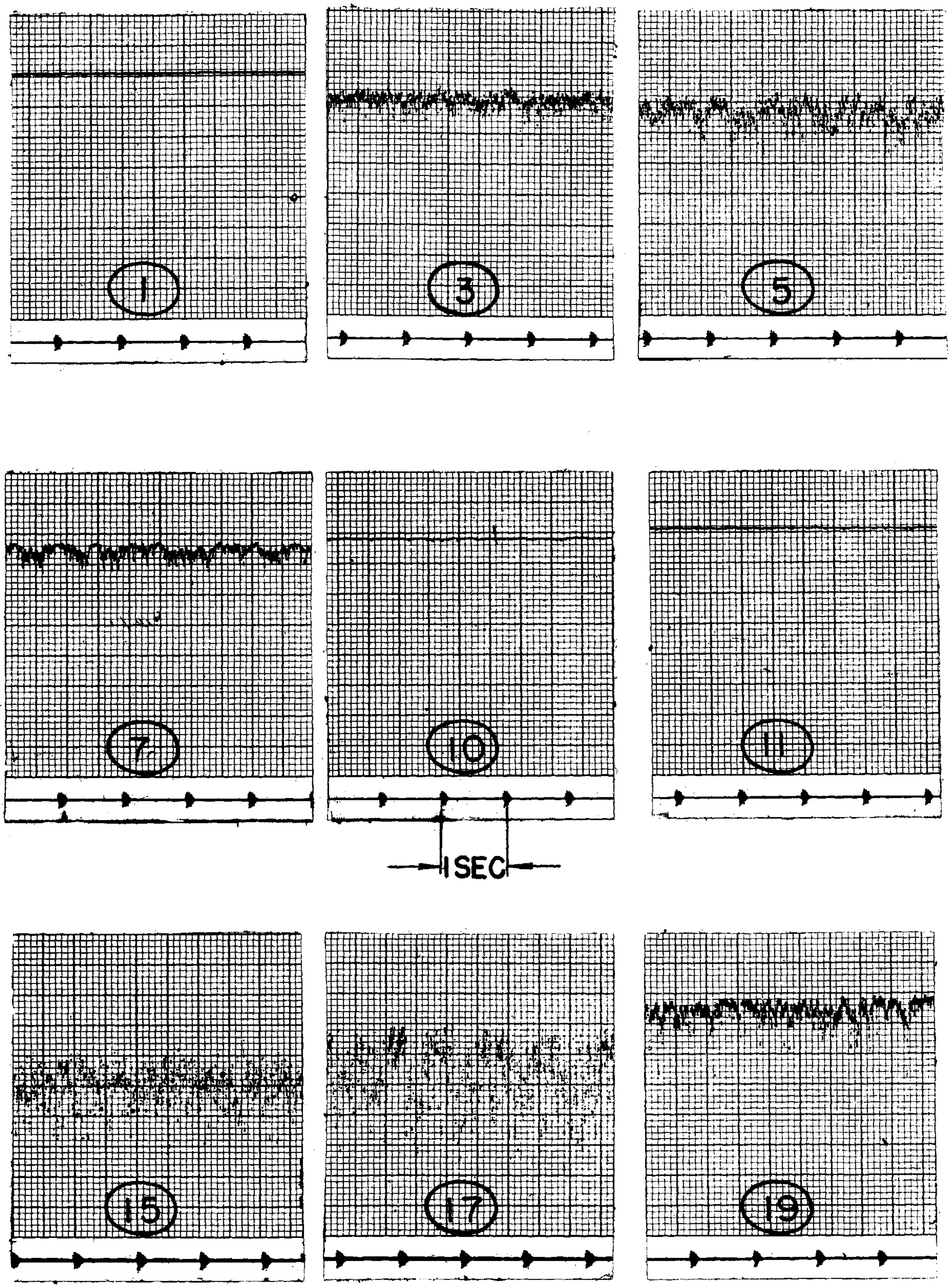

FIG. 21 - SANBORN RECORDINGS OF HOT WIRE MEASUREMENTS

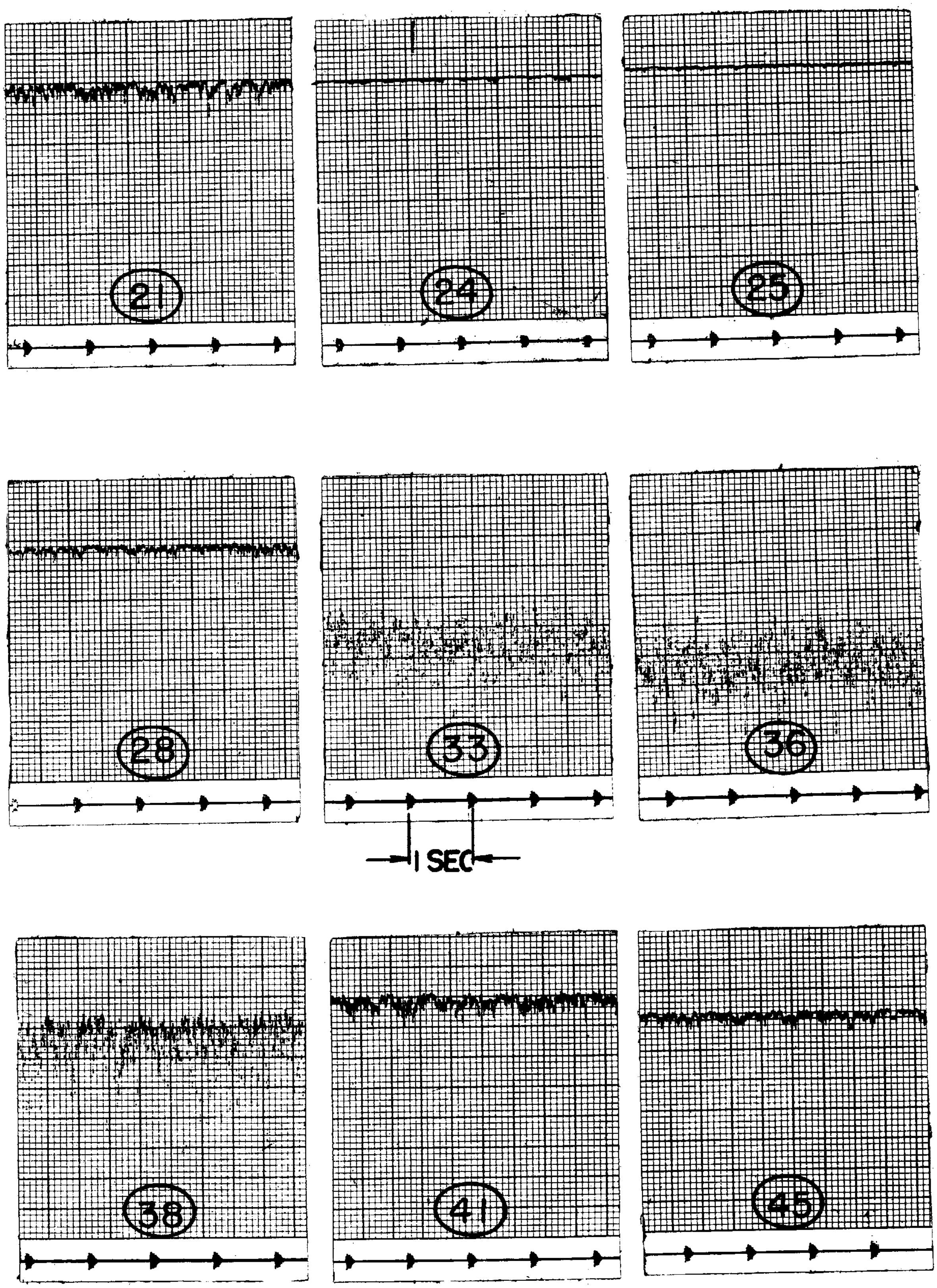

FIG. 21 - SANBORN RECORDINGS OF HOT WIRE MEASUREMENTS

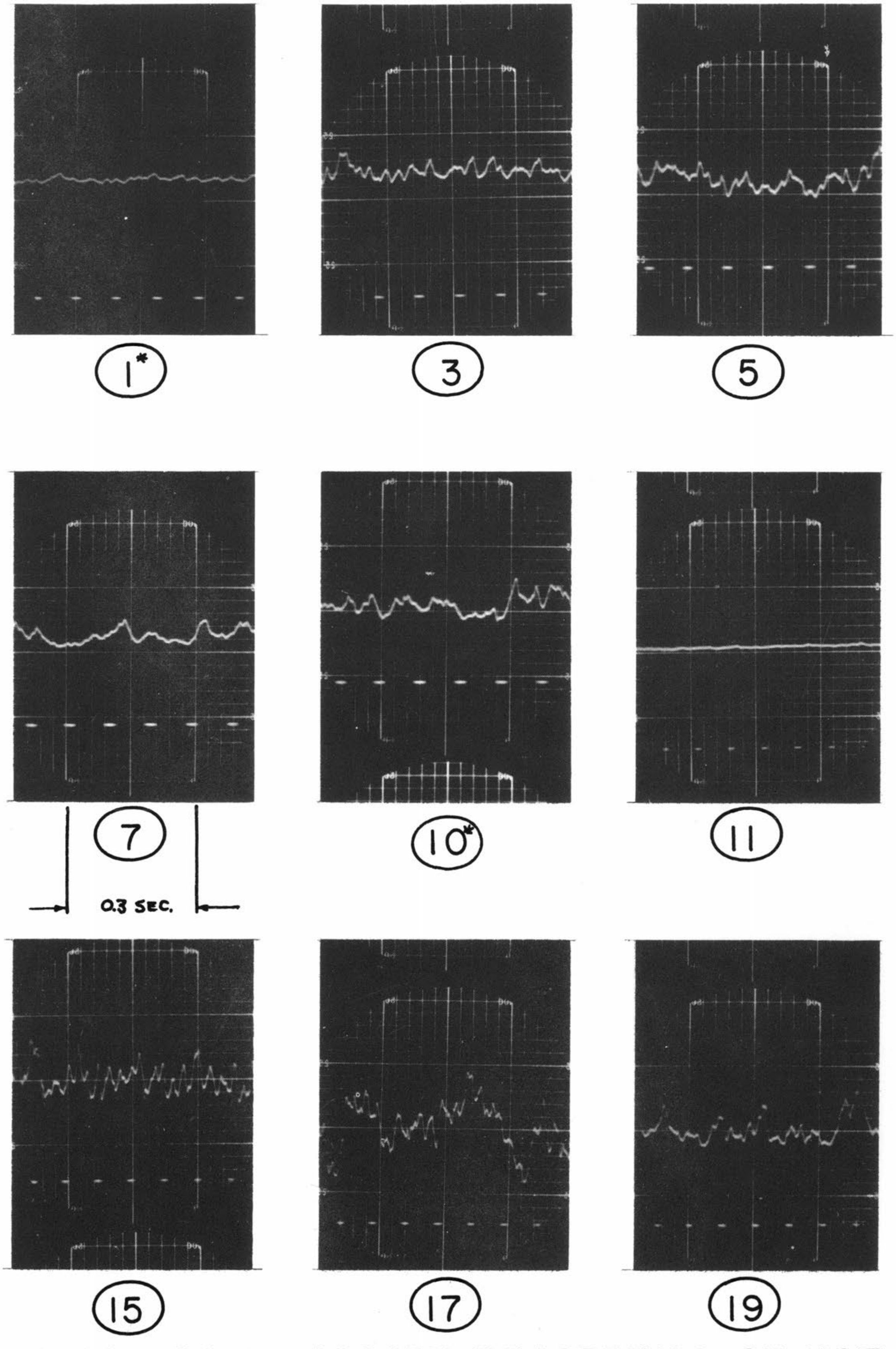

①* ③ ⑤ ⑦ ⑩* ⑪ ⑮ ⑰ ⑲

FIG. 22 - OSCILLOSCOPE RECORDINGS OF HOT WIRE MEASUREMENTS

*AMPLITUDE MAGNIFIED 10 TIMES

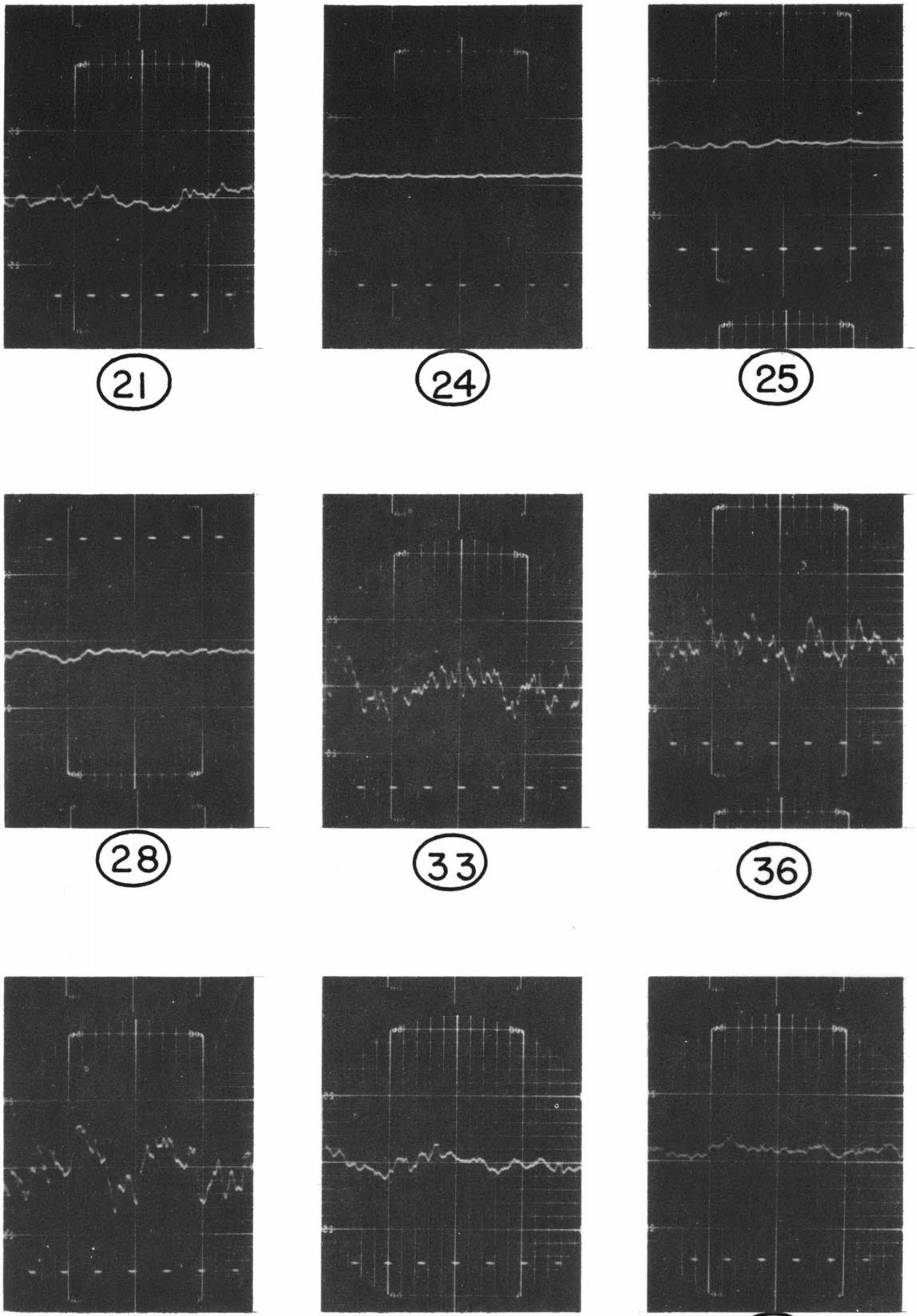

㉑ ㉔ ㉕

㉘ ㉝ ㊱

㊳ ㊶ ㊺

FIG. 22- CONTINUED

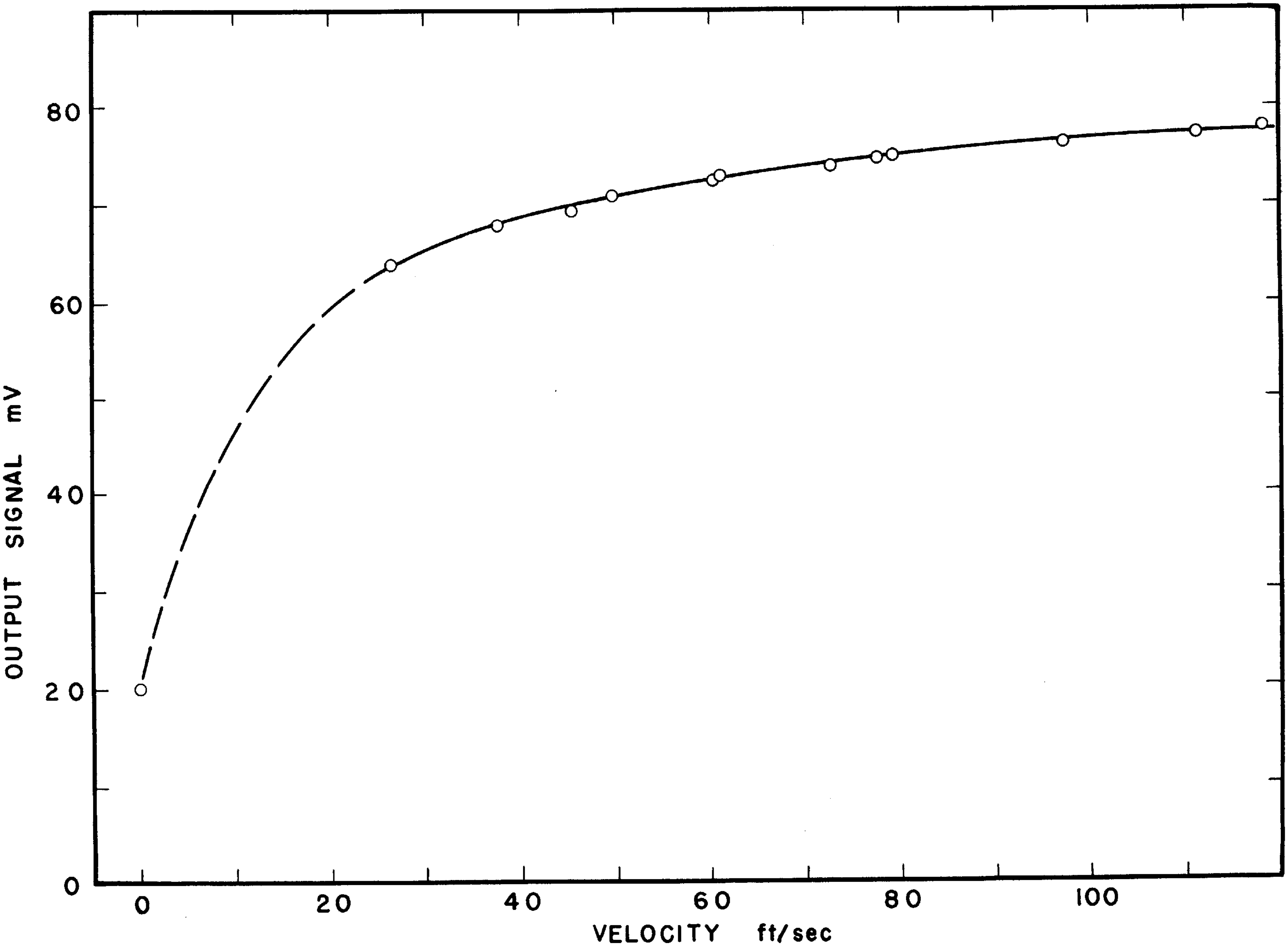

FIG. 23 – CALIBRATION CURVE FOR THE HOT WIRE

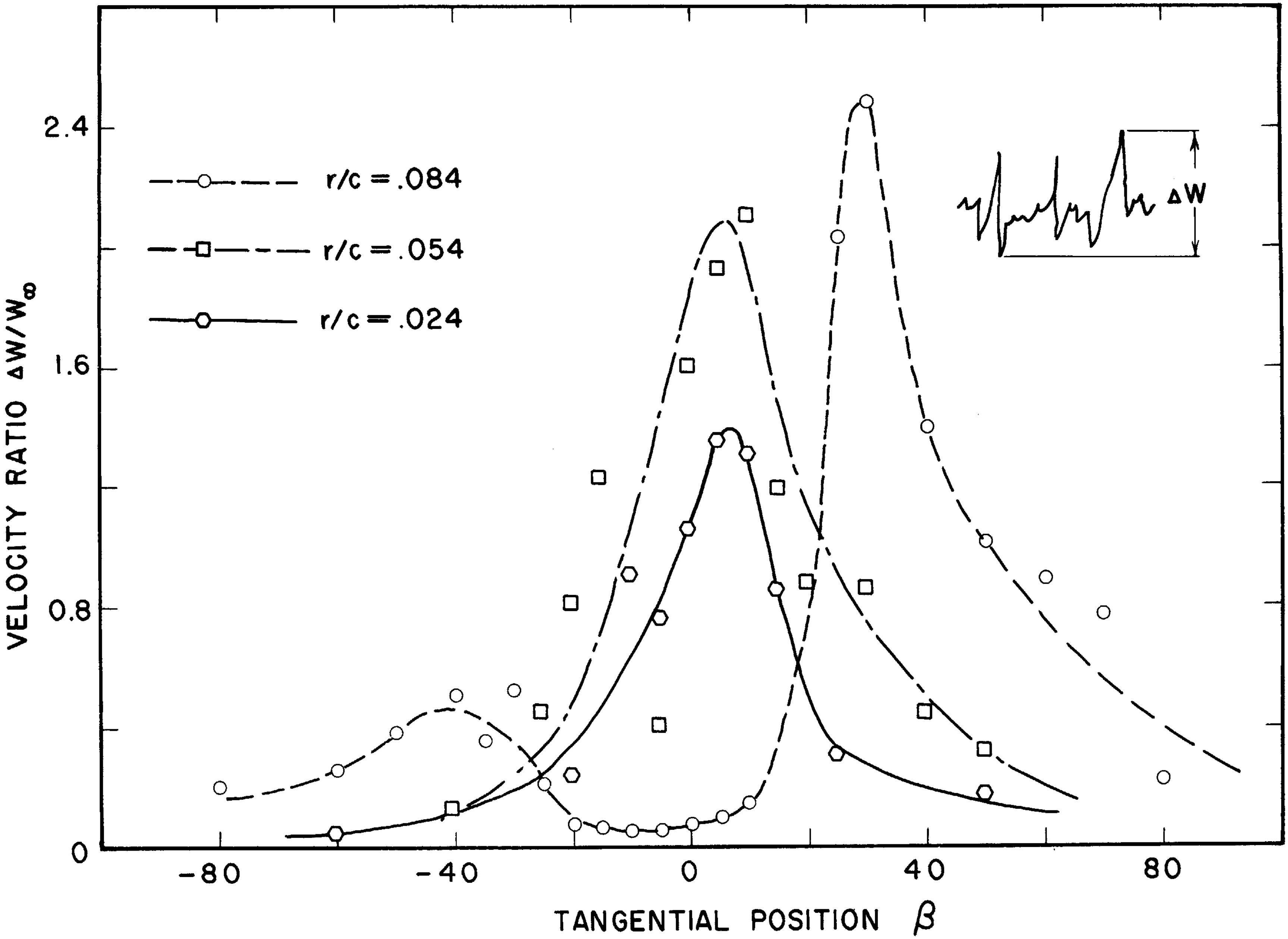

FIG. 24 – VELOCITY FLUCTUATIONS

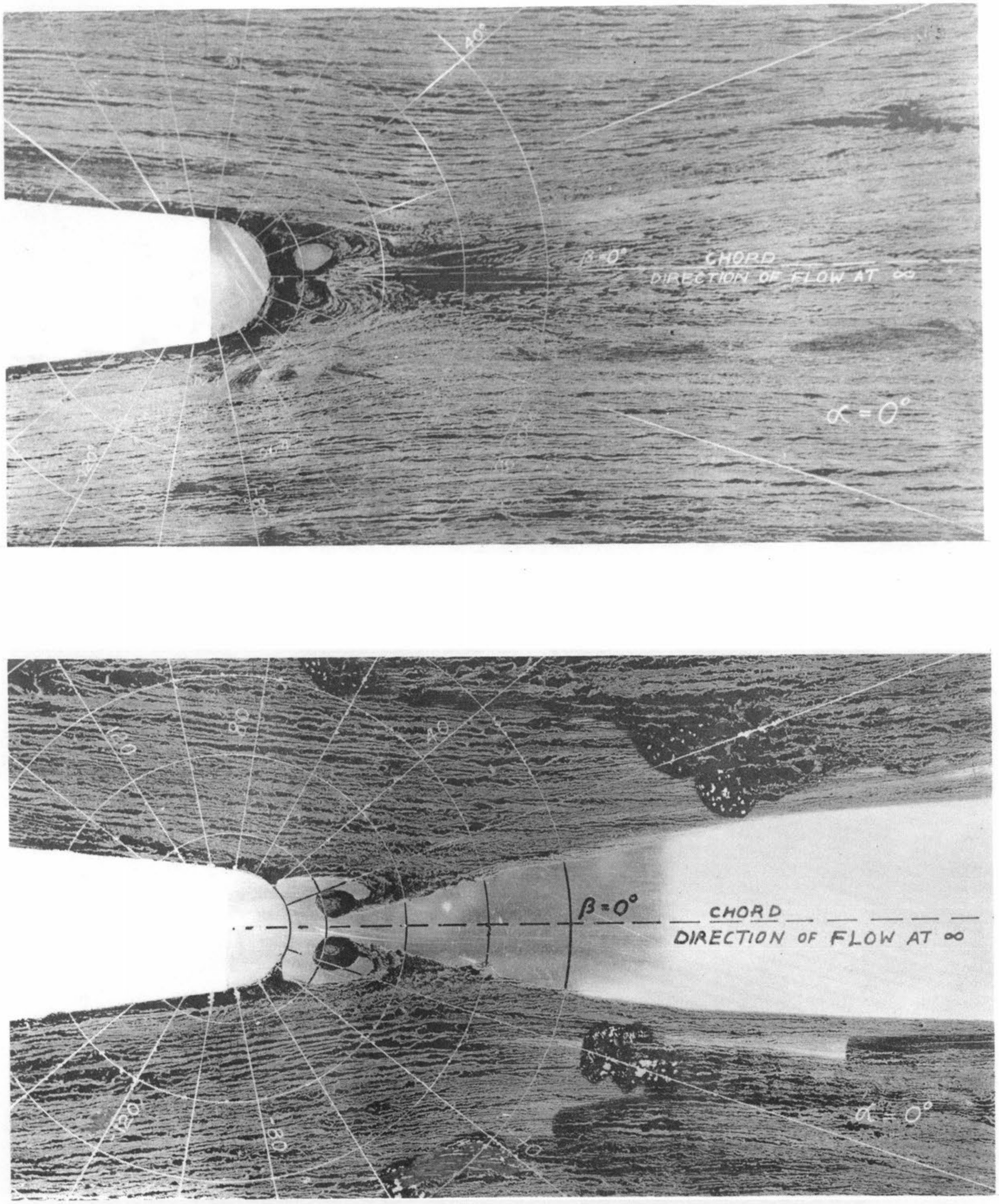

FIG. 25 — LAMP BLACK TRACES OF THE FLOW
NEAR THE TRAILING EDGE
a - 0 DEGREE ANGLE OF ATTACK

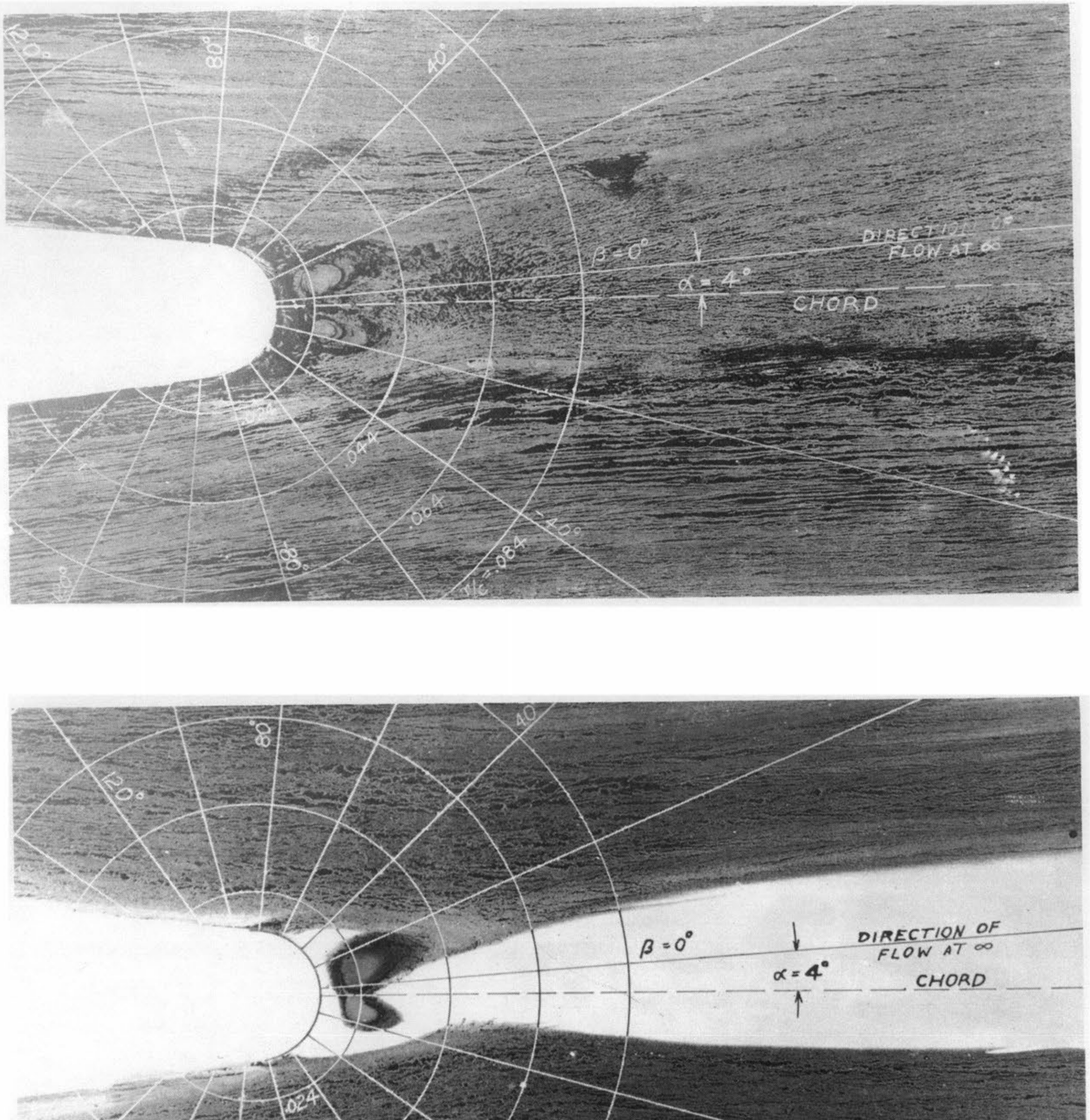

FIG.25 – CONTINUED

b – 4 DEGREES ANGLE OF ATTACK

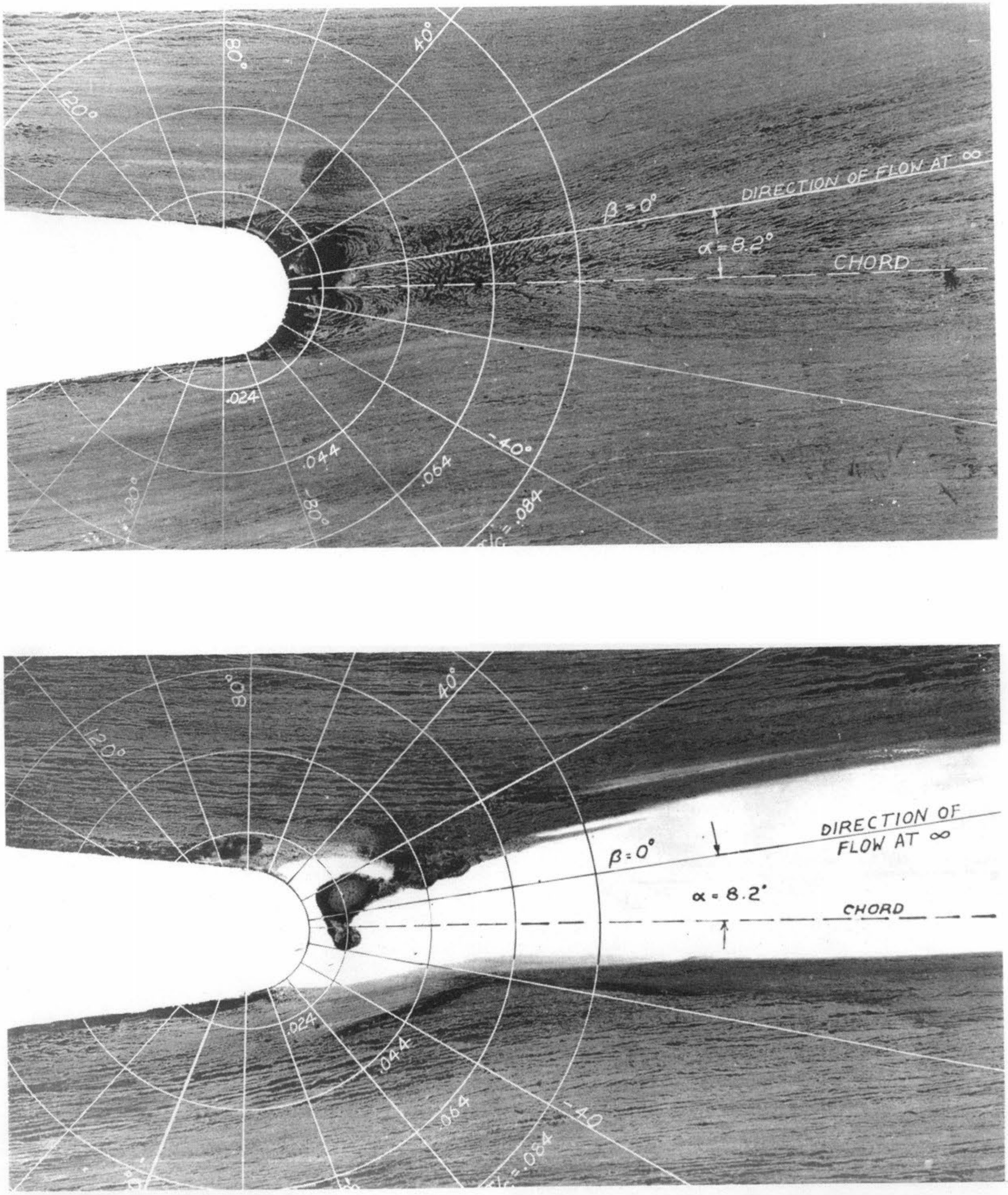

FIG. 25 - CONTINUED

c - 8.2 DEGREES ANGLE OF ATTACK

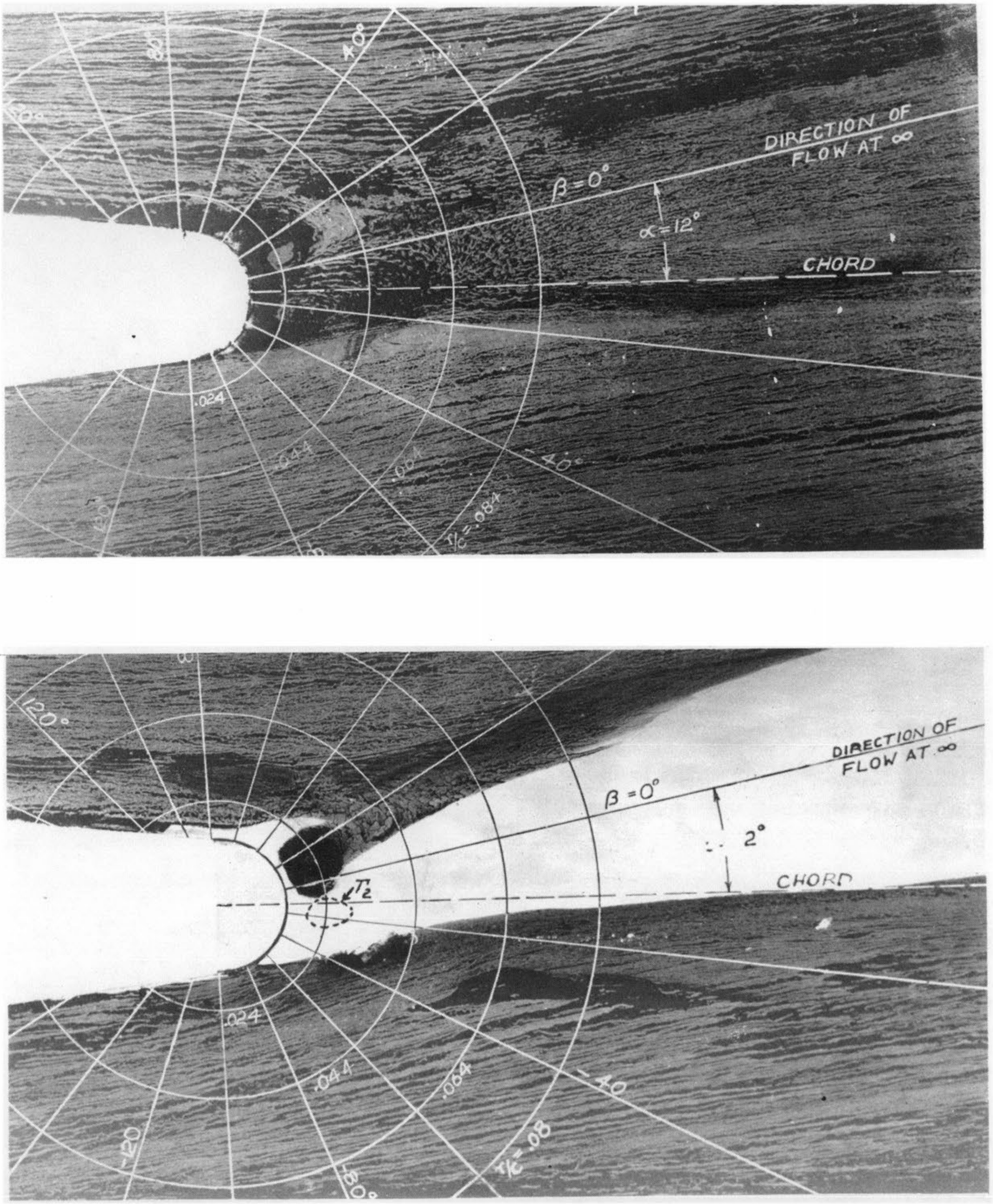

FIG. 25 – CONTINUED

d – 12 DEGREES ANGLE OF ATTACK

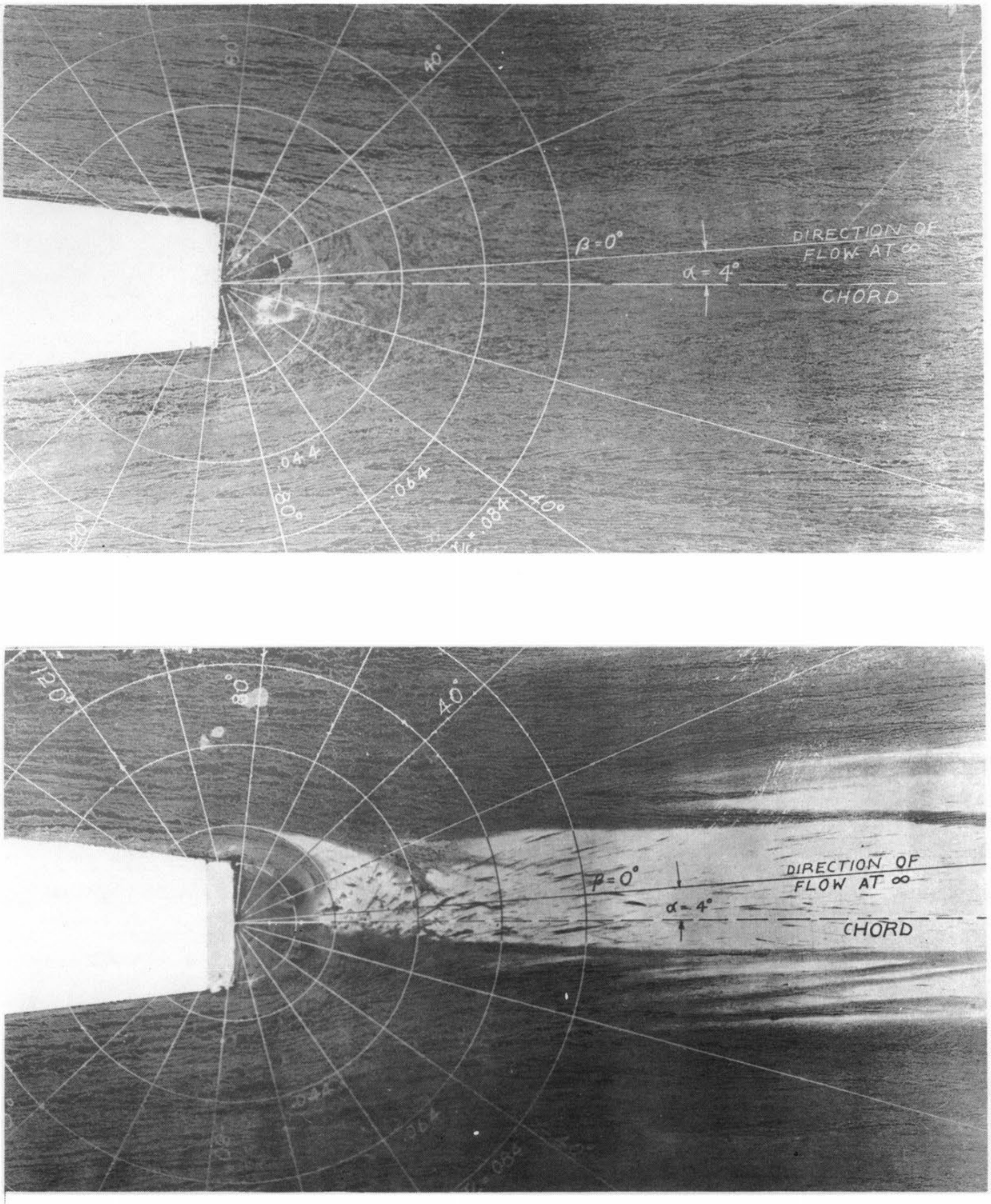

FIG. 25 – CONTINUED

e – 4 DEGREES ANGLE OF ATTACK WITH SQUARE TRAILING EDGE

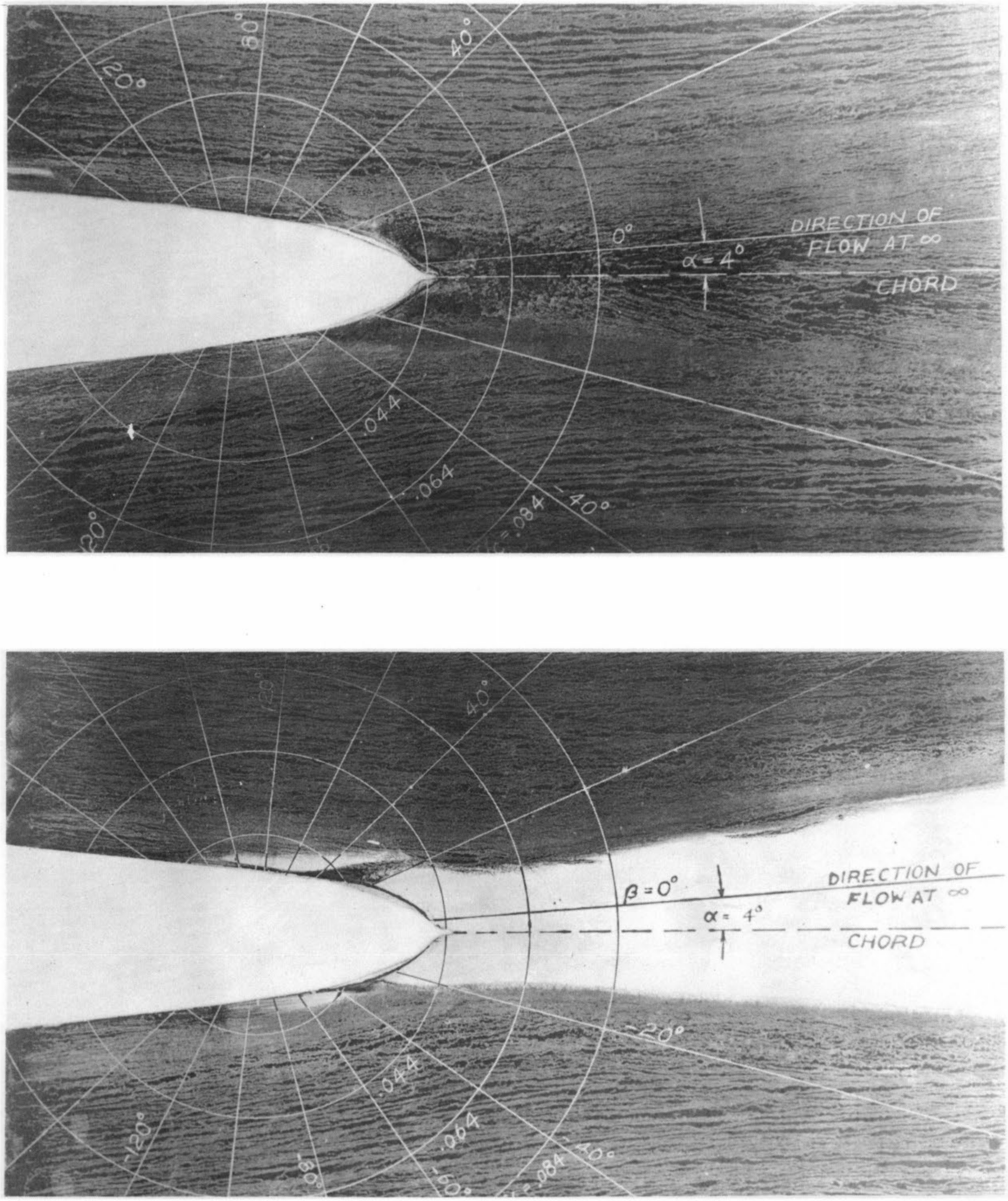

FIG. 25 – CONTINUED

f – 4 DEGREES ANGLE OF ATTACK WITH CUSPED TRAILING EDGE

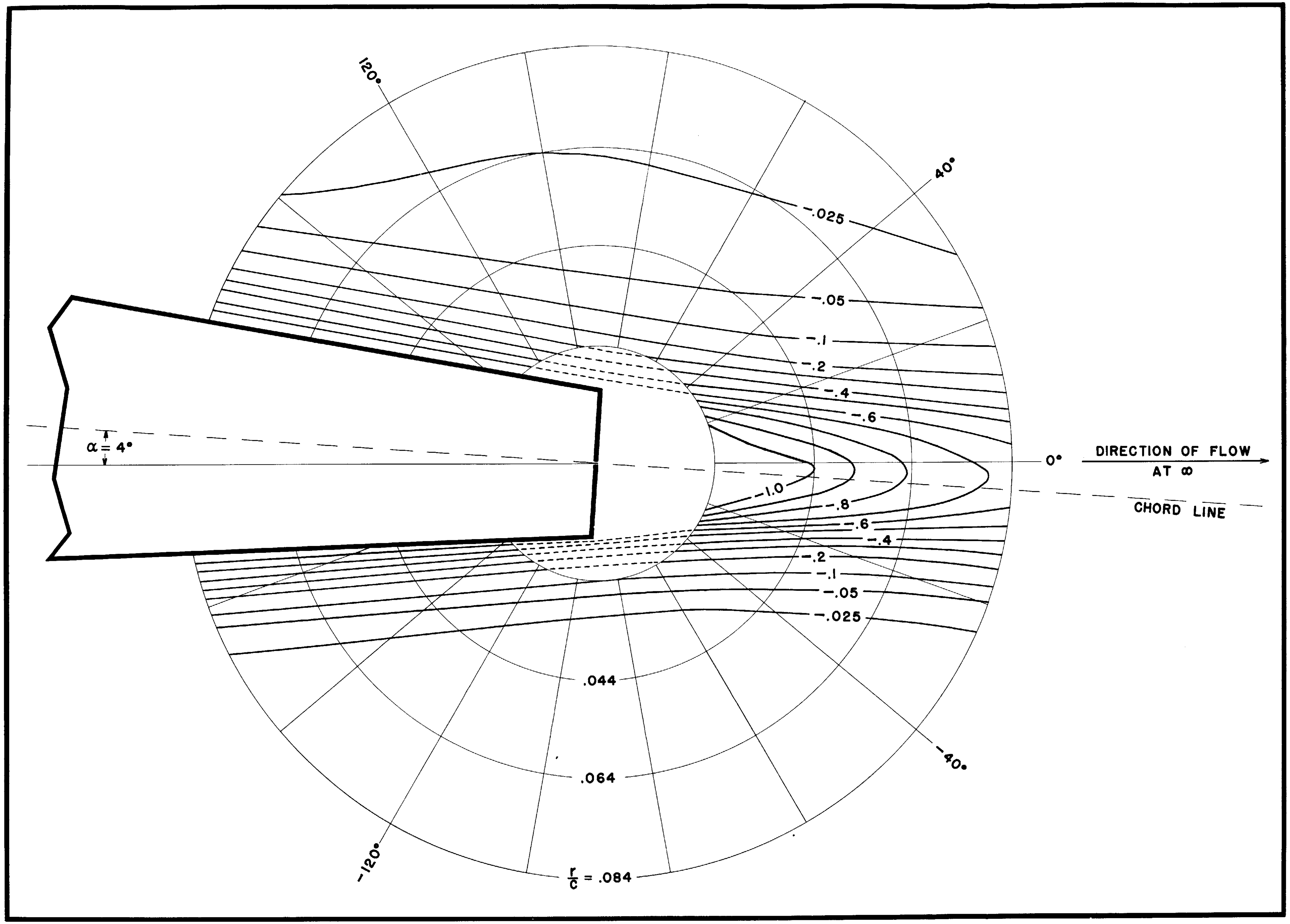

FIG. 26 – CONTOUR PLOT OF THE FLOW AROUND THE TRAILING EDGE OF THE AIRFOIL AT 4 DEGREES ANGLE OF ATTACK WITH SQUARE TRAILING EDGE. α – LINES OF CONSTANT STAGNATION PRESSURE.

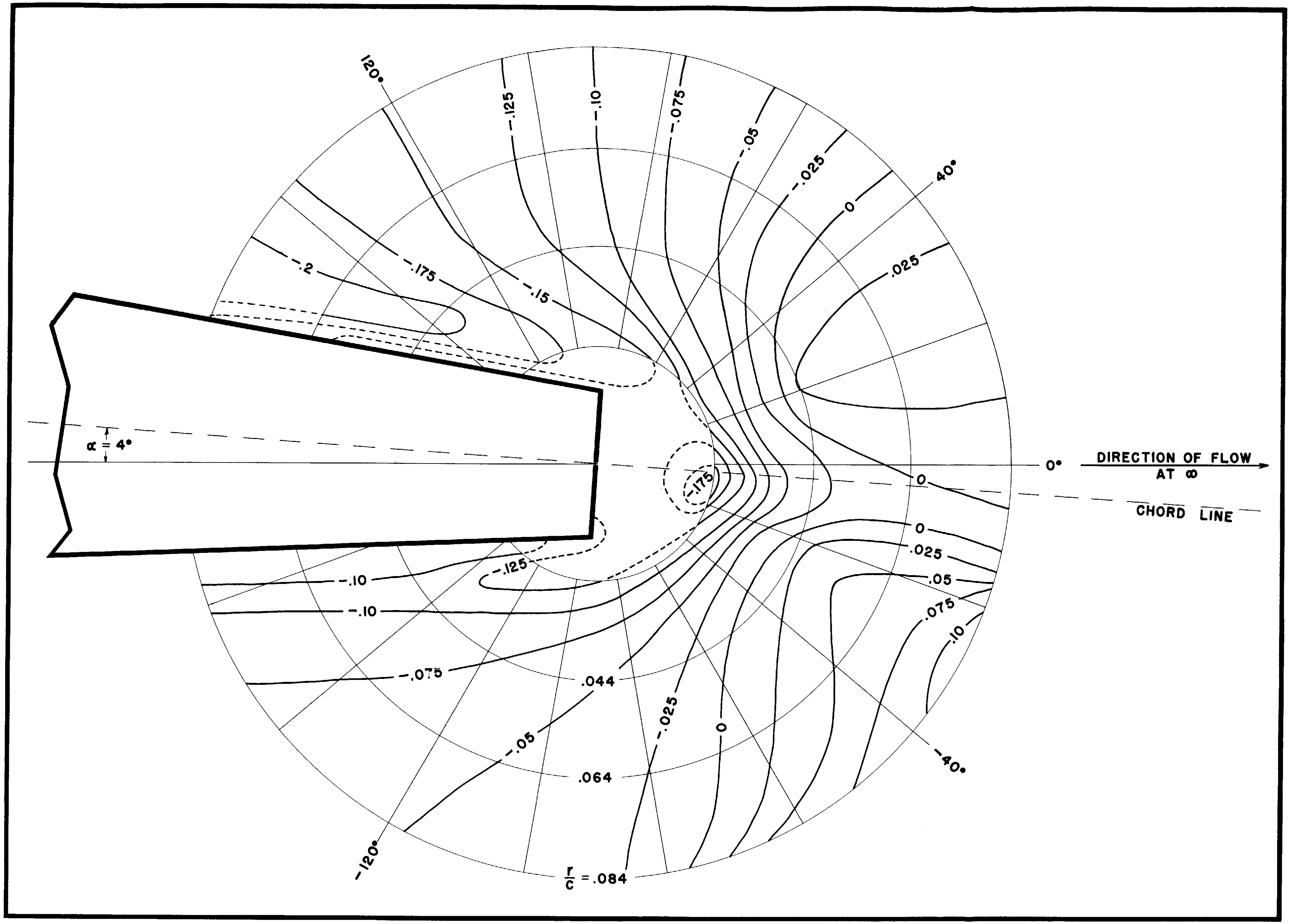

FIG. 26 – CONTINUED. b – LINES OF CONSTANT STATIC PRESSURE.

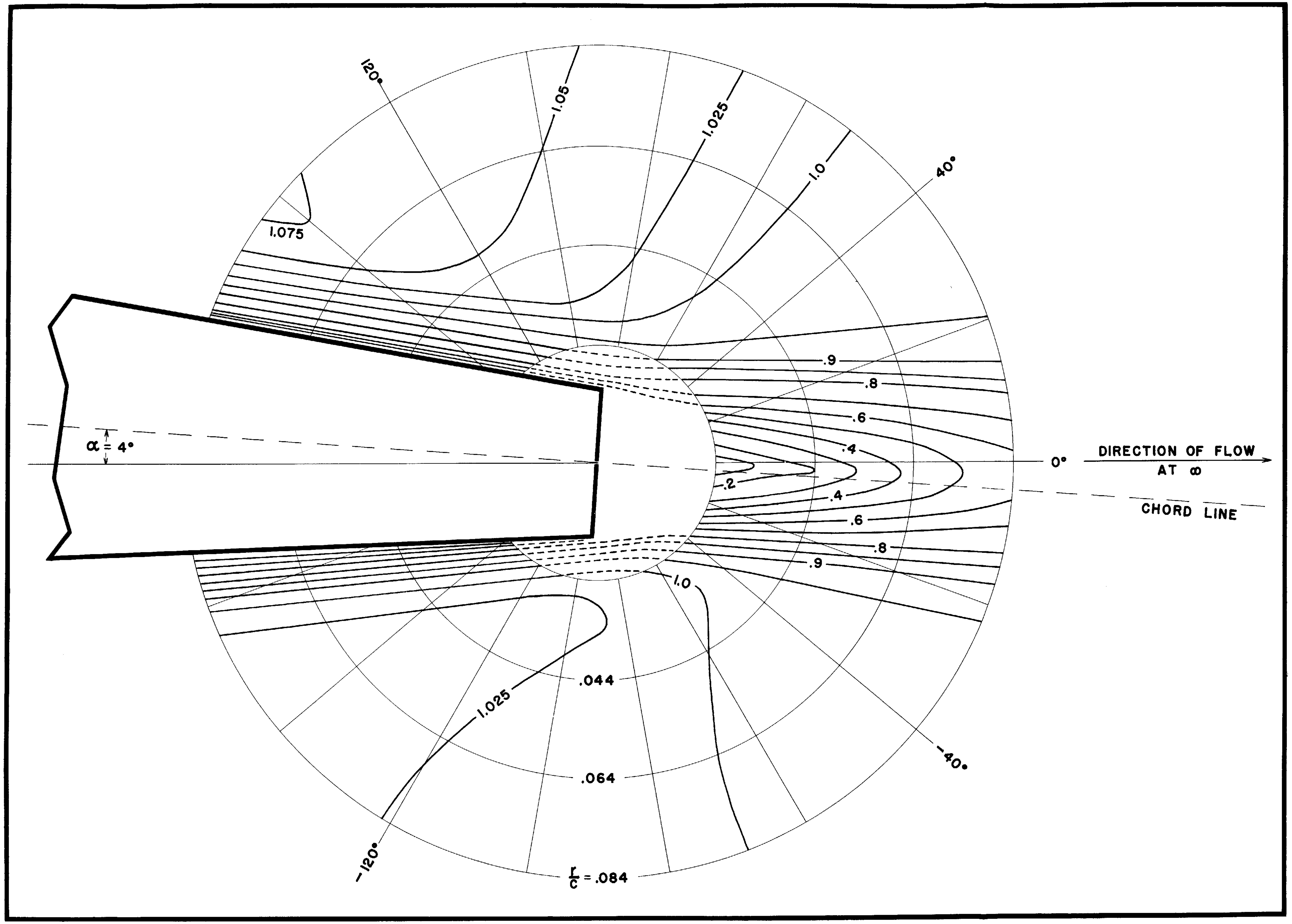

FIG. 26 – CONTINUED. c – LINES OF CONSTANT VELOCITY.

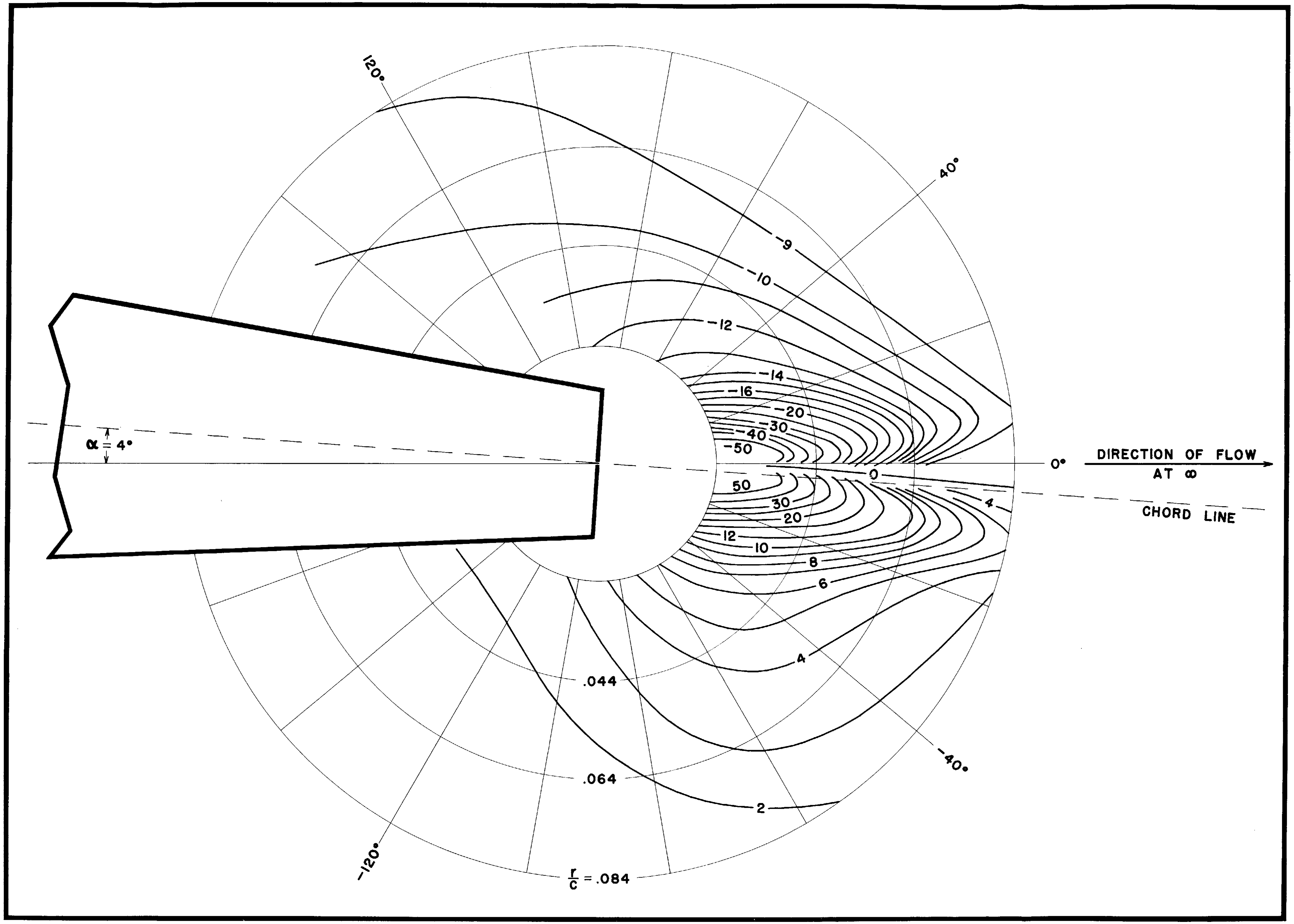

FIG. 26 – CONTINUED. d – LINES OF CONSTANT FLOW ANGLE – DEGREES.

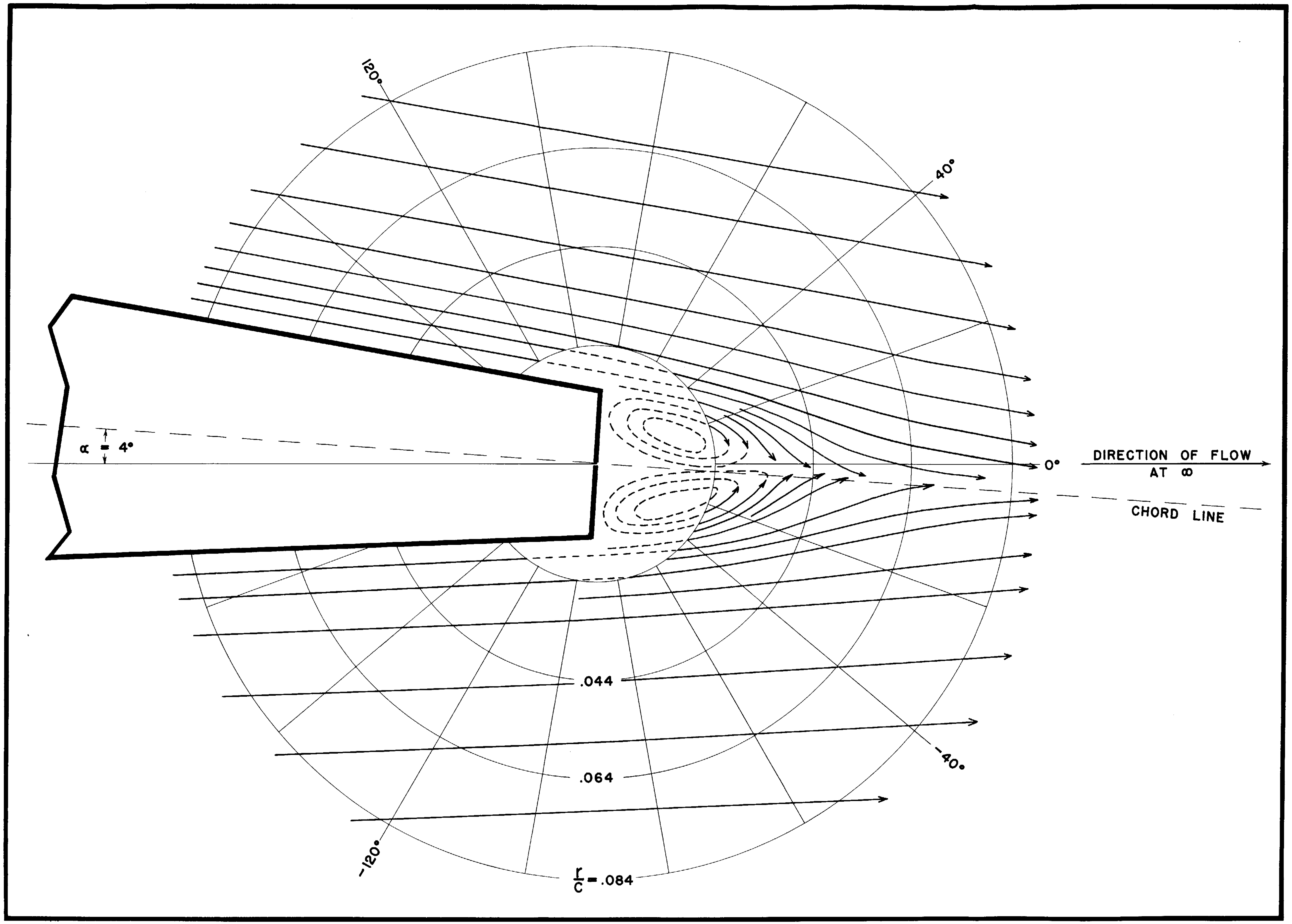

FIG. 26 – CONTINUED. e – STREAMLINES.

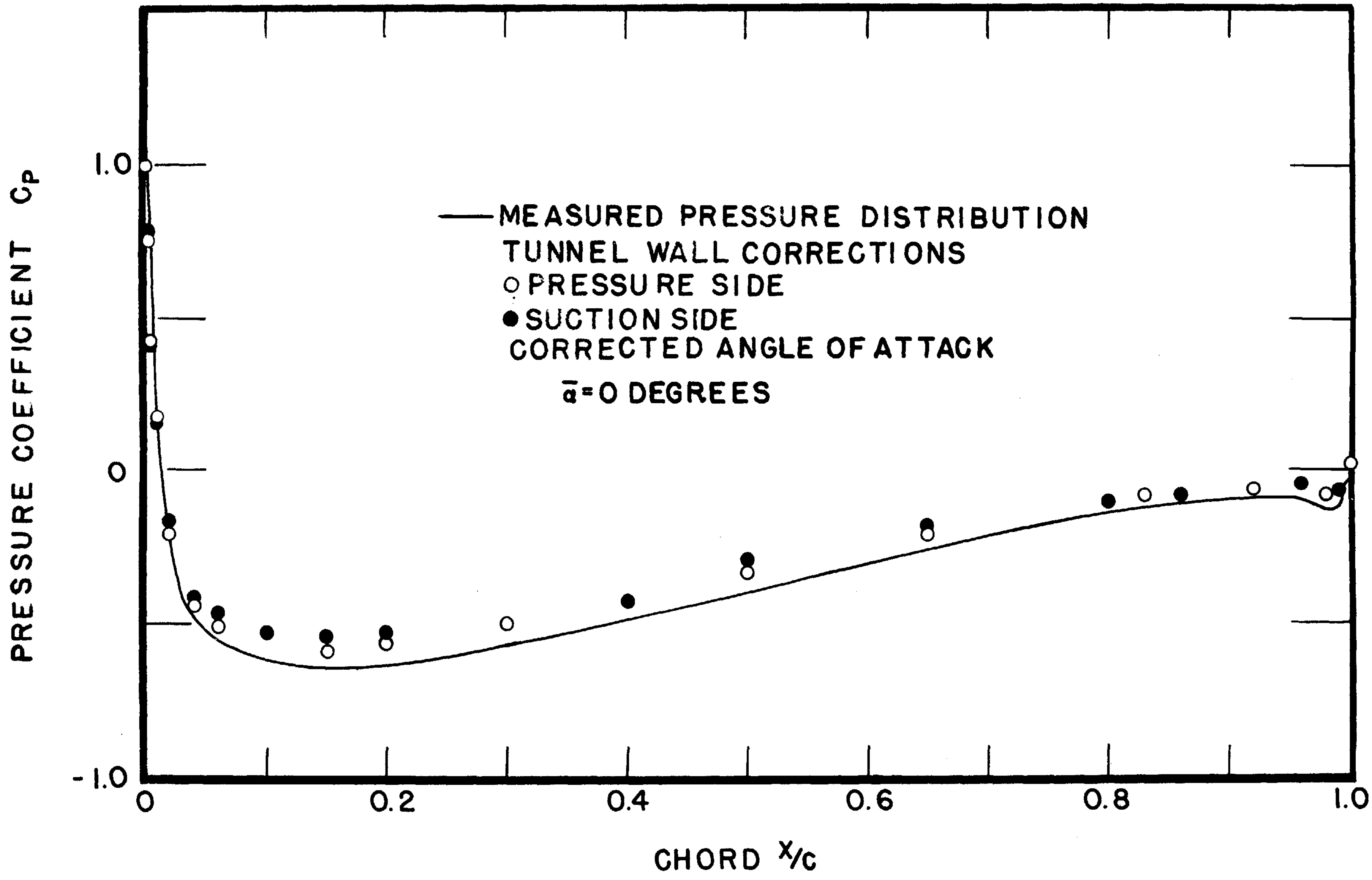

FIG. 27— PRESSURE DISTRIBUTION AROUND THE AIRFOIL WITH TUNNEL WALL CORRECTIONS

a—0 DEGREE ANGLE OF ATTACK

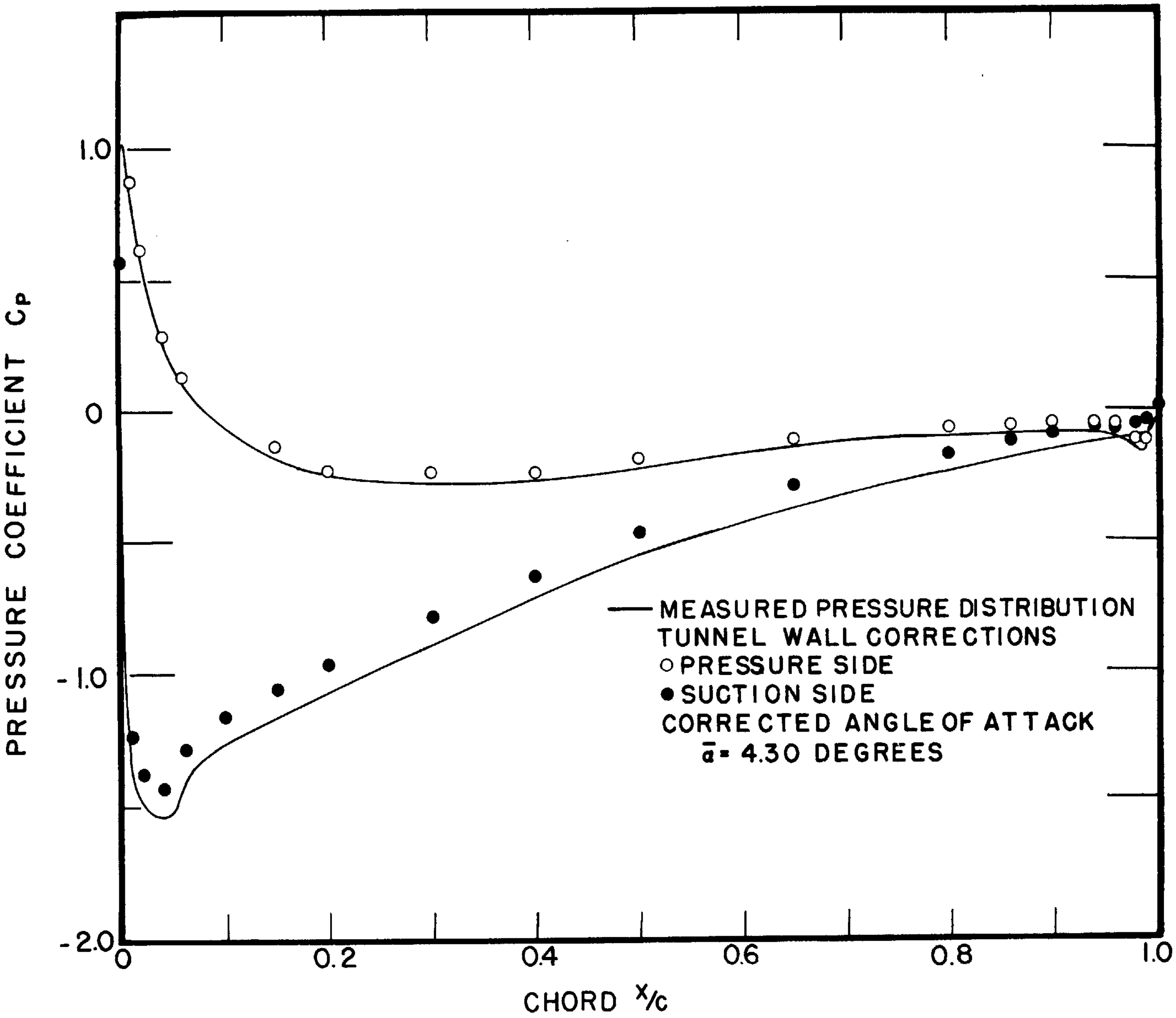

FIG. 27– CONTINUED
b– 4 DEGREE ANGLE OF ATTACK

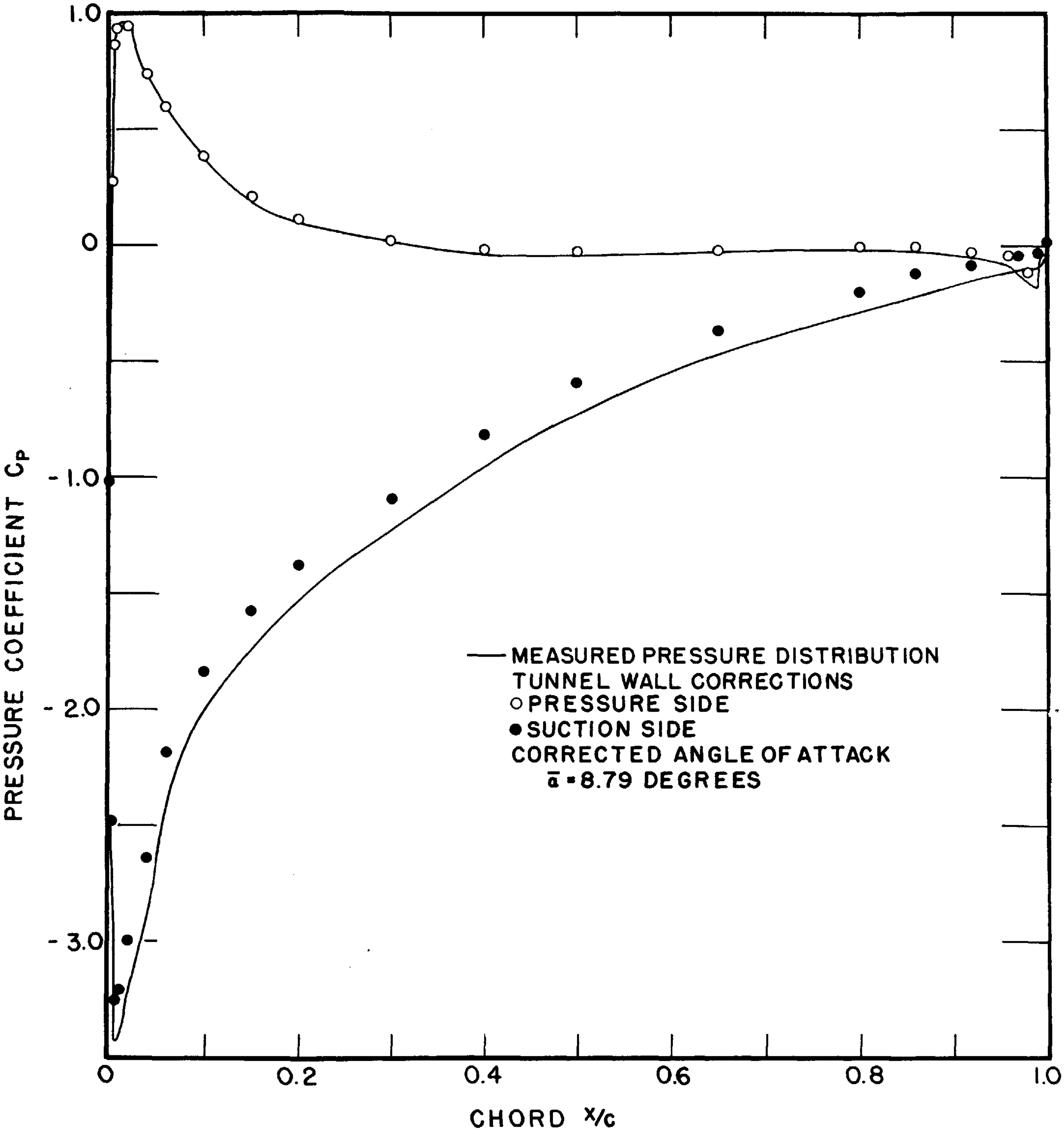

FIG. 27—CONTINUED
c – 8.2° ANGLE OF ATTACK

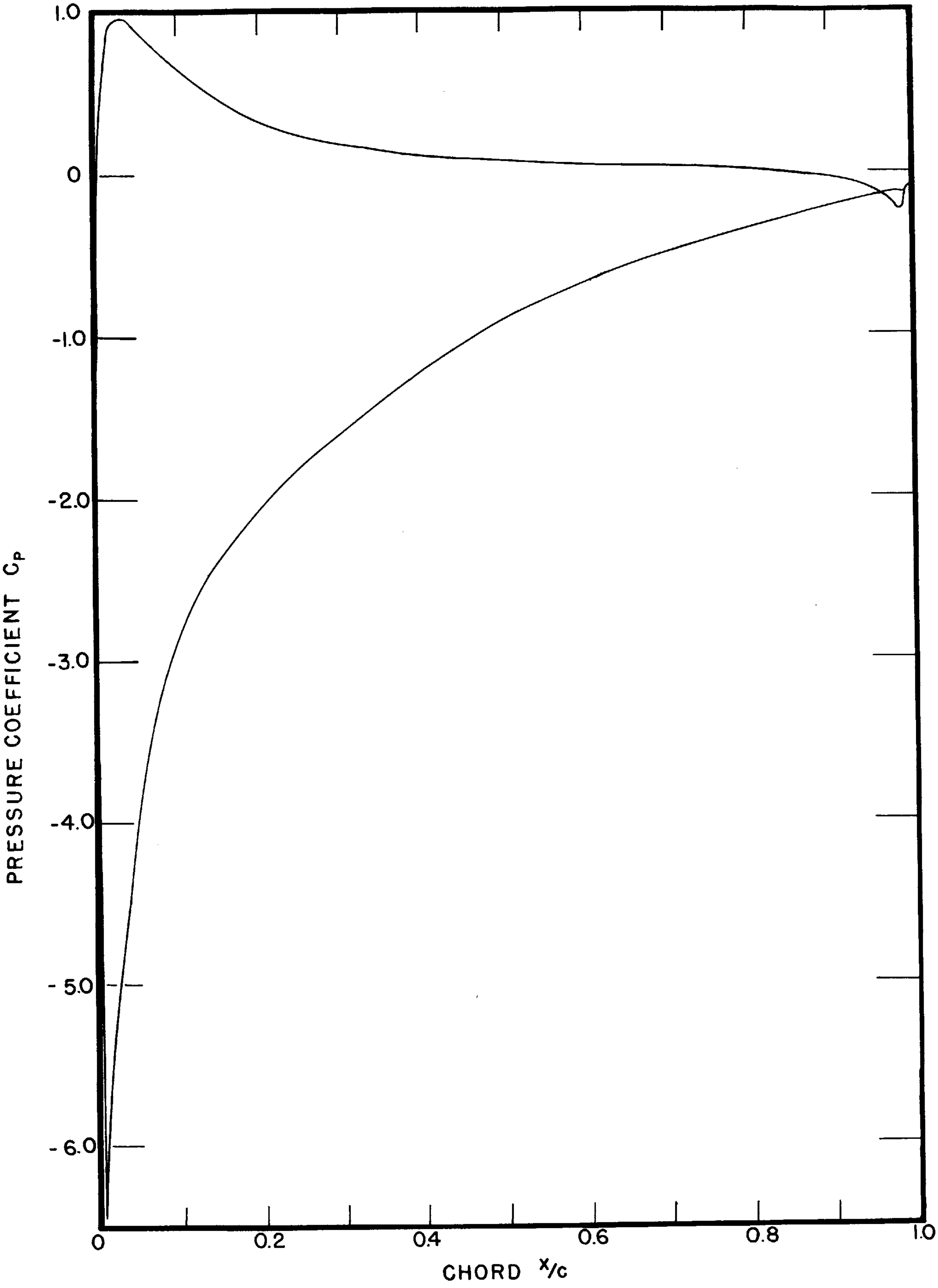

FIG. 27- CONTINUED
d-12 DEGREE ANGLE OF ATTACK

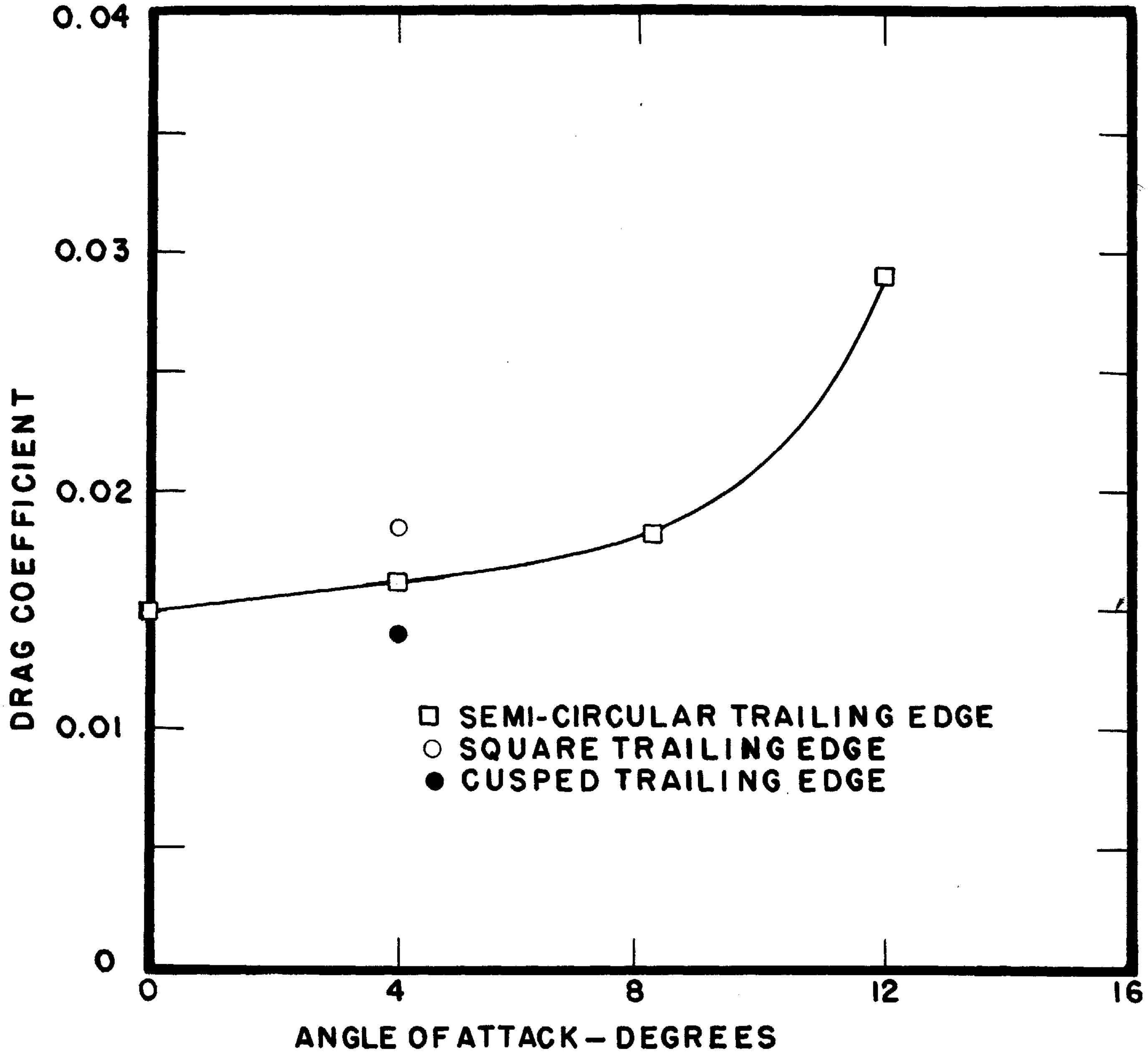

FIG. 28 – DRAG COEFFICIENT VERSUS ANGLE OF ATTACK

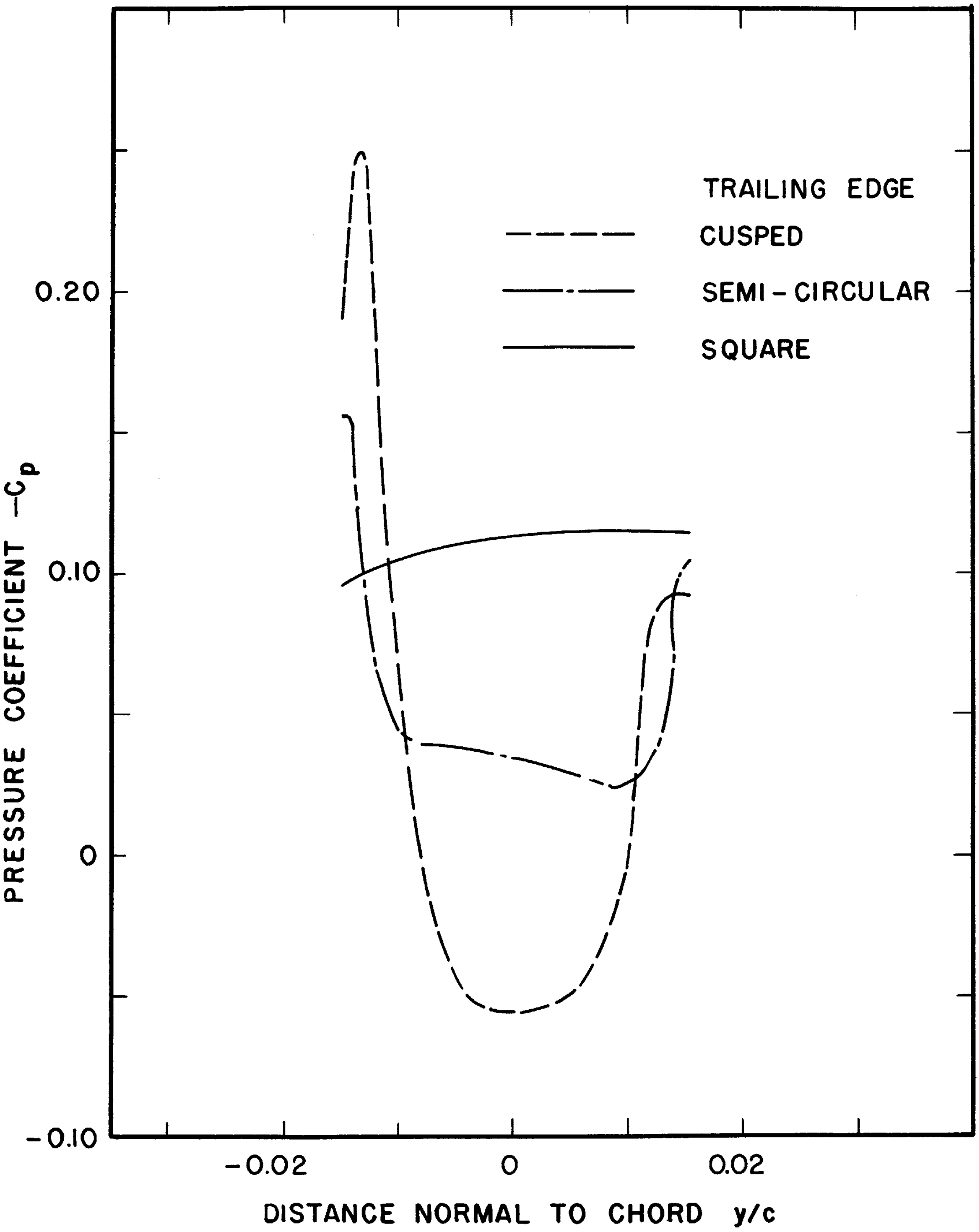

FIG. 29 - PRESSURE DISTRIBUTION AROUND TRAILING EDGE AT 4 DEGREES ANGLE OF ATTACK

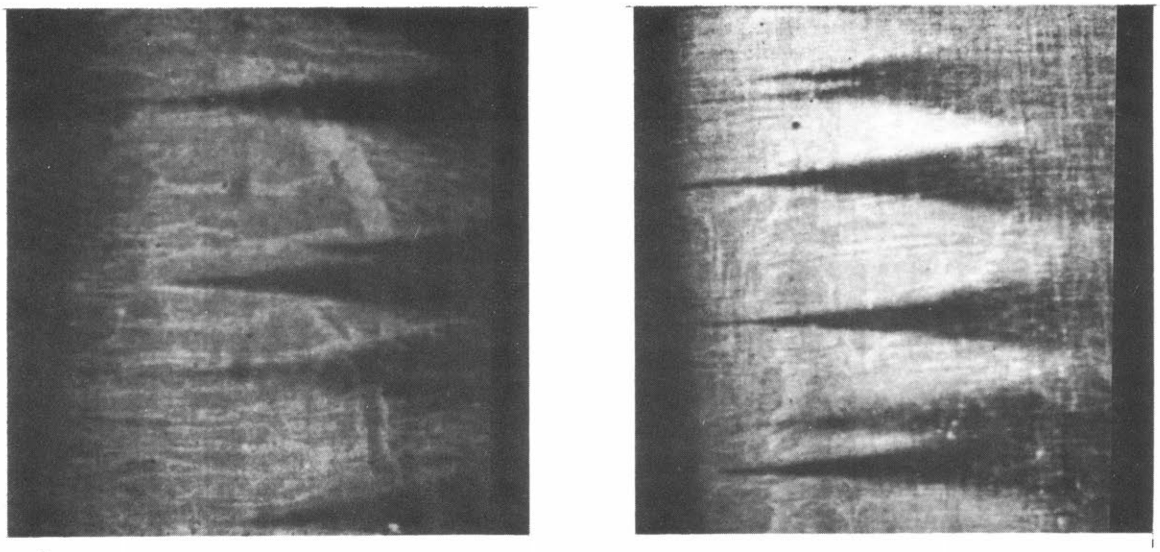

LEADING EDGE

α = 4 DEGREES

PRESSURE SIDE

LEADING EDGE

α = 0 DEGREE

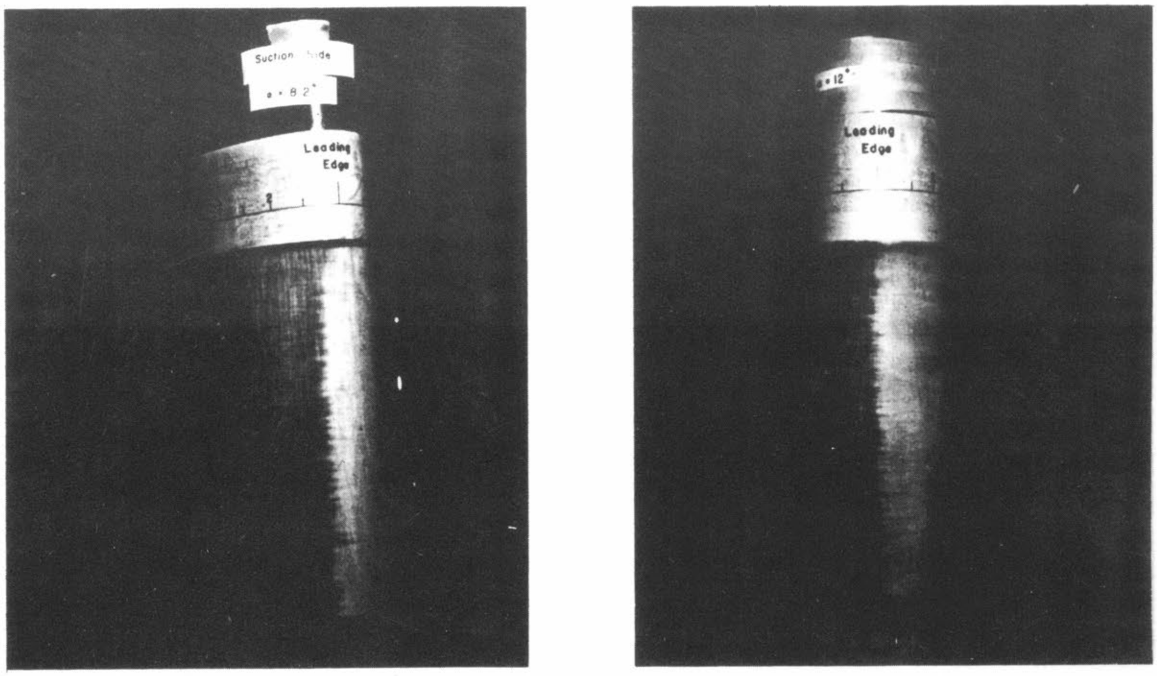

α = 8.2 DEGREES

SUCTION SIDE

α = 12 DEGREES

SUCTION SIDE

FIG. 30 - VISUALIZATION OF TRANSITION.

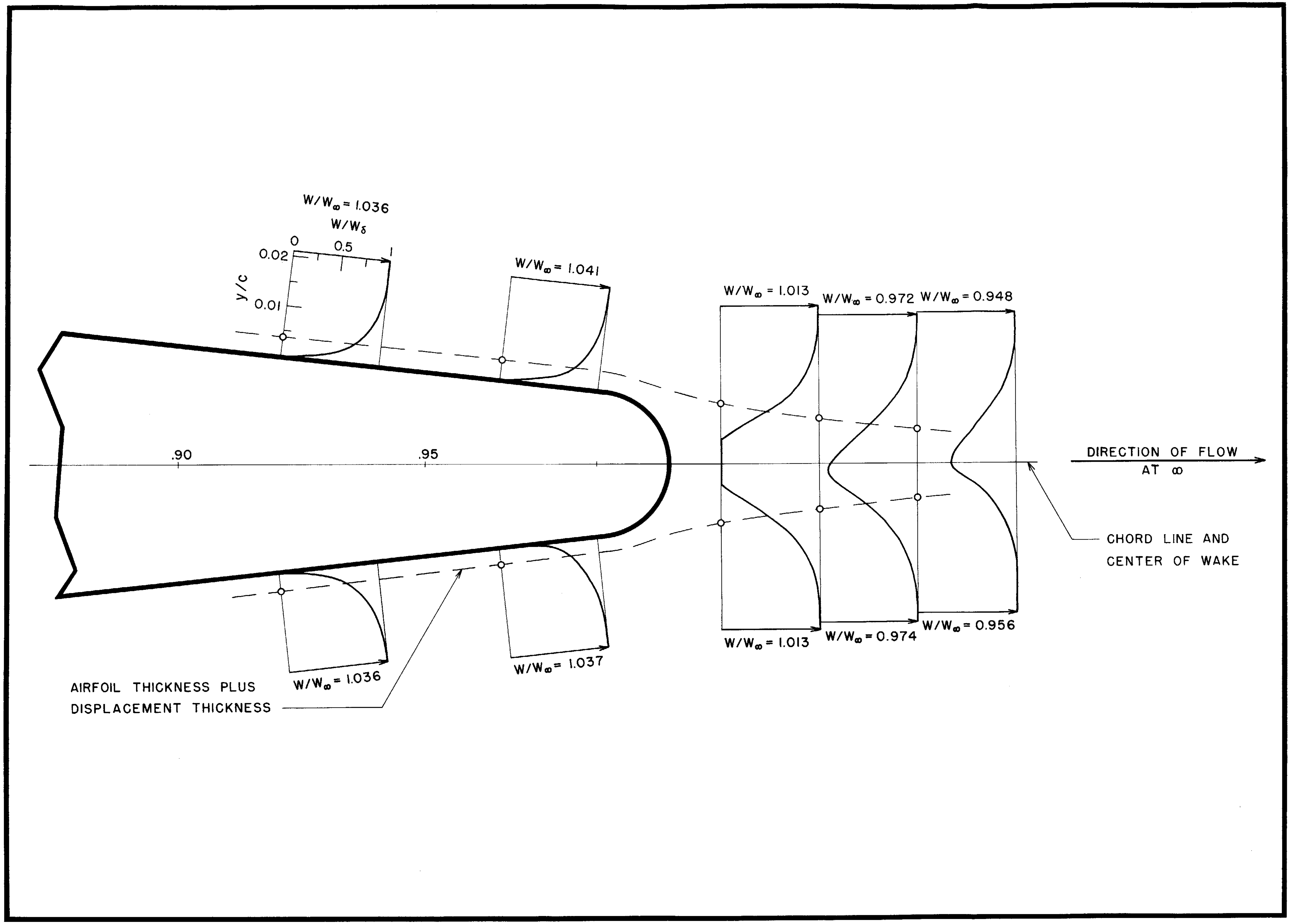

FIG. 31 – VARIATION OF DISPLACEMENT THICKNESS AND VELOCITY PROFILES NEAR THE TRAILING EDGE.

a – 0 DEGREE ANGLE OF ATTACK.

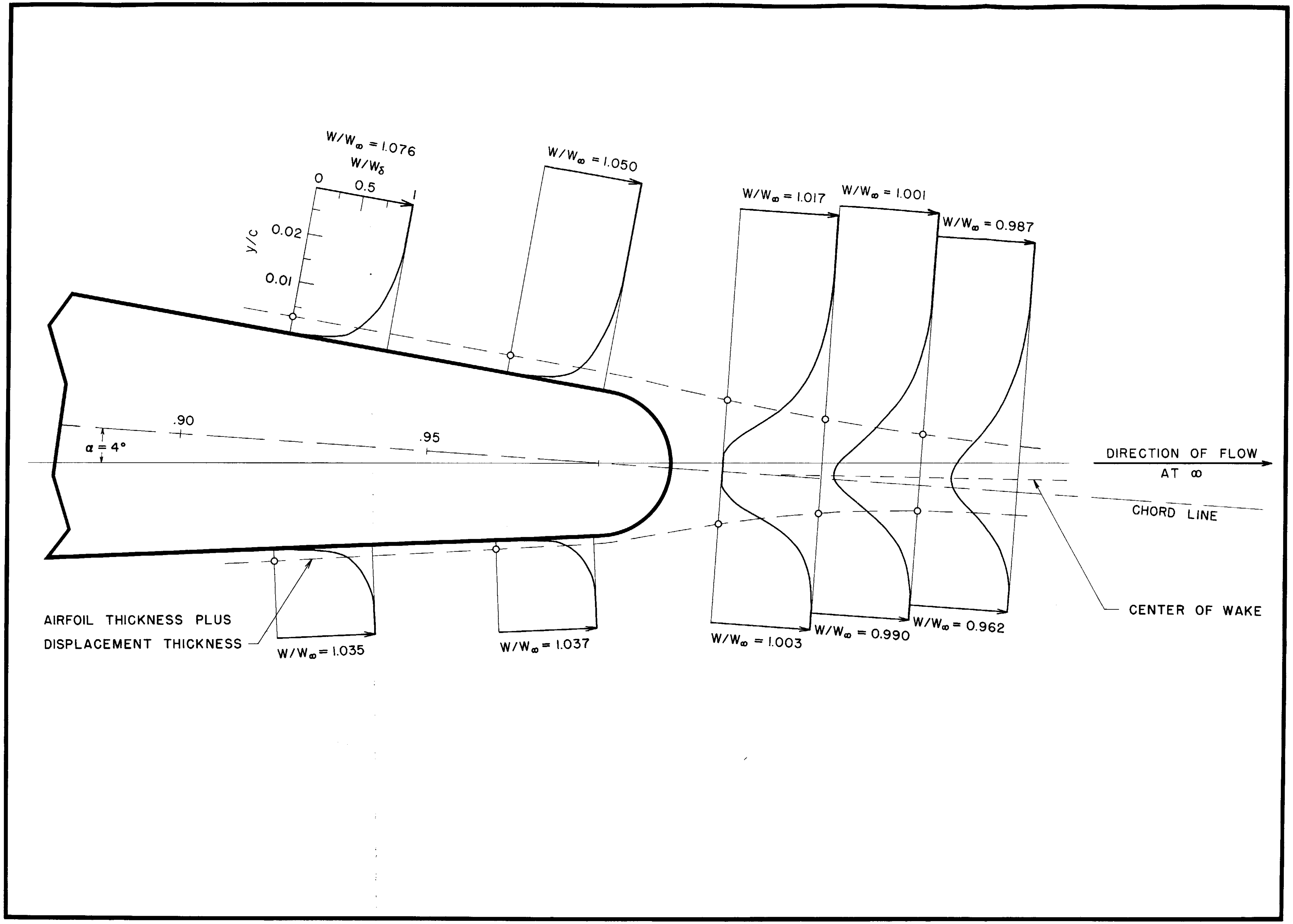

FIG. 31 - CONTINUED. b - 4 DEGREE ANGLE OF ATTACK.

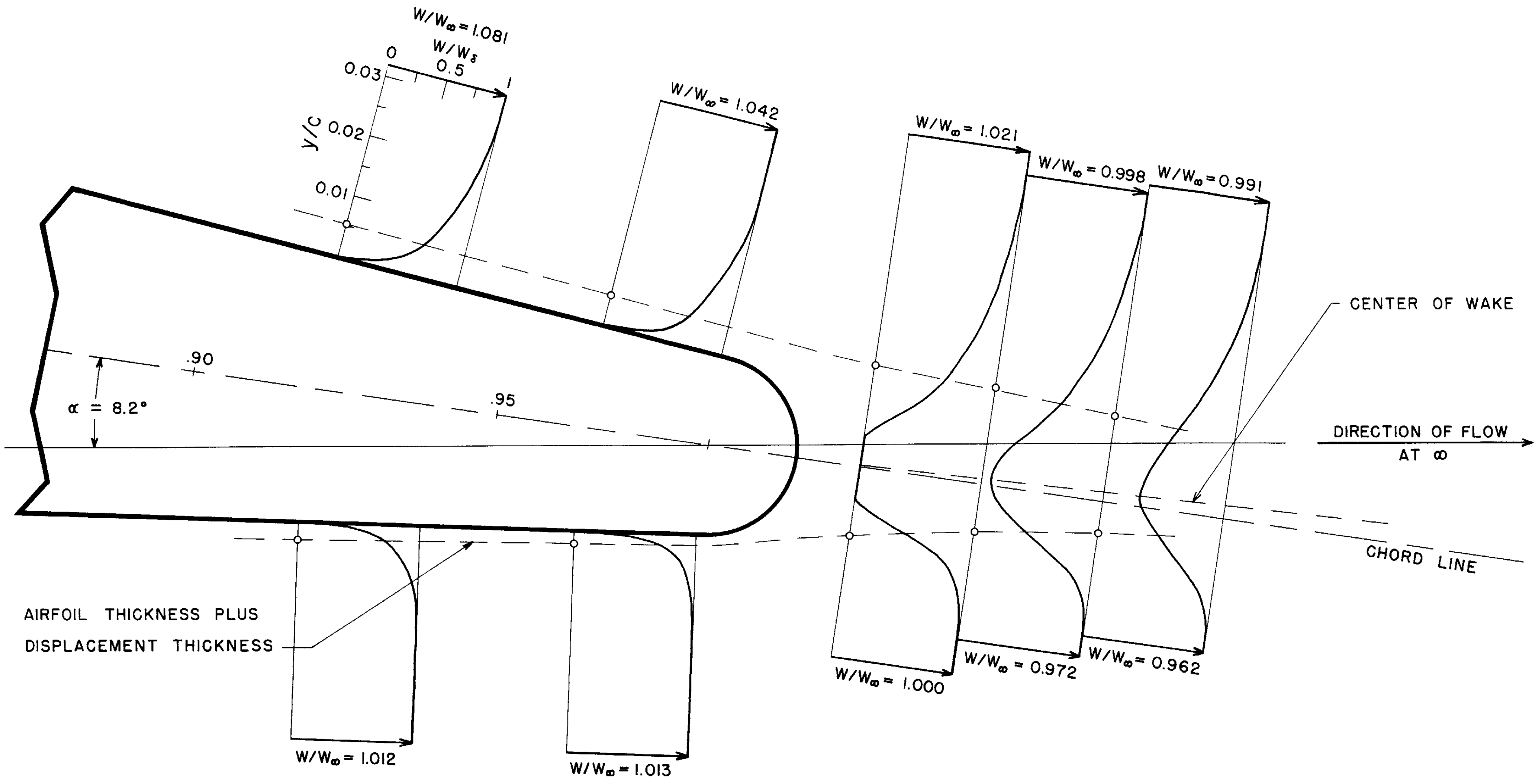

FIG. 31 - CONTINUED. c - 8.2 DEGREE ANGLE OF ATTACK.

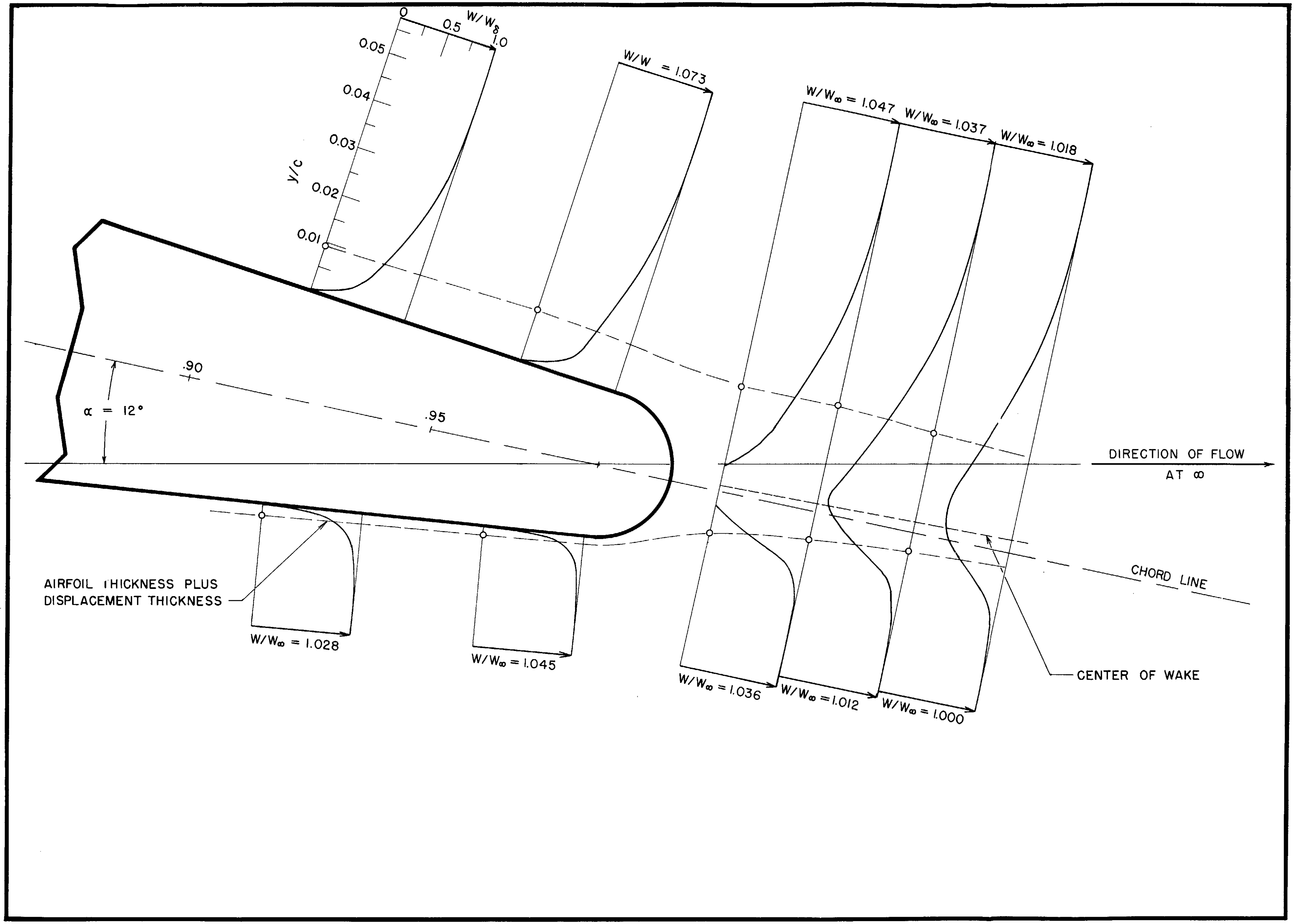

FIG. 31 - CONTINUED. d - 12 DEGREE ANGLE OF ATTACK.

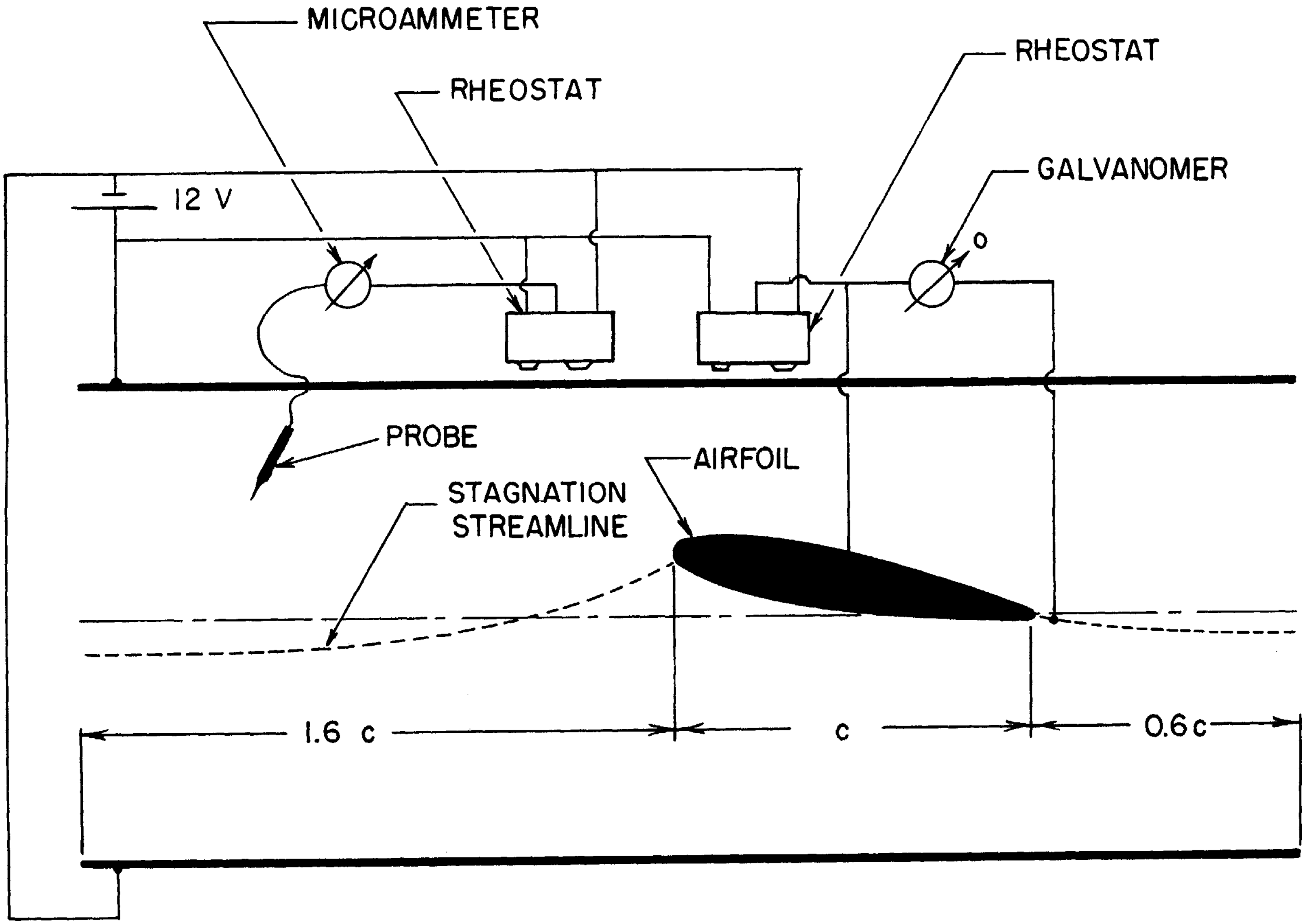

FIG. 32 - SCHEMATIC OF THE ELECTRIC ANALOG

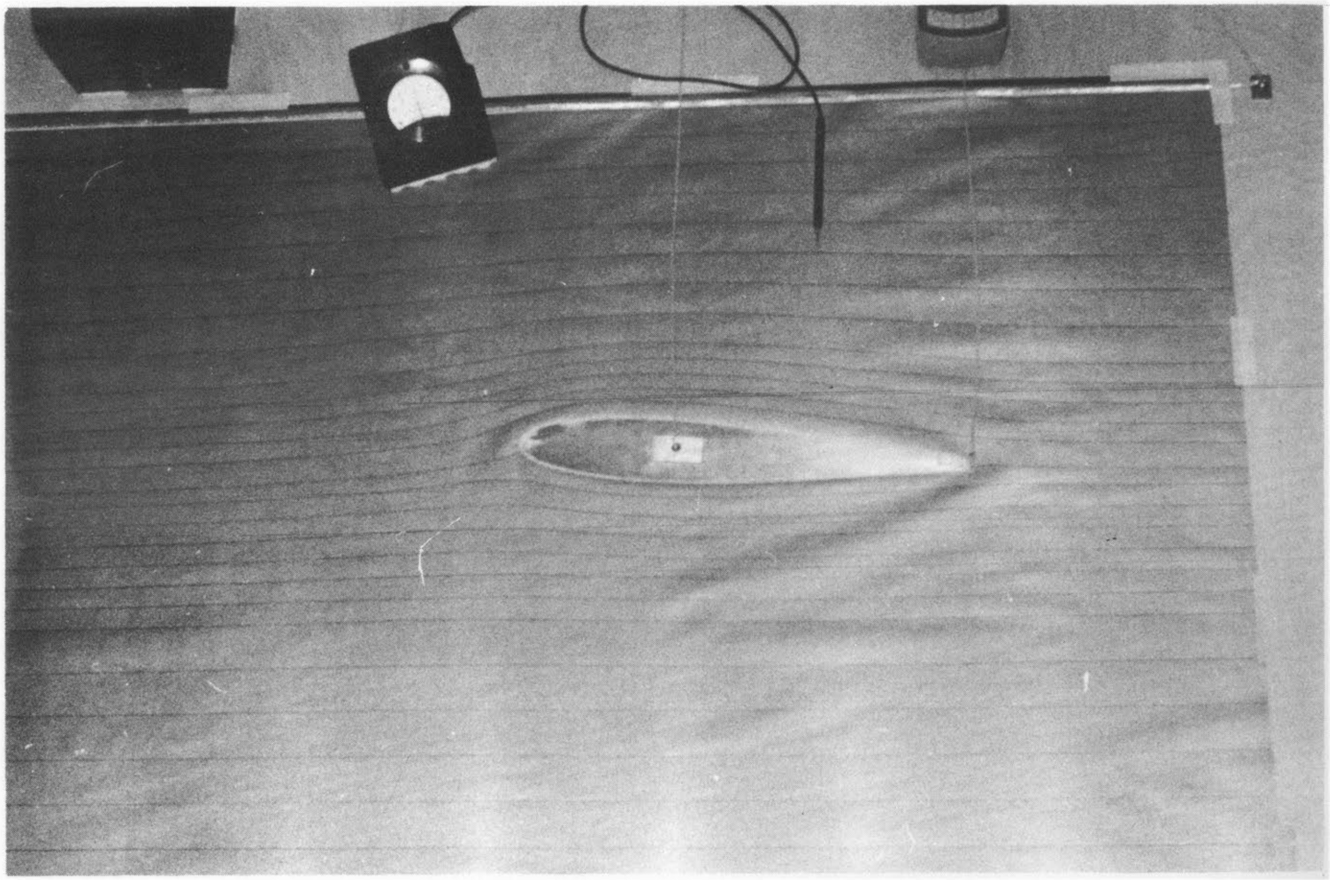

FIG. 33 - PHOTOGRAPH OF ELECTRICAL ANALOG.

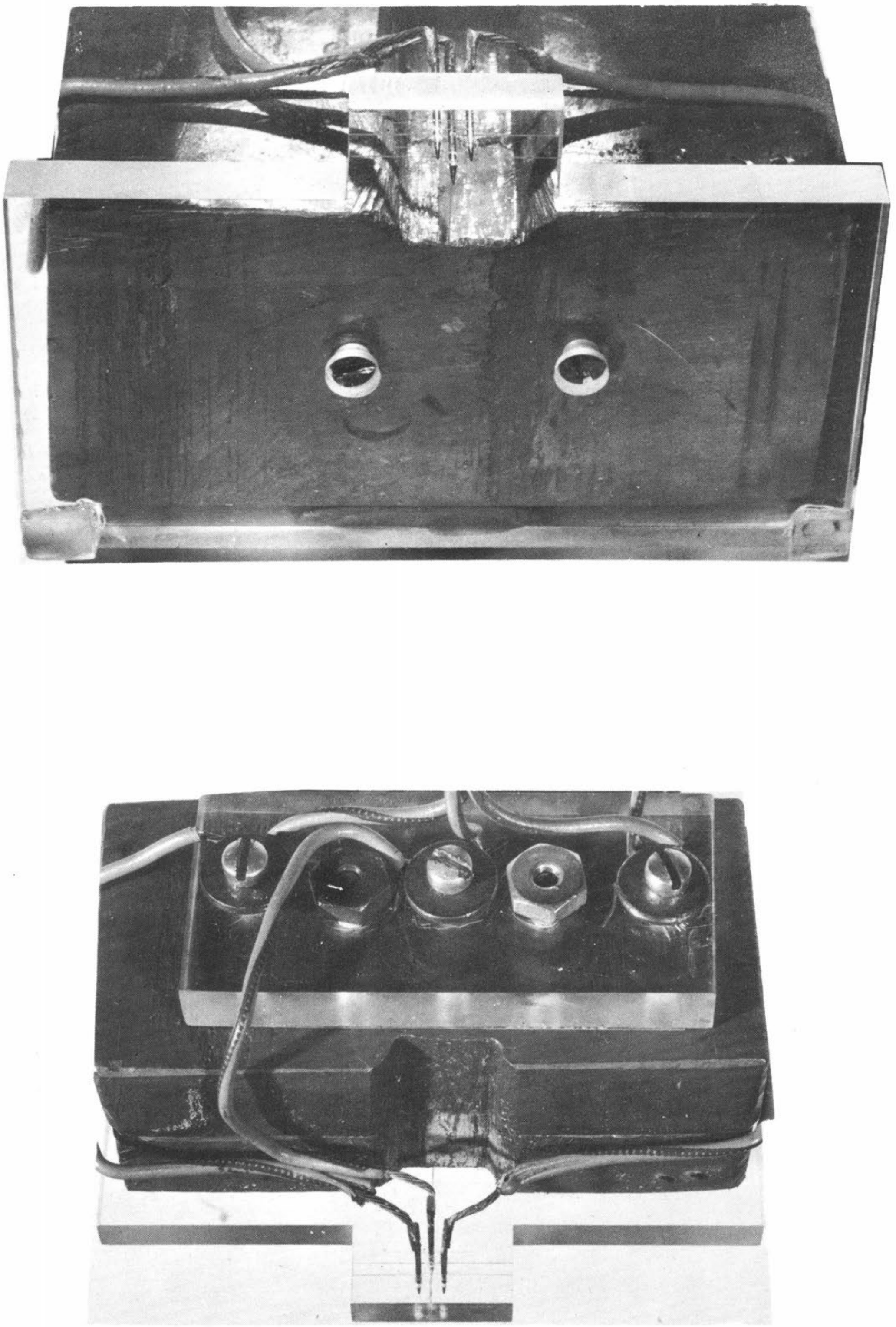

FIG. 34 - GRADIENT MEASURING PROBE.

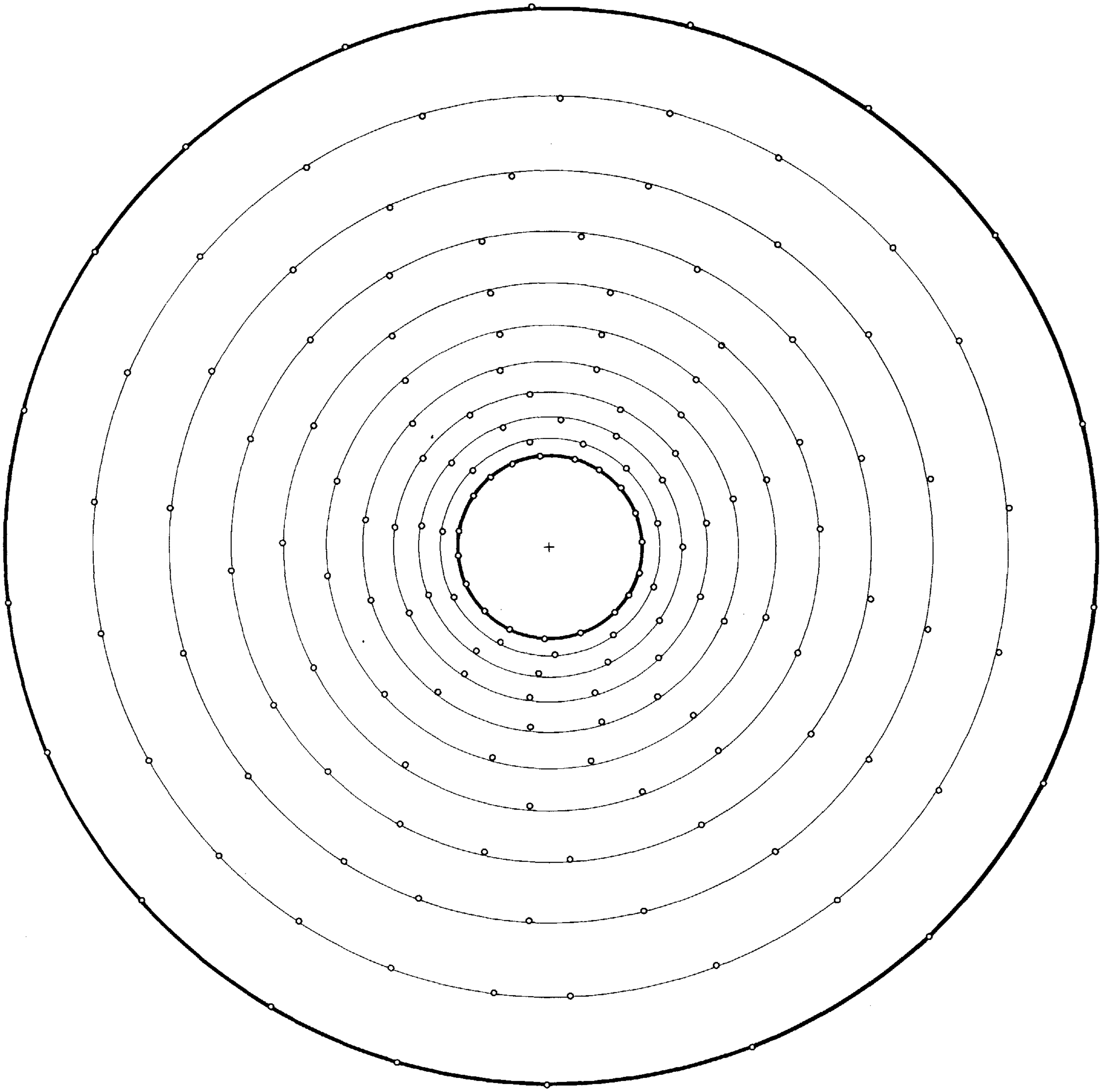

FIG. 35

ELECTRICAL ANALOG OF POTENTIAL VORTEX

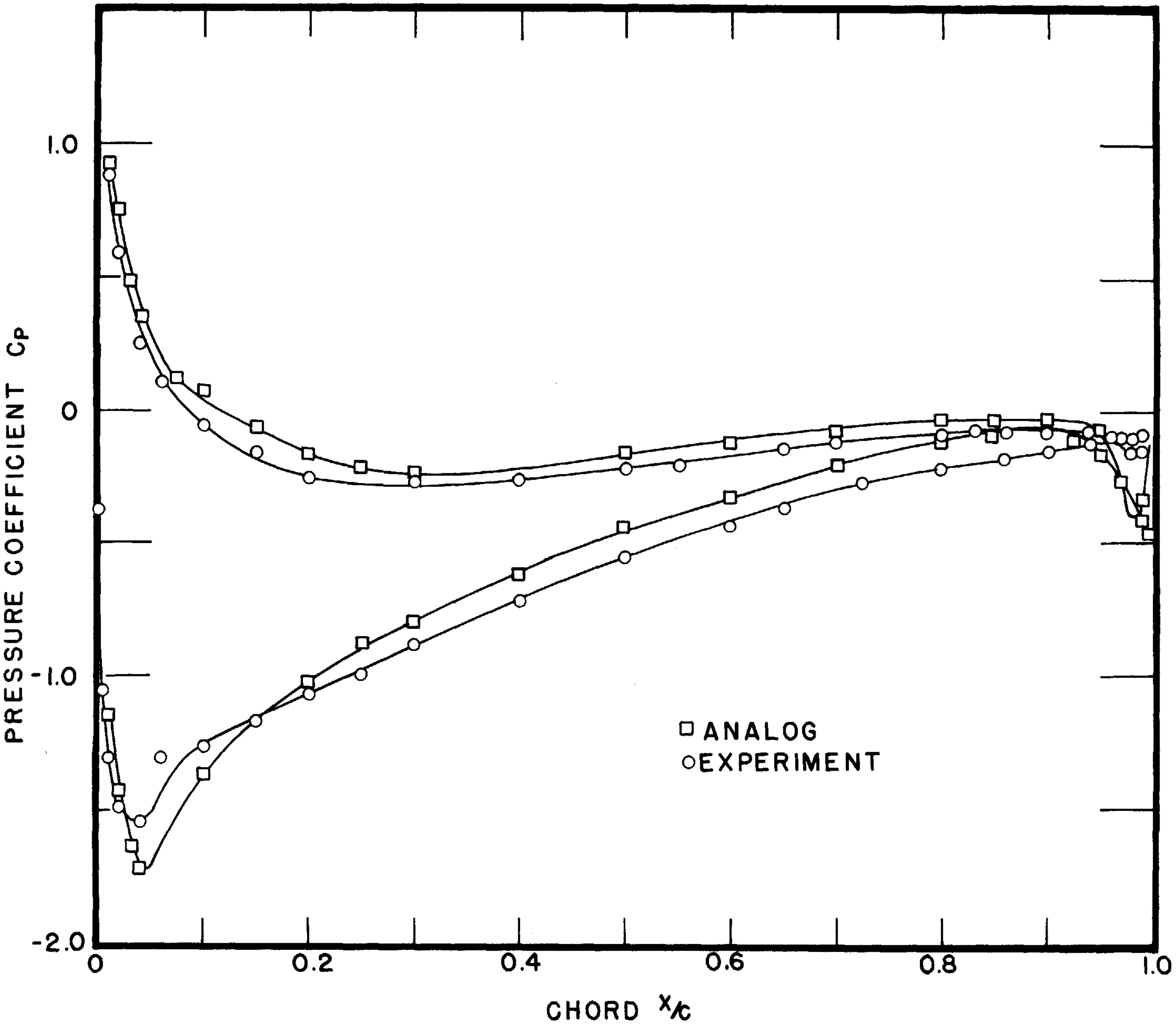

FIG.36 PRESSURE DISTRIBUTION DETERMINED BY THE ELECTRICAL ANALOG—POTENTIAL FLOW

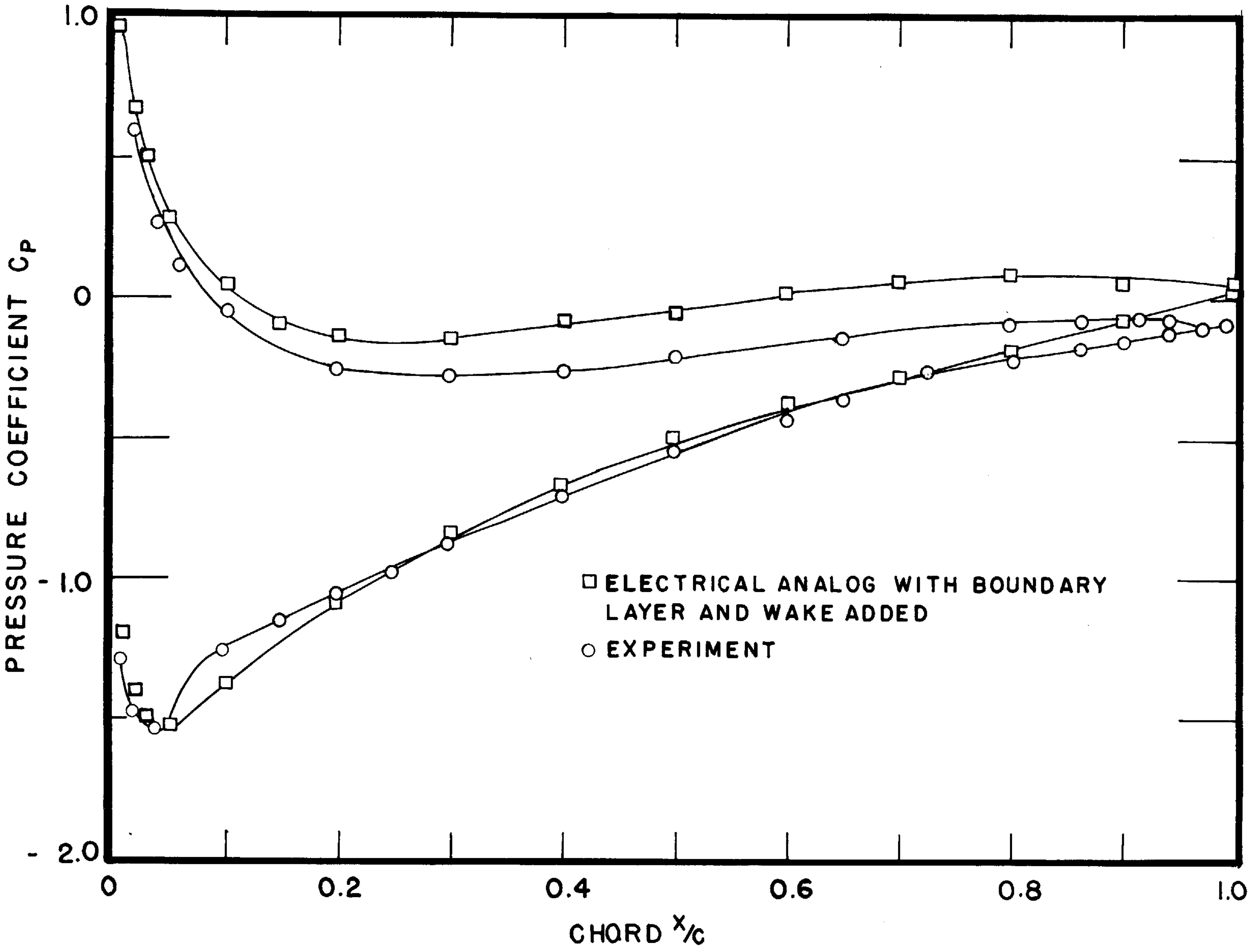

FIG. 37— PRESSURE DISTRIBUTION DETERMINED BY THE ELECTRICAL ANALOG WITH DISPLACEMENT THICKNESS OF THE BOUNDARY LAYER AND WAKE ADDED